Kelemen, P.B., Kikawa, E., Miller, D.J., et al., 2004
Proceedings of the Ocean Drilling Program, Initial Reports Volume 209

9. Site 1274[1]

Shipboard Scientific Party[2]

OPERATIONS SUMMARY

Hole 1274A

After transit from Site 1273 in dynamic positioning mode with the drill string suspended below the ship, we arrived on the Global Positioning System coordinates for the start of the Hole 1274A subsea camera survey (Fig. F1) at 0030 hr on 15 June 2003. Our survey began over a sedimented bottom and tracked ~200 m west, up the side of the western wall of the axial valley of the Mid-Atlantic Ridge, following the path of *Shinkai* 6500 Dive 416 (Fig. F2). During this dive all recovered samples were serpentinized peridotite. After passing an outcrop at the depth of the final sample of peridotite collected during the dive, we selected a drilling target with a thin sediment cover (<2 m) to initiate Hole 1274A.

Before beginning our coring operation, we deployed the Water Sampling Temperature Probe (WSTP) to collect a bottom water sample in support of our microbiology program. Coring continued through 155.8 meters below seafloor (mbsf) (Cores 1R to 28R) (Table T1) with little difficulty. The only problems of note were an easily cleared bit blockage experienced after recovering Core 11R and minor amounts of fill collapsing in the hole between pipe connections. Cores 15R, 20R, and 21R were cut as full ~9.6-m intervals (as opposed to the nominal half-cores that we recovered throughout the rest of the hole) due to rapid penetration through those depths (74.0–83.7 and 102.9–122.1 mbsf, respectively). After we recovered Core 28R, the hole collapsed and cut off circulation through the drill string. Pipe was pulled from the hole while attempting to restore circulation, without success, so we released the bit and abandoned Hole 1274A. The average rate of penetration for Hole 1274A was 4.9 m/hr.

F1. Bathymetry and survey track for Hole 1274A, p. 32.

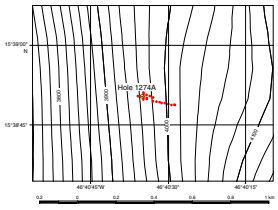

F2. Track and bathymetric section for Site 1274, p. 33.

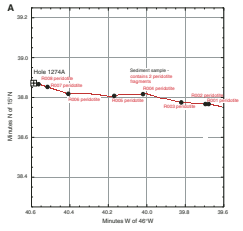

T1. Coring summary, Site 1274, p. 102.

[1]Examples of how to reference the whole or part of this volume.
[2]Shipboard Scientific Party addresses.

IGNEOUS AND MANTLE PETROLOGY

Drilling penetrated to a depth of 155.80 mbsf in Hole 1274A providing 28 cores; total cumulative recovery of 34.65 m of core is 22.2%. The coherent recovery of near meter-long sections in a large number of cores allows characterization of igneous rocks and residues of partial melting at a centimeter scale in the vertical dimension.

The core consists of serpentinized peridotite and dunite with minor amounts of gabbro and oxide gabbro. A curated thickness of 6.61 m of unconsolidated material with harzburgites, dunites, and gabbros was recovered at 97.9–146.1 mbsf. The total cumulative core recovery comprised 93% hard rocks and 7% unconsolidated material. The rock material recovered comprised 77% serpentinized harzburgite, 20% dunite, and the remaining 3% gabbro (Fig. F3).

Based on the lithologic recurrence of very similar peridotites (harzburgite and dunite) throughout Hole 1274A, we could have defined only one lithologic unit. However, a thick fault gouge interval consisting mostly of a fine- to medium-grained matrix of serpentinite mud/clay with clasts of harzburgite, dunite, and gabbro cuts the peridotite sequence. Therefore, we define three stratigraphic units: Unit I is a peridotite sequence that consists mainly of harzburgite, Unit II contains the fault gouge interval and the bulk of the gabbro in the hole, and Unit III is a 2.26-m-long peridotite sequence that is very similar to Unit I.

Lithology and Stratigraphy

Unit I

Interval: Sections 209-1274A-1R-1 through 18R-1
Depth: 0–94.66 mbsf
Lithology: harzburgite

Unit I contains 83% harzburgite (Fig. F4), 16.5% dunite (Fig. F5), and 0.5% gabbro. The top of the sequence is 13 m of recovered (40.3 m drilled) harzburgite with very rare dunite. The modal orthopyroxene contents in harzburgite vary asystematically between 10% and 28% (average = 18% in 80 core intervals as defined in "Site 1274 Visual Core Descriptions"). Clinopyroxene is present as an interstitial phase in all samples but averages <2%, except for a 50-cm-long interval at 0.67 and 1.17 mbsf where its mode is as high as 3% and the orthopyroxene mode is ~25%. Modal spinel averages <1.5% throughout the sequence. At the base of the homogeneous harzburgite section, a sequence of alternating harzburgites and dunites characterizes the bottom of Unit I (40.3–94.7 mbsf). The dunites make their first appearance in the sequence as a few centimeter-thick intervals that alternate with orthopyroxene-poor harzburgite. These dunite bands increase toward the bottom of Unit I to as thick as 70 cm. The harzburgites have, on average, 13.5% modal orthopyroxene (47 core intervals defined in "Site 1274 Visual Core Descriptions") (54.3 m drilled), 5% less than the peridotite above this interval. Harzburgites near dunites have modal orthopyroxene content as low as 8%–10% (Fig. F5). Dunites contain some orthopyroxene (average = 2.5% in 27 samples) and a modest amount of spinel (average = 1%). Plastic deformation and recrystallization below the solidus is minor, and the textures are protogranular. One pebble of harzburgite with a mylonitic texture is present at the top of Core 209-1274A-2R (Fig. F6). A 15-

F3. Lithostratigraphic summary, Hole 1274A, p. 35.

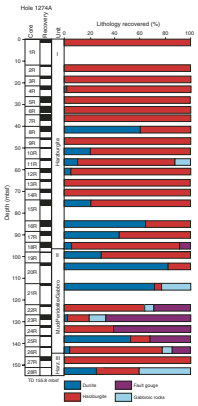

F4. Typical harzburgite, p. 36.

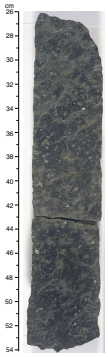

F5. Harzburgite/dunite contact, p. 37.

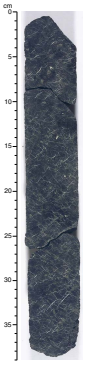

F6. Pebble of mylonitic harzburgite, p. 38.

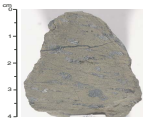

cm-long interval of oxide gabbro, consisting of three pieces, is the only mafic rock found in Unit I.

Unit II

Interval: Sections 209-1274A-18R-1 through 26R-1
Depth: 94.66–142.12 mbsf
Lithology: mud/peridotite/gabbro

Unit II includes nine cores with a cumulative recovery of 8.98 m from 47.5 m drilled (recovery = 18.9%). Unit II contains significant thicknesses of a gray-green unconsolidated mud (Fig. F7). Rounded clasts of dunite and harzburgite (1–2 cm long) are dispersed in the mud matrix. A few intervals (30–60 cm) of dunite and harzburgite were cored between the unconsolidated intervals. The dunite and harzburgite are highly altered and brecciated and are, respectively, 29% and 30% of the total recovery of Unit II. Gabbro is found throughout Unit II (8%). A 20-cm-thick interval of completely rodingitized gabbro found in Core 209-1274A-21R (Fig. F8) contains clinozoisite, garnet, and vesuvianite (see "Alteration of Mafic Rocks," p. 9, in "Hydrothermal Alteration" in "Metamorphic Petrology").

F7. Mud interval from the fault gouge zone, p. 39.

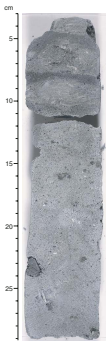

F8. Altered gabbro, p. 40.

Unit III

Interval: Sections 209-1274A-26R-1 through 28R-1
Depth: 142.12–151.38 mbsf
Lithology: harzburgite

Unit III includes two cores (three sections) with a cumulative recovery of 2.09 m from 4.98 m drilled (recovery = 42%). Unit III is similar to Unit I and consists primarily of harzburgite (90% of Unit III recovery). Two horizons of gabbro (6%) and dunite (4%) account for the rest of Unit III. The harzburgite averages 22% orthopyroxene, 1% clinopyroxene, and <1% spinel. The dunite contains as much as 5% orthopyroxene as an anhedral to interstitial phase. Plastic deformation and recrystallization below the solidus are essentially absent, and the textures are protogranular.

Lithologic Characterization

Harzburgite

The harzburgites recovered from Hole 1274A are the freshest (40%–50% of the primary minerals are preserved) drilled so far during Leg 209. They have a coarse protogranular texture and contain a mineral assemblage consisting largely of olivine (70%–90%) and lesser orthopyroxene (10%–28%) with minor amounts of clinopyroxene (<1%–3%) and spinel (1%–2%). There is a gradational decrease in the modal proportion of pyroxene toward dunite at the centimeter scale, but in general the modal proportions of minerals in harzburgite do not show a systematic gradient downhole (Fig. F9). Below, we characterize the textural aspects of the constituent minerals of the harzburgite.

F9. Modal orthopyroxene percentage, p. 41.

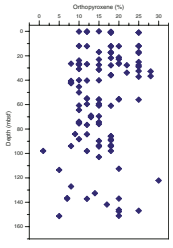

Olivine

Olivine composes >70% of the harzburgite from Hole 1274A. The olivine is moderately serpentinized but is well preserved locally. Determination of the original grain size of olivine in hand sample was not possible because of the pervasive alteration. In thin section, fresh olivine

occurs as small (generally <0.1–1 mm) grains consisting of subangular to subrounded kernels separated by anastomosing serpentine veinlets and secondary magnetite. Optically continuous olivine kernels indicate that the original crystals were considerably larger than 3–4 mm. Small grains of olivine are partially enclosed in the orthopyroxene margins.

Pyroxenes

Orthopyroxene composes as much as 30% of the volume of the peridotites. Most of the orthopyroxene grains are anhedral with smoothly curved grain boundaries at the contact with olivine, typical of protogranular texture in abyssal peridotites (Fig. **F10**). Orthopyroxene margins partially enclose smaller-sized olivine grains, many of which are euhedral. Some orthopyroxene grains are more equant, and these tend to form clusters of several orthopyroxene grains with granular to polygonal grain boundaries. Clinopyroxene is a common interstitial phase along the triple junctions in the orthopyroxene clusters. Subhedral to euhedral spinel is commonly included in orthopyroxene grains, especially in those that are more rounded. Spinel, orthopyroxene, and olivine symplectite are common at or within the margins of anhedral orthopyroxene (Fig. **F11**). These characteristics are also observed in the peridotites from Hole 1272A, and like Hole 1272A harzburgite, Hole 1274A harzburgite has textures and mineralogies characteristic of partial melting residues. Clinopyroxene abundance in harzburgite from Hole 1274A, although low (≤2%), is greater than that in peridotites from Hole 1272A and locally may amount to 3% of the volume of harzburgite. Clinopyroxene occurs as rims or small patches at the tips of anhedral orthopyroxene or all along the margins of large orthopyroxene grains. Generally, clinopyroxene is optically continuous when it rims orthopyroxene (Fig. **F12**). Clinopyroxene also tends to enclose small grains of olivine and orthopyroxene, and we refer to this as poikilitic clinopyroxene (Fig. **F13**). In one thin section (Sample 209-1274A-1R-1, 15–17 cm), a poikilitic clinopyroxene totally encloses an oval orthopyroxene. Clinopyroxene also occurs in association with spinel in symplectitic or granular intergrowths. Symplectites commonly occur at the margins of orthopyroxene and seem to grow toward the olivine. The boundary between orthopyroxene and spinel symplectites is sharp and straight. Rare, relatively large, single crystals of clinopyroxene with intergranular extensions are also present (Fig. **F14**).

Orthopyroxene is affected by minor ductile-brittle deformation that is manifest as incipient breakdown of the coarse protogranular crystals into subgrains. Intergranular clinopyroxene is present at the boundaries of the subgrains (Fig. **F15A**), clearly healing microfractures and crystallizing as small lamellae along kink bands (Fig. **F15B**), and in orthopyroxene cleavages (Fig. **F15C, F15D, F15E, F15F**). Moreover, some microfractures are filled with small grains of olivine, clinopyroxene, and spinel and only clinopyroxene and spinel in other places. Similar crack-filling assemblages are present between larger orthopyroxenes (Fig. **F16A–F16D**). Locally, small clinopyroxene grains with magmatic twinning crystallized between olivine and orthopyroxene grains (Fig. **F17**).

Maximum and minimum grain sizes of orthopyroxene and clinopyroxene in the peridotites of Hole 1274A were estimated during visual core description. Grain size was estimated more accurately from 20 thin sections. Figure **F18** shows that the grain size in Hole 1274A is bimodal.

F10. Orthopyroxene textural relations, p. 42.

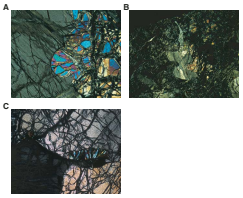

F11. Olivine–orthopyroxene protogranular texture, p. 43.

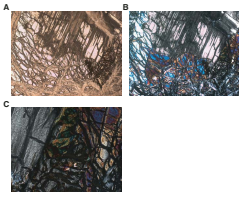

F12. Clinopyroxene, p. 44.

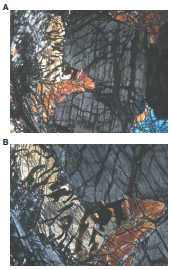

F13. Poikilitic clinopyroxene, p. 45.

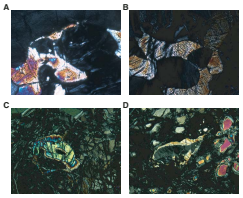

F14. Large clinopyroxene crystal, p. 46.

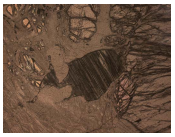

F15. Textural relations of clinopyroxene, p. 47.

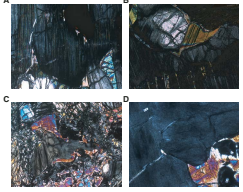

Spinel

Chrome spinel is generally well preserved and composes 1%–2% of the harzburgite and dunite. Spinel shapes, from observation of the entire core, can be divided into three categories, equant, interstitial, and vermicular:

1. Equant: the shape is equidimensional with straight and/or curved surfaces.
2. Interstitial: a transitional category between vermicular and equant. The boundaries of these spinels are commonly curved and have thin tips extending from the corners of the grains.
3. Vermicular: the shape is intricate, forming symplectitic intergrowths with orthopyroxene, clinopyroxene, and/or olivine.

In Hole 1274A, all spinel morphologies are present throughout the hole and many core pieces contain spinel with more than one textural type (Fig. F19). However, in dunite (e.g., Cores 209-1274A-2R to 5R) equant spinel is dominant, whereas in harzburgite (e.g., Cores 8R, 20R, 21R, and 25R) vermicular spinel predominates (Figs. F19, F20, F21). In thin section, spinel in harzburgite is deep red to black in plane-polarized light (indicating variable composition).

Dunite

Dunite is highly serpentinized compared to harzburgite and is composed of olivine and spinel (1%–2% modal) with or without pyroxene (<10% modal). Relict olivine generally composes <10% of the dunite, but locally, clusters of olivine kernels are preserved. Spinel is euhedral to subhedral and is brown to deep brown. Orthopyroxene in dunite is anhedral and has curved contacts with olivine, typical of protogranular textures. Small clinopyroxene crystals associated with spinel are present along some orthopyroxene grain edges. This microstructure is identical to that in the harzburgite, except that orthopyroxene in dunite may also contain subhedral, 1-mm-size spinel inclusions. Clinopyroxene associated with orthopyroxene locally forms relatively large patches of two or more grains with spinel, as in the harzburgite. Relics of vermicular intergrowths of spinel and clinopyroxene are between olivine grains or are elongated lenses crosscutting the olivine matrix (Fig. F22A, F22B). Polygonal, poikilitic clinopyroxene enclosing small olivine grains and rimmed by symplectitic spinel-clinopyroxene intergrowth is present at olivine grain junctions. In thin section, Sample 209-1274A-8R-1, 109–111 cm, shows four 1-mm euhedral spinels at olivine junctions and four spinel-clinopyroxene symplectitic intergrowths. In thin section, Sample 209-1274A-15R-1, 23–26 cm, shows 1-mm euhedral spinel and a few pseudomorphs of spinel-clinopyroxene symplectite. These symplectitic relics may have replaced former orthopyroxene. Most symplectites are along orthopyroxene grain boundaries in the harzburgites.

Gabbros

The first occurrence of gabbro in Hole 1274A is in Unit I at a depth of ~55 mbsf in interval 209-1274A-11R-1 (Pieces 9–11, 41–56 cm) (Fig. F23). The gabbro is rather fresh and rich in oxide (~12%, mainly ilmenite) and contains 64% plagioclase, 16% clinopyroxene, 4% olivine, and 2% orthopyroxene as primary magmatic phases. Based on its pri-

F16. Orthopyroxene grain-size reduction, p. 49.

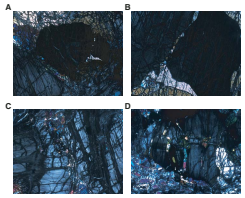

F17. Euhedral clinopyroxene and twinning, p. 50.

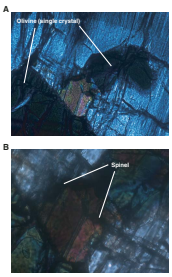

F18. Orthopyroxene and clinopyroxene in peridotites, p. 51.

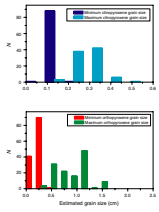

F19. Observed spinel shape in dunite and harzburgite, p. 52.

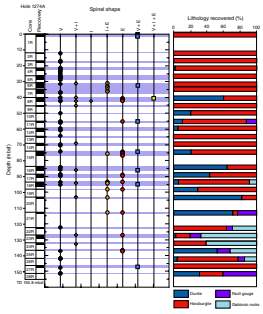

F20. Distribution of spinel shape in dunite and harzburgite, p. 53.

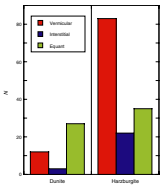

mary mineralogy, this rock is an oxide gabbro. In thin section (Sample 209-1274A-11R-1 [Piece 10, 46–49 cm]), the rock appears to have recrystallized and the original igneous texture is destroyed. Triple junctions between crystals (120°) (Fig. F24) suggest high-temperature annealing. Substantial recovery has occurred, leading to coarsening of neoblasts. Plagioclase twins are bent, indicating deformation (Fig. F25). Olivine is associated with clinopyroxene, except for a small patch of olivine associated with oxide. Plagioclase contains sulfide inclusions that could be primary igneous phases.

The bulk of the gabbroic rocks in this hole are in Unit II. In hand specimen, they are similar to each other. All are extensively altered, so their original lithology and texture are obscured. The contact between gabbroic rocks and the host peridotite is preserved in many pieces of Cores 209-1274A-21R, 22R, and 23R (Fig. F26). At the contact there appears to be a reaction rim separating gabbroic rocks from harzburgite. Primary mineralogy has been inferred from two thin sections (Samples 209-1274A-21R-1 [Piece 5, 12–17 cm] and 21R-1 [Piece 23, 93–98 cm]) and from interpretation of alteration products and pseudomorphs of the primary minerals. These gabbros likely contained variable amounts of plagioclase (45%–60%), clinopyroxene (29%–45%), orthopyroxene (7%–8%), and oxides (3%). Fresh clinopyroxene (5%) is still preserved in interval 209-1274A-21R-1 (Piece 5, 12–17 cm). The presence of orthopyroxene is inferred based on pseudomorphs with a lattice of oxides. Thus, we classify the gabbroic rocks of Unit II as gabbronorites.

A small amount of gabbroic material is also present in Unit III. It appears similar to gabbroic rocks in Unit II. No contacts were recovered between gabbroic rocks and host peridotite in Unit III.

Discussion

Site 1274 harzburgites display mineralogical and textural characteristics similar to those of Site 1272. In particular, peridotites from both sites have a protogranular texture. The low abundance of residual clinopyroxene and the dark red chromium spinel (that usually corresponds to high chromium numbers, i.e., high degrees of melting) suggest that the harzburgites from Hole 1274A are very depleted, in accordance with geochemical investigations on dredged peridotite samples from the same region (Bonatti et al., 1992; Sobolev et al., 1992a, 1992b; Cannat and Casey, 1995; Cannat et al., 1992; Dick and Kelemen, 1992). Clinopyroxene, locally with magmatic twinning, occurs as an interstitial phase, with or without symplectitic intergrowths of spinel, olivine, and orthopyroxene in both harzburgite and dunite from Sites 1272 and 1274. This texture was described in abyssal peridotite samples by Seyler et al. (2001) and has been interpreted to result from the crystallization of interstitial melt in the residual solid at the end of partial melting. The occurrence of intergranular clinopyroxene along subgrain boundaries in orthopyroxene indicates that the crystallization of the clinopyroxene occurred during or just after orthopyroxene deformation. However, at Site 1274 the interstitial clinopyroxene is more abundant than at Site 1272 and forms better-developed crystals along orthopyroxene grain boundaries and within cracks between orthopyroxene subgrains. Based on the logic of Seyler et al. (2001), we suggest that the amount of crystallized melt was large (>2 vol%) (see discussion in Seyler et al., 2001). Perhaps this is related to the relatively cold thermal regime in the shallow mantle adjacent to the 15°20′ Fracture Zone. An alternative is that a genetically unrelated melt could have impregnated the perido-

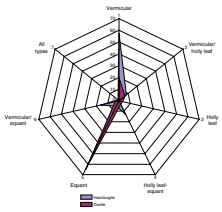

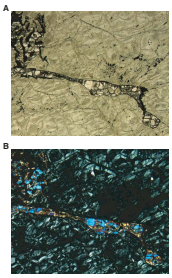

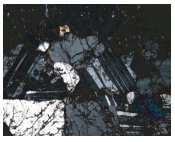

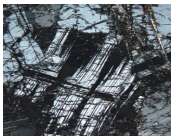

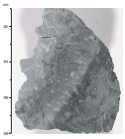

tite during upwelling. A third hypothesis calls for partial melt accumulation at the top of the melting column. Finally, it could be that all or much of the clinopyroxene, together with some associated spinel, was exsolved from high-temperature orthopyroxene during cooling of the harzburgites.

At Site 1274, dunite is not very abundant. However, it is important to note that interstitial clinopyroxene occurs in dunite as well as in harzburgite and the contacts between harzburgite and dunite are gradational. Possibly, the dunite is a simple residue of melting, formed by more extensive melt extraction compared to the harzburgite. Orthopyroxene in dunite, with or without spinel-clinopyroxene symplectites, could also be relics of dissolved or reacted orthopyroxene, suggesting the formation of dunite by dissolution of orthopyroxene from harzburgite.

METAMORPHIC PETROLOGY

A total of 34.65 m of highly to completely serpentinized harzburgite and minor very highly to completely serpentinized dunite was recovered from Hole 1274A. Altered gabbroic intrusive rocks are present only in some short intervals.

The ultramafic rocks show a systematic downhole increase in the total extent of serpentinization. In the upper 60 mbsf, up to 35% of the primary igneous phases (olivine, orthopyroxene, and clinopyroxene) are preserved, representing the least altered peridotite unit drilled at Sites 1268–1274. In some intervals, the serpentinized ultramafic rocks have been affected by cataclastic deformation, resulting in the formation of fault gouges. Oxidative carbonate–iron oxyhydroxide–clay alteration is prominently developed along aragonite veins and extends to ~90 mbsf. Brucite alteration is particularly well developed in dunite. Thin section observations indicate that olivine is replaced by brucite-serpentine-magnetite assemblages.

Vein alteration is dominated by black serpentine-magnetite and white chrysotile veins. The chrysotile veins are transgranular as well as paragranular. The paragranular vein type is particularly common in proximity to shear zones. Carbonate and iron oxide veins are limited to the upper part of Hole 1274A and are related to late-stage circulation of cold, oxygenated seawater.

Hydrothermal Alteration

Alteration of Ultramafic Rocks

The grayish black to black harzburgites and dunites of Hole 1274A are highly to completely serpentinized. Alteration products include serpentine after olivine and orthopyroxene, brucite, serpentine, and magnetite after olivine and minor talc and tremolite after clinopyroxene and orthopyroxene. Spinel is commonly fresh or slightly altered to magnetite. In partially serpentinized rocks, olivine is generally more altered than orthopyroxene. Clinopyroxene is only moderately altered to talc and tremolite. In the uppermost 60 m of Hole 1274A, the degree of orthopyroxene alteration averages 50%–60%, while that of olivine is 80%. Olivine alteration in this interval produced only trace amounts of magnetite. Very highly to completely altered harzburgite and dunite from deeper in Hole 1274A show noticeable amounts of magnetite,

commonly in diffuse magnetite-serpentine veinlike networks that appear to trace former olivine grain boundaries and cracks (mesh-rim texture). Qualitatively, the downhole increase in the proportion of magnetite observed in thin sections appears to correlate with an increase in magnetic susceptibility downhole (see **"Paleomagnetism,"** p. 22).

X-ray diffraction (XRD) results indicate that the secondary mineral assemblage is dominated by serpentine, minor brucite, and magnetite (Table **T2**). Brucite appears more abundant in dunites (e.g., Sample 209-1274A-20R-1, 141–144 cm) (Fig. **F27**), whereas in harzburgites, brucite may be absent or represent only a trace component (e.g., Sample 17R-2, 16–19 cm) (Fig. **F28**).

The ultramafic rocks from Hole 1274A show an interesting variety of microtextures that involve relict orthopyroxene and olivine as well as the alteration products serpentine, magnetite, and brucite. Specifically, three different types of mesh textures are developed: (1) mesh rims of serpentine and magnetite, (2) relict kernels of olivine surrounded by serpentine and magnetite and/or brucite (Fig. **F29A, F29B**), and (3) brucite kernels surrounded by serpentine and a trace of magnetite (Fig. **F29C**). Individual thin sections commonly show various combinations of these types of mesh texture. Unlike the fibrous brucite in Holes 1271A and 1271B, which could be clearly distinguished from fibrous serpentine based on its optical orientation (length-fast), apparent fibers of brucite in thin sections of serpentinites from Hole 1274A are length-slow. Similar brown kernels were observed in mesh-textured serpentinites from Site 920 and were identified by electron microprobe analyses as finely intergrown brucite and serpentine (Dilek et al., 1997). The optical orientation of these aggregates suggests that the serpentine is lizardite. Direct replacement of olivine by lizardite and brucite (magnetite) is common during serpentinization at relatively low temperatures of ~200°C (e.g., Sanford, 1981; O'Hanley, 1996). Nonpseudomorphic ribbon textures are also very common in Hole 1274A, and both mesh and ribbon textures are commonly developed in single thin sections. Ribbon textures consisting dominantly of chrysotile (apparent fibers are length-slow) replace mesh textures, in particular in sections of the hole where paragranular chrysotile veins are abundant. Ribbon textures and paragranular chrysotile veins locally impose a foliated fabric on the rock.

Systematic downhole variations in the degree of serpentinization of ultramafic rocks were observed in Hole 1274A (Fig. **F30A, F30B**). In the uppermost 100 m of the hole, the degree of alteration increases from 60%–70% to >95%. Between 60 and 95 mbsf, alteration intensities vary between 70% and 100%. Below a prominent fault gouge zone in Section 209-1274A-18R-2 at ~95 mbsf, alteration intensity is generally very high to complete (>95%). In the lowermost 2 m recovered from Hole 1274A, alteration intensities drop again slightly to values between 85% and 95%. These variations in the estimated degrees of alteration are mirrored by changes in rock density, thermal conductivity, compressional velocity, and porosity (see Figs. **F55, F30A, F30B**).

The uppermost 90 m of Hole 1274A is affected by oxidative seawater alteration forming prominent centimeter-wide reddish to brownish halos along carbonate veins (Fig. **F31**), which account in some intervals for as much as 15 vol% of the hole (Fig. **F30C**). This type of alteration is commonly restricted to pieces with white carbonate veins, although these are not always preserved and may have been broken off the margins of individual pieces during drilling.

T2. XRD analyses, p. 103.

F27. Brucite alteration in dunite, p. 60.

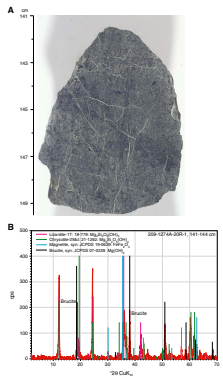

F28. Serpentinized harzburgite, p. 61.

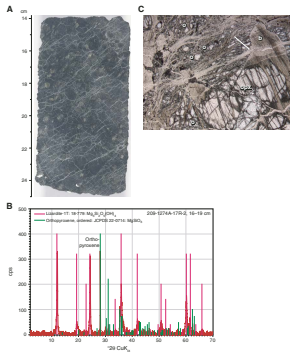

F29. Kernels of olivine and brucite, p. 62.

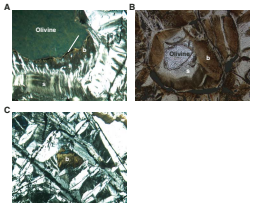

F30. Variability of alteration intensity, p. 63.

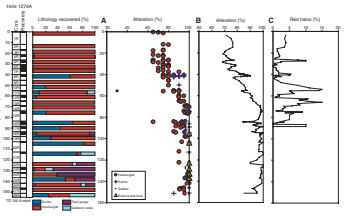

Alteration in Fault Gouges

The fault gouges of Sections 209-1274A-22R-1 to 26R-1 are composed mainly of serpentine and minor magnetite. Two different varieties, one greenish and the other grayish black, can be distinguished. XRD analyses of two fault gouge samples from Section 209-1274A-23R-2 (Table T2) identified serpentine and magnetite in the greenish variety of interval 23R-2, 0–3 cm (Fig. F32A, F32B) and serpentine, magnetite, and nontronite in the grayish black variety of interval 23R-2, 67–70 cm (Fig. F32C, F32D). Intervals of gravel within these fault gouges include centimeter-sized fragments of white asbestiform chrysotile (e.g., Sample 209-1274A-18R-2, 6–13 cm) (Table T2).

Alteration of Mafic Rocks

An oxide gabbro in Section 209-1274A-11R-1 is moderately altered to green amphibole, chlorite, prehnite, talc, and serpentine. Fibrous green amphibole is the most abundant secondary mineral, replacing plagioclase, clinopyroxene, and orthopyroxene. Minor replacement of plagioclase by blocky, bowtie-structured prehnite is patchy (Fig. F33A). Olivine is 50% altered to serpentine.

Gabbros in the lowermost 70 m of Hole 1274A are completely altered and show variable degrees of rodingitization (e.g., see hand specimen shown in Fig. F33B), which is most pronounced at the contacts between gabbro and harzburgite/dunite. Chlorite and amphibole are the most abundant secondary phases and replace plagioclase and pyroxenes. Fe-Ti oxides are replaced by magnetite and titanite, although exsolution/oxidation lamellae of ilmenite are usually preserved. Plagioclase is variably altered to calcium silicates, including prehnite, zoisite (Fig. F33C), hydrogrossular andradite (Fig. F33D), and vesuvianite.

Vein Description

In Hole 1274A metamorphic veins account for 1.8 vol% of the recovered drill core (Table T3). Figure F34 shows the distribution of mineral phases identified in the veins by macroscopic observation. As at Site 1272, serpentine minerals (87.2%) dominate the mineralogy of veins in Hole 1274A. The relative proportions of chrysotile and picrolite vary downhole (Fig. F35A). Picrolite veins are rare in the uppermost 40 m of Hole 1274A. Black picrolite-magnetite veins are more abundant than chrysotile veins between 40 and 55 mbsf and in the lowermost 70 m of the hole (Fig. F35A, F35C). Paragranular chrysotile veins are most abundant between 25 and 35 mbsf and from 57 to 70 mbsf (Fig. F35B). Carbonates, mainly aragonite, account for 11.3% of the veins. These veins are present in variable abundance in the uppermost 90 m of Hole 1274A, with a maximum at ~60 mbsf (Fig. F35C). Minor phases in metamorphic veins are magnetite (1.0%) as well as iron oxyhydroxide, clay, and sulfide (combined = 0.4%) (Fig. F34).

Two major serpentine vein generations, (1) black serpentine-magnetite veins and (2) white cross-fiber chrysotile veins, are present in varying proportions throughout Hole 1274A. Black serpentine-magnetite veins are clearly the earliest generation and form either diffuse vein networks or sets of subparallel, transgranular veins. White, thin chrysotile veins crosscut the black serpentine-magnetite veins. In some intervals (e.g., interval 209-1274A-15R-1, 8–17 cm), two different chrysotile vein types are present: (1) paragranular, nonbranched, sigmoidal veins and

F31. Orange-brown halos along aragonite veins, p. 64.

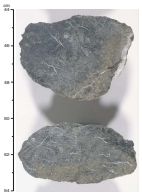

F32. Serpentine mud breccias, p. 65.

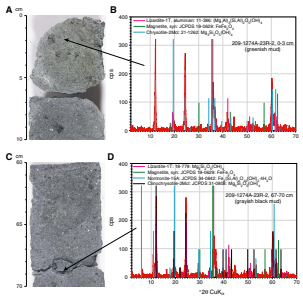

F33. Prehnite, zoisite, and andradite, p. 66.

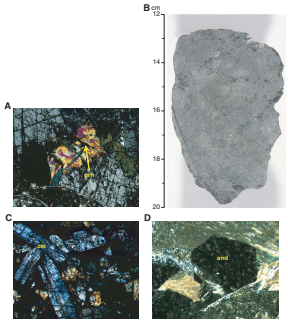

T3. Vein mineralogy, p. 104.

F34. Proportions of vein minerals, p. 67.

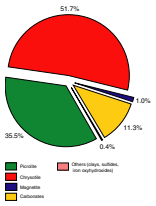

F35. Mineral abundances in veins, p. 68.

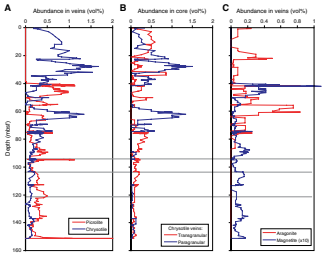

(2) transgranular, irregular, thin, occasionally branched veins. Both transgranular and paragranular serpentine veins occur throughout Hole 1274A. Locally present, green, massive picrolite and white and green composite picrolite-chrysotile veins cut black serpentine-magnetite and are cut by chrysotile veins.

Gray to white carbonate veins are present in the upper 90 m of Hole 1274A (Figs. **F31, F35C**). They are mainly composed of aragonite and contain minor clays and iron oxyhydroxides. These veins have centimeter-wide orange to brownish halos in the serpentinized harzburgites and dunites, which are, in the uppermost 40 m, strictly associated with aragonite veins. The aragonite veins and associated oxidized halos represent a late stage in the metamorphic evolution of the crust at Site 1274 and can be related to circulation of oxygenated seawater at low temperatures.

The short intervals of gabbro in Hole 1274 host only minor green picrolite veins.

Discussion

The variations in the degree of serpentinization of ultramafic rocks provide the opportunity to examine possible reaction paths of serpentinization at Site 1274. Where serpentinization is incomplete (as low as 60%), magnetite is rare, suggesting that significant magnetite formation does not begin until >60% of the primary rock is serpentinized. This observation is consistent with the sequence of serpentinization reactions proposed by Toft et al. (1990) to explain density–magnetic susceptibility relationships in variably serpentinized harzburgites from ophiolites. These authors suggested that initial serpentinization produces iron-rich serpentine and iron-rich brucite and that magnetite forms during recrystallization of these phases as serpentinization proceeds.

Temperature-pressure stabilities of serpentine phases are not well constrained. Thermodynamic calculations predict that antigorite is the stable serpentine phase >200°–300°C and pressures <2 kbar and that chrysotile and lizardite form from antigorite during low-temperature recrystallization (e.g., Evans, 1977; Dilek et al., 1997). Consistent with this view, an early oxygen isotope study of serpentinites suggests formation of lizardite and chrysotile at temperatures <235°C (Wenner and Taylor, 1971). However, more recent stable isotope investigations (Agrinier et al., 1995; Früh-Green et al., 1996; Agrinier and Cannat, 1997), field studies (O'Hanley and Wicks, 1995; Wicks and Whittacker, 1977), and hydrothermal experiments (Normand et al., 2002; Janecky and Seyfried, 1986; Allen and Seyfried, 2003) indicate that lizardite and chrysotile form directly from olivine at temperatures well above 300°C. The phase relations proposed by Evans (1977) assume that $P(H_2O) = P_{total}$. However, Sanford (1981) and O'Hanley (1996) demonstrated that the lizardite + brucite stability field extends toward higher temperatures if $P(H_2O) < P_{total}$. Whereas $P(H_2O) = P_{total}$ is expected in prograde metamorphism, during retrograde serpentinization of oceanic peridotites $P(H_2O)$ is likely to be less than P_{total} because H_2O is consumed, H_2 and CH_4 are produced, and the fluid may be under hydrostatic rather than lithostatic pressure. Moreover, the nucleation energy of (sheetlike) lizardite after olivine is lower than that of (needlelike) antigorite because of a larger interfacial (olivine-lizardite) surface area (Normand et al., 2002). Lizardite may hence form at lower levels of supersaturation than antigorite (and chrysotile), and metastable replacement of olivine by lizard-

ite may be kinetically more favorable than the formation of antigorite, even if formation of the latter is predicted thermodynamically.

In Hole 1274A alteration of clinopyroxene to talc and tremolite is consistent with results of hydrothermal reaction experiments at 400°C and 500 bar (Allen and Seyfried, 2003):

$$\underset{\text{clinopyroxene}}{6\,CaMgSi_2O_6} + \underset{\text{orthopyroxene}}{6\,MgSiO_3} + 5\,Mg^{2+} + 9\,H_2O \rightarrow \underset{\text{serpentine}}{3\,Mg_3SiO_5(OH)_4}$$

$$+ \underset{\text{talc}}{Mg_3Si_4O_{10}(OH)_2} + \underset{\text{tremolite}}{CaMg_5Si_8O_{22}(OH)_2} + 4\,Ca^{2+} + 2H^+.$$

These authors also suggest that pyroxenes react with aqueous fluids faster than olivine does at temperatures >300°C. Breakdown of pyroxene and the associated release of Ca^{2+} (see equation above) to the interacting hydrothermal fluids may be related to the partial rodingitization of the gabbroic units in Hole 1274A. Rodingitization probably takes place at temperatures between 300° and 400°C (e.g., Bideau et al., 1991; Dilek et al., 1997), which coincides with the temperature interval at which pyroxene breakdown is expected to proceed rapidly.

As discussed in **"Metamorphic Petrology,"** p. 9, in the "Site 1271" chapter, the formation of brucite is not expected to be associated with the breakdown of pyroxene because the high silica activity of fluids reacting with pyroxene would prevent brucite formation and would cause previously formed brucite to react to serpentine according to the reaction:

$$\underset{\text{brucite}}{3\,Mg(OH)_2} + 2\,SiO_{2\,(aq)} = \underset{\text{serpentine}}{Mg_3Si_2O_5(OH)_4} + H_2O.$$

The presence of both brucite and partially serpentinized pyroxene may indicate local disequilibria during the main stage of serpentinization. However, it is more likely that the formation of serpentine + brucite + magnetite after olivine took place at a later stage, at temperatures <250°C. In contrast to the main stage of serpentinization, magnetite that accompanies serpentine and brucite appears to form directly from olivine breakdown. The following reaction can possibly account for this observation:

$$\underset{\text{olivine}}{2\,Mg_{1.8}Fe_{0.2}SiO_4} + 2.766\,H_2O = \underset{\text{serpentine}}{Mg_3Si_2O_5(OH)_4} + \underset{\text{brucite}}{0.6\,Mg(OH)_2}$$

$$+ \underset{\text{magnetite}}{0.133\,Fe_3O_4} + 0.133\,H_{2\,(aq)}.$$

The presence of nontronite in serpentine muds indicates that water-rock reactions continued at low temperatures and under oxidizing conditions. This is also suggested by the development of aragonite veins with oxidation halos in the uppermost 90 m of Hole 1274A. The aragonite veins disappear abruptly below the first fault gouge at 95 mbsf. Either the fault gouge represents a hydrogeological barrier that prevents cold seawater from penetrating deeper into the basement or the fault zone accommodates the strain so that fracturing and circulation of cold seawater is limited to the hanging wall of the gouge.

STRUCTURAL GEOLOGY

We present the results of structural observations of the core recovered from Hole 1274A, followed by a discussion of some of the problems in interpreting the crystal-plastic deformation. Three categories of observations were recorded in spreadsheet format (see the "Supplementary Materials" contents list): crystal-plastic deformation, alteration veins, and brittle deformation. These were supplemented by microstructural observations in 34 thin sections. The peridotites from this site were the freshest drilled during this leg (as much as 40% fresh olivine in harzburgite). However, pervasive alteration has led to some ambiguity in the interpretation of observed features. Details of the structural classification scheme for each feature are given in "Structural Geology," p. 9, in the "Explanatory Notes" chapter.

Crystal-Plastic Deformation

High-Temperature, Low Strain–Rate Deformation

The harzburgites and dunites from Hole 1274A have undergone very little high-temperature crystal-plastic deformation. They are coarse grained and have mostly protogranular textures with only a few examples of weakly porphyroclastic harzburgite (~3% of the core). The protogranular textures are characterized by smooth, curved grain boundaries and range from simple equigranular grains (Fig. F36A) to grains with protruding lobes and included olivine (Fig. F36B, F36C). The grain interiors have minor broad, undulose extinction of some grains and, occasionally, subgrain boundaries in olivine. The average olivine and orthopyroxene grain size is difficult to determine, but most of the volume appears to be occupied by grains >5 mm, ranging to 20 mm in diameter. Small vermicular spinel grains associated with orthopyroxene or clinopyroxene are ubiqitous; much larger lobate spinels are also present in some thin sections. These textures may be interpreted as the result of grain boundary–controlled diffusion creep during mantle upwelling and melting. However, the lobate, intergrown shapes of many grains (Fig. F36D) together with the great abundance of delicate interstitial and intragranular late magmatic spinel grains (see "Igneous and Mantle Petrology," p. 2) suggests that some of the earlier fabrics may have been overprinted during late-stage melt-rock reaction at the base of the lithosphere.

Some indications of high-temperature deformation are present within the harzburgites. These include kink bands with neoblasts in orthopyroxene, as well as neoblasts along some grain boundaries (Fig. F37A, F37G). Relatively closely spaced subgrain boundaries in olivine are also present (Fig. F37C). In interval 209-1274A-5R-2, 17–20 cm, arrays of kink band boundaries with clinopyroxene exsolution have formed in some orthopyroxene grains (Fig. F37B). Patches of orthopyroxene grains that are significantly smaller than the average grain size are also present in some sections (Fig. F37D, F37E, F37F). Intergranular clinopyroxene and intergrowths of olivine, orthopyroxene and clinopyroxene, and vermicular spinel suggests that the formation of these fine-grained patches is concurrent with the formation of the protogranular texture. Only rarely do high-temperature deformation features begin to dominate the Hole 1274A harzburgite fabrics, producing narrow intervals of weakly deformed harzburgite (crystal-plastic deformation intensity = 1) (Figs. F38, F39; Table T4).

F36. Protogranular orthopyroxenes in harzburgites, p. 69.

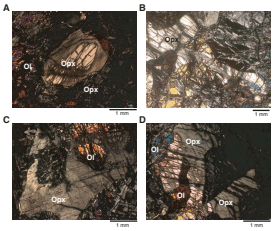

F37. High-temperature deformation textures in harzburgites, p. 70.

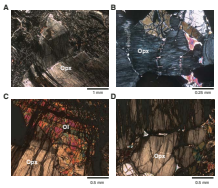

F38. Deformation and alteration vein intensities with depth, p. 72.

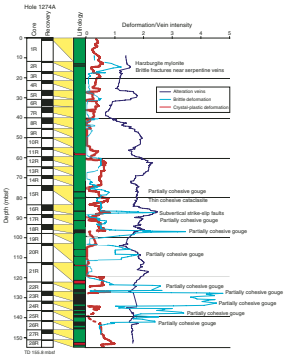

F39. Crystal-plastic deformation intensity, p. 73.

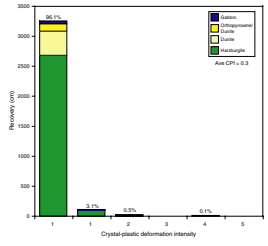

T4. Crystal-plastic deformation intensities, p. 105.

High Strain–Rate Deformation

A single weathered pebble of peridotite mylonite recovered at the top of Core 209-1274A-2R appears out of place, as none of the adjacent pieces of core show the effects of weathering or a similar style of deformation. Therefore, it is possible that the mylonite is a piece of rubble that fell into the hole.

This mylonite consists of orthopyroxene porphyroclasts in a matrix of finely recrystallized olivine (Fig. F40A). Individual orthopyroxene porphyroclasts have length:width ratios of 5:1 (Fig. F40C) and often consist of complex arrays of kink bands (Fig. F40B) formed subparallel to the foliation plane. Relatively coarse, less recrystallized patches of olivine constitute enclaves or even augen within the finer-grained olivine matrix. Once formed, the finer-grained matrix can deform by diffusion creep rather than dislocation creep and is therefore weaker than the remaining enclaves of unrecrystallized olivine (Jaroslow et al., 1996). Locally, undeformed enclaves of olivine and spinel are also present in the mylonite, with the spinel grains terminating abruptly at the margins of the enclave, indicating that the mylonitic deformation took place after spinel crystallization (Fig. F40D).

Abyssal peridotite mylonites similar to this one constitute ~10% of dredged abyssal peridotites, mostly from oceanic transforms (Dick, 1989) and represent high-temperature (granulite to lower amphibolite) fault zones (Jaroslow et al., 1996). Given the style of deformation and its location at the top of the section, this fragment may indicate that the uppermost few meters of the outcrop are part of a mylonitic shear zone associated with unroofing of the peridotite block sampled in Hole 1274A.

F40. Deformation textures in harzburgite mylonite, p. 74.

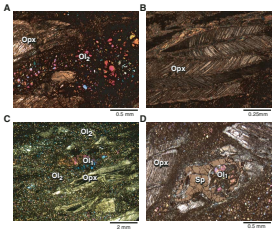

Crystal-Plastic Foliations

Fifteen crystal-plastic or protogranular shape fabrics were measured in the Hole 1274A harzburgites. These fabrics were rare and hard to find, and all were determined by examination of the core with the binocular microscope. In many cases these foliations were very weak. These fabrics are defined by smaller intergranular pyroxenes and rare arrays of lineated spinels at a high angle to the serpentine foliation (cf. Ceuleneer and Cannat, 1997). It is not clear whether they represent crystal-plastic deformation or late crystallization of intergranular pyroxene and spinel from a melt migrating through the peridotite—or some combination of both. Because of their weak development, measuring the orientation of these fabrics on anything other than the cut face of the cores was impossible. Therefore, the measurements are of apparent dips in the cut face of the core, which was generally oriented parallel to the dip of the pervasive serpentine foliation in the Hole 1274A peridotites (see below). The apparent dips are shown as a pole figure in the core reference frame (Fig. F41A).

A plot of poles to the foliations, rotated into a common reference frame using the measured paleomagnetic declination, shows that they appear to be coherently oriented (Fig. F41B). This is a surprising result, as a simple plot of apparent dips, measured in the cut face of the core, would likely give a random scatter within a cone of error in the stereo plot. This result may imply some systematic relationship between the pyroxene and spinel shape fabrics and the serpentine foliation as the core was systematically split parallel to the dip of the serpentine foliation. This could reflect formation of the pyroxene and serpentine fab-

F41. Poles to crystal-plastic foliations, p. 75.

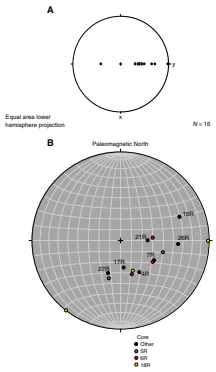

rics in similarly oriented stress fields, preferred formation of the serpentine fabric along preexisting planes of weakness related to the pyroxene fabric, or a coincidental clustering of data points from a small number of difficult and uncertain measurements.

With two exceptions in Section 209-1274A-18R-1 at 94.6 and 95.4 mbsf (expanded depth), the poles to foliation form a girdle in Figure F41B. The two outlying points represent foliations measured in peridotites just above the major fault gouge found at 94 mbsf and thus may reflect rotations due to late faulting. Another foliation, measured 40 cm higher in the same core, dips at 30°, similar to the 25° dip measured in the overlying Section 209-1274A-17R-2. There is no systematic variation in the dip of the measured foliation with depth in Hole 1274A. Thus, the girdle of poles in Figure F41B might represent outcrop-scale folding on the scale of tens of meters.

Postintrusion Crystal-Plastic Deformation

Late oxide gabbro or gabbronorite dikes were found in several intervals in the Hole 1274A core, concentrated near the bottom. Secondary minerals largely replace the dikes, and many are completely rodingitized. They preserve sharp contacts with peridotite, with pseudomorphed pyroxene locally perpendicular to these contacts. This indicates intrusion of the gabbroic dikes into the mantle peridotite at relatively high temperatures (probably >600°C). Patches of relict clinopyroxene and plagioclase are often undeformed but in other cases record a weak to moderate crystal-plastic deformation with the formation of abundant plagioclase deformation twins (Fig. F42A) and patches of polygonal neoblasts replacing strained plagioclase grains (Fig. F42B). In at least one case, partially replaced Fe-Ti oxides are intergranular to clinopyroxene neoblasts. The average deformation grade of the gabbros = 0.5, the highest of any lithology recovered, and is consistent with observations at Sites 1268 through 1272 that strain is partitioned into the gabbros relative to the peridotites during high-temperature deformation. A downhole plot of crystal-plastic deformation intensities is shown in Figure F38.

F42. Deformation textures in a weakly deformed oxide gabbro, p. 76.

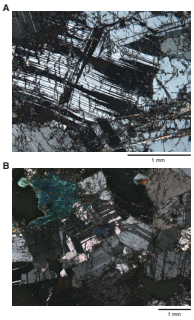

Cross-Fiber Serpentine Foliation

Cross-fiber serpentine foliation at Site 1274 is variable and appears to vary with the degree and style of serpentinization. Harzburgite containing more than ~30% fresh olivine is cut by numerous fine (<0.1 mm wide) anastomosing serpentine and magnetite veins that form pervasively through the body of the rock during the main phase of serpentinization. They can have preferred orientation or occur randomly. Where veins have a preferred orientation, they define a fairly strong foliation visible in thin section. Harzburgite containing less than ~30% fresh olivine is generally dominated by strong ribbon texture serpentine (O'Hanley, 1996), which defines a consistent planar to slightly anastomosing foliation (Fig. F43). Alternating zones of highly serpentinzed and fresher material appear to form layered bands in the core ranging 1–3 cm in width. These bands define a faint foliation in many locations that is generally parallel to fine serpentine veins and ribbons. These serpentine bands are deflected around clusters of large pyroxene porphyroclasts or are deflected into areas with lower than average pyroxene proportion. In some locations the serpentine bands are aligned perpendicular to the predominant long axis of pyroxene grains. Cross-fiber ser-

F43. Partially serpentinized harzburgite, p. 77.

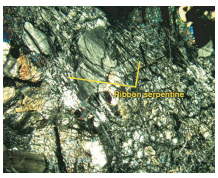

pentine foliation is present in most dunite samples as serpentine ribbons and magnetite veins. These define a planar to slightly anastomosing foliation in most samples.

Alteration Veins

The harzburgites and dunites of Hole 1274A contain four generations of alteration veins (Fig. F44). The first consists of planar to curved, thin (<1 mm wide) black magnetite-serpentine veins (Fig. F44D, F44F) that are more readily seen in the dunites (e.g., Section 209-1274A-8R-1) and at the top of the core (Section 1R-1) where they are not obscured by later generations of veins. The second generation consists of rare planar (<2 mm wide) pale green-white picrolite veins (Fig. F44D, F44E) that are best developed in the dunites (e.g., Section 209-1274A-8R-1) and at the base of the core next to the fault zones (Cores 20R to 25R).

The third and most abundant generation of veins consists of small (1 cm long) planar to sigmoidal chrysotile veins (Fig. F44A). These veins occur throughout the harzburgites within the core but are less numerous in the dunite horizons (40–59 and 100–120 mbsf) (Figs. F44D, F45). They are composed of white chrysotile and occasionally white chysotile with pale green picrolite centers. The veins are dilational, often defining a distinct foliation (Fig. F44A, F44G) and sometimes form conjugate sets (Fig. F44B). The foliation dips 20°–90°, most commonly 30°–60°, with the dominant dip decreasing downcore (Fig. F45). Rarely, the veins show no foliation and instead form an irregular mesh or anastomosing network of veins (Fig. F44C).

The final generation of veins consists of late aragonite-carbonate veins (Fig. F44G) and associated oxides that fill planar to irregular brittle fractures (up to 8 cm long) and crosscut all three earlier generations of veins. The carbonate veins are confined to the upper 90 m of the core (Fig. F45) above the major fault zones in the bottom of the hole. Crosscutting relationships for all four generations of veins are shown in Figure F44D, F44E–F44G.

The intensity and orientation of veins were measured using the intensity scale outlined in "Structural Geology," p. 9, in the "Explanatory Notes" chapter. The intensity of these veins is a measure of their average frequency in a 10-cm piece of core. The variation in total vein intensity with depth for Hole 1274A is shown in Figure F38. Alteration vein intensity is generally low (intensity ≤ 2.5) and is significantly lower than the vein intensity in the peridotites at Sites 1268, 1270, and 1271. However, the vein intensity is greater than that in the altered peridotites of Hole 1272A. This may simply be an artifact of the high degree of alteration shown throughout Hole 1272A, which may have obliterated some chrysotile veins. The average alteration vein intensity in Hole 1274A is slightly lower in the top 50 m of the hole than in the rest of the hole. This variation corresponds to the degree of alteration shown in the core (see "Metamorphic Petrology," p. 7). Some local peaks in the intensity curve appear to coincide with peaks in the brittle deformation intensity curve, suggesting that some of the veining can be correlated with brittle deformation. However, pervasive serpentinization appears to have preceded the brittle deformation shown by these rocks.

A total of 41 chrysotile foliation orientations that could be reoriented with the paleomagnetic data were measured in the core. Figure F46 shows a lower hemisphere plot showing the poles to the chrysotile foliation, restored with the declination of the stable remnant magnetization pointing north as discussed in "Structures in Peridotite and

F44. Alteration veins in harzburgites and dunites, p. 78.

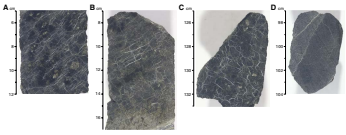

F45. Dips of veins and foliation, p. 80.

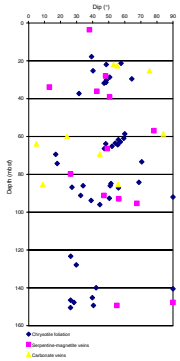

F46. Poles to brittle shear zones and chrysotile foliation, p. 81.

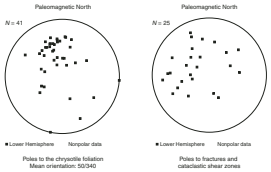

Gabbroic Intrusions," p. 8, in "Mantle Upwelling, Melt Transport, and Igneous Crustal Accretion" in the "Leg 209 Summary" chapter. The poles to the chrysotile foliation are remarkably clustered, and the data suggest that the mean dip of the veins is to the south-southeast at ~40° with a few conjugate vein sets dipping steeply north-northeast (the reference frame that we used to reorient the data). These are parallel to the orientations shown by the fractures and cataclastic zones within the core. The orientation of the chrysotile veins may reflect the regional (extensional) stress field during serpentinization, consistent with the later formation of cataclastic gouge zones.

Major Fault Zones

The lower one-third of Hole 1274B contains several horizons of serpentine mud and breccia interpreted to be fault gouge over intervals 209-1274A-15R-1, 34–36 cm; 17R-1, 57–59 cm; 18R-2, 6–13 cm; 18R-2, 26–36 cm; 20R-1, 113–121 cm; 22R-1, 58–76 cm; 23R-2, 0–133 cm; 24R-1, 0–74 cm; 24R-1, 107–113 cm; 24R-1, 118–120 cm; 25R-1, 12–25 cm; 25R-1, 40–49 cm; 26R-1, 5–17 cm; and 26R-1, 33–36 cm. Gouge/breccia intervals are partially cohesive and initially had the consistency of stiff clay when recovered from the core barrel. As it dried, the gouge became cohesive and friable. The gouges are dominantly matrix supported, with occasional narrow (<10 cm wide) clast-supported horizons. These horizons contain <10% to >70% clasts. Clasts are mainly subangular to subrounded serpentinized peridotite together with rare metagabbroic rocks and range in size from 0.04 to 5 cm. Clast size is generally finer in matrix-rich horizons and coarser in clast-rich horizons (Fig. F47). The matrix in most intervals is composed of serpentine mud and/or clays; however, some intervals have a carbonate-rich matrix (e.g., intervals 209-1274A-23R-2, 106–120 cm, and 24R-1, 0–8 cm).

Clast-rich and clast-poor gouges appear to have subhorizontal contacts with the surrounding peridotite. Some intervals of gouge have a weak to moderately strong subhorizontal foliation, but a few intervals have a steeply dipping foliation (up to 60°) with undulatory variations (Fig. F48). It is unknown to what degree this foliation was caused or disturbed by drilling.

Downhole Variation and Orientation of Brittle Features

Brittle deformation is generally low in the upper 74 mbsf of Hole 1274A above the major gouge units (Fig. F38) and restricted to several narrow zones of minor fracturing near serpentine veins. Cores 209-1274A-15R and below have high degrees of brittle deformation. Several intervals of gouge recovered from below 74 mbsf are very narrow but may represent wider fault zones with poor recovery. Wide gouge zones (>2 m thick) in Sections 209-1274A-23R-2 and 24R-1 probably represent a major fault zone. It is possible that all of the gouge samples collected from Sections 209-1274A-15R-1 through 26R-1 represent a single major fault system with numerous splays. Brittle shear zones and fractures measured in Hole 1274A generally dip between 20° and 60° to the southeast in the reference frame that we used to reorient the data (Fig. F46), subparallel to the chrysotile veins.

F47. Fault gouge showing variable clast contents and layering, p. 82.

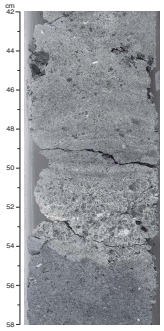

F48. Fault gouge with steeply dipping layering, p. 83.

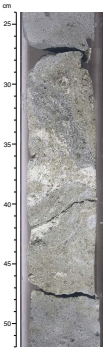

Discussion

The absence of an unequivocally identifiable mantle deformation fabric is somewhat surprising, since models of mantle flow at mid-ocean ridges suggest pervasive deformation at the transition from vertical flow beneath the ridge to horizontal flow away from the ridge. At the hand sample scale in rocks from this hole, identification of high-temperature foliation in peridotite is difficult to separate from the pervasive chrysotile foliation. At the thin section scale, the coarse grain size often prevents identification of high-temperature foliation.

The subtle high-temperature crystal-plastic foliation is a crystal shape fabric resulting from elongation of orthopyroxene grains by slip along (001) and the elongated shape of otherwise undeformed protogranular pyroxene grains. Elongate protogranular pyroxene grains were occasionally parallel to elongate spinels. Elongation was generally observed in smaller interstitial pyroxenes that are texturally distinct from larger (2–7 mm), more abundant equant pyroxene grains.

The serpentine foliation surrounds enclaves of relatively fresh peridotite (Fig. **F44A**). These enclaves, generally 2–5 mm wide and elongate parallel to the serpentine foliation, are easily mistaken for stretched pyroxene porphyroclasts (Ceuleneer and Cannat, 1997). Examination under a binocular microscope and in thin section showed that when a crystal shape fabric was present it was subperpendicular to the serpentine foliation in the cut face of the core and occasionally parallel to elongate spinel trails. In many cases, individual pyroxene grains extend across the fresh peridotite enclaves into highly altered zones. These pyroxenes are pseudomorphed in the altered zones and are fresh in the enclaves.

The serpentine foliation is defined by chrysotile veins and may have formed in the following way. Alteration of olivine to serpentine is accompanied by a significant volume expansion (up to 40%) (O'Hanley, 1996). Olivine is preferentially altered compared to pyroxene, leading to stress concentrations around pyroxene grains. The differential stress is accommodated by dilation cracks that are filled with chrysotile. If pyroxene is relatively sparse and randomly distributed in the rock, a random pattern of veins is produced (Fig. **F44C**). If the pyroxene is strongly clustered or forms bands, the chrysotile veins become concentrated into the more olivine-rich bands aligned parallel to the pyroxene bands (Fig. **F44A**).

To summarize, the peridotites show a very weak high-temperature, low-strain mantle deformation fabric. They were intruded by gabbroic rocks near the base of the thermal boundary layer at high temperatures (probably >600°C). Deformation of the gabbroic rocks may have been coincident with the formation of the mylonite inferred to come from the top of the hole. These deformation events indicate the onset of strain localization at decreasing temperature, which ultimately produced the major fault gouges in the lower part of Hole 1274A. At lower temperatures, concurrent with the faulting, the rocks were partially altered by a succession of serpentinization events. The last recorded event is fracturing and seawater circulation indicated by carbonate veins.

GEOCHEMISTRY

We performed chemical analyses of six harzburgites, three dunites, and two serpentinite mud samples from Site 1274 selected by the ship-

board scientific party, by inductively coupled plasma–atomic emission spectrometry (ICP-AES) for determining major and trace element concentrations, and gas chromatography for H_2O, CO_2, and S. These samples are representative of the rocks recovered from Hole 1274A (see **"Igneous and Mantle Petrology,"** p. 2, and **"Metamorphic Petrology,"** p. 7, for characterization of the lithologic units). The harzburgites and dunites are from the different lithologic units. However, the two mud samples are both from Unit II. The results for the major and trace elements are reported on a volatile-free basis in Table **T5.**

T5. Major and trace element compositions, p. 106.

Peridotites

The Site 1274 peridotites are relatively fresh compared to most other peridotites sampled during Leg 209. This is particularly true for samples from the upper section of the drill core at Site 1274 (Cores 209-1274A-3R to 7R) (see **"Site 1274 Thin Sections"** and **"Metamorphic Petrology,"** p. 7). We note that two samples have the lowest H_2O contents in peridotites from Leg 209 (Sample 209-1274A-3R-1, 87–89 cm, with 11 wt%, and Sample 7R-1, 48–54 cm, with 12 wt%). However, some of the Site 1274 peridotites have H_2O contents of ~15 wt%, indicating that they are highly serpentinized (Fig. **F49**). The mud samples have elevated sulfur contents of 672 and 3268 ppm, compared to both the harzburgites and dunites which are below detection levels (<350 ppm). We note that one dunite from Unit II (Sample 209-1274A-20R-1, 141–144 cm) also contains 638 ppm sulfur, which may be related to the large proportion of black veins in this sample (see **"Metamorphic Petrology,"** p. 7). Mud Sample 209-1274A-23R-2, 67–70 cm, also has a high sulfur content (>3200 ppm).

F49. SiO_2 and H_2O vs. MgO for peridotites, p. 84.

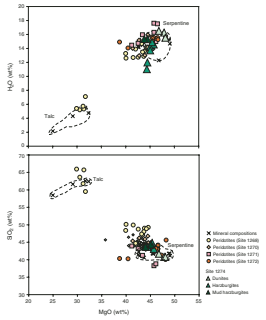

Site 1274 peridotite bulk rock compositions plot in a restricted range of compared to peridotites from previous Leg 209 sites. They are divided into three groups using thin section and visual core descriptions (see **"Igneous and Mantle Petrology,"** p. 2): harzburgites, dunites, and mud. Major elements in the harzburgites are SiO_2 (43–44 wt%), Fe_2O_3 (~8.5 wt%), Al_2O_3 (0.6–0.9 wt%), and MgO (44–46 wt%). In contrast, the dunites have lower SiO_2 (40.8 wt%) and Al_2O_3 (0.16 wt%) and higher Fe_2O_3 (9–10.4 wt%) and MgO (47–48 wt%). Site 1274 peridotites are characterized by high and homogeneous Mg# (100 × molar Mg/[Mg + Fe]) (91.3%–91.6%) except for two samples (Fig. **F50**). Sample 209-1274A-20R-1, 141–144 cm, a dunite in Unit II, is characterized by slightly lower Mg# (90.2%). This sample has a higher Fe_2O_3 content (10.4 wt%) than other Site 1274 peridotites. This variation may result from melt-rock reactions involving Fe-Mg exchange between this peridotite and an olivine-saturated basaltic melt.

F50. FeO vs. MgO whole-rock peridotites, p. 85.

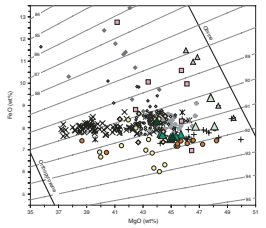

Site 1274 peridotites display lower Al_2O_3 contents than Leg 153 peridotites but are similar to Site 1268, 1270, 1271, and 1272 peridotites. In peridotites, Al_2O_3 is concentrated mainly in pyroxenes, so that variation in Al_2O_3 reflects their degree of fertility. Site 1274 harzburgites contain 0.6–0.9 wt% Al_2O_3, whereas the Site 1274 dunites have lower Al_2O_3 contents (0.3 wt%). These low values suggest that the Site 1274 peridotites were more refractory than Leg 153 peridotites.

F51. CaO vs. Al_2O_3 in peridotites, p. 86.

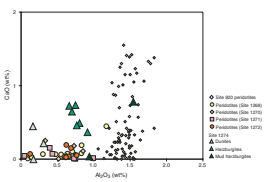

On average, Site 1274 dunites have lower CaO (<0.06–0.45 wt%) contents than Site 1274 harzburgites (CaO = 0.4–0.7 wt%). Site 1274 peridotites have higher CaO contents than other Leg 209 peridotites (Fig. **F51**). The scattering of CaO relative to Al_2O_3 in Site 1274 harzburgites and dunites may by attributed either to the addition of small amounts

of carbonates or to preferential Ca loss during serpentinization. Both Al_2O_3 and CaO are concentrated in pyroxenes and, more particularly, in clinopyroxene for CaO. The lower CaO concentrations observed in peridotites from previous sites has been attributed to either preferential Ca loss during serpentinization and weathering and/or the presence of only minor amounts of clinopyroxene in these rocks. However, the higher CaO content and the rough correlation observed between CaO and Al_2O_3 in Site 1274 peridotites suggests the presence of a larger proportion of clinopyroxene in these rocks. This is consistent with visual core description and petrographic analysis of thin sections indicating the presence of relics of a few percent clinopyroxene (see **"Igneous and Mantle Petrology,"** p. 2).

The two mud samples are similar in major element geochemistry to the harzburgites of Units I and III, apart from Sample 209-1274A-23R-2, 67–70 cm, which contains 0.15 wt% TiO_2 compared to 0.01 wt% TiO_2 in the harzburgite samples. In addition, this mud sample also has slightly elevated Al_2O_3 (1.54 wt%) and Na_2O_3 (0.23 wt%) and a low Mg# (90.5%) compared to the other Site 1274 peridotites. This sample is depleted in MgO when compared with Site 1274 peridotites. Its slightly lower Mg# may result from tectonic mixing of peridotite and gabbroic material, as also suggested by its slightly higher Al_2O_3 and TiO_2 contents.

In terms of trace element geochemistry, the dunites and harzburgites are subtly different (Fig. **F52, F53**). Mud samples plot in the same range as harzburgites, except for Sample 209-1274A-23R-2, 67–70 cm, which displays slightly higher incompatible element contents. The trace elements in dunites are V (14–18.5 ppm), Sc (3–6 ppm), Ni (2500–2700 ppm), and Co (~123 ppm). In contrast, the harzburgites and mud samples are slightly enriched in the incompatible elements V (29–35 ppm) and Sc (7–9 ppm) but lower in Ni (2200–2500 ppm) and Co (107–116 ppm). Ni and Co are preferentially partitioned into olivine, whereas V and Sc are in clinopyroxene. Compatible trace element variations in Site 1274 peridotites mainly reflect the modal proportion of olivine and clinopyroxene. Incompatible trace element concentrations observed in Site 1274 peridotites fall in the range of the peridotites analyzed during Leg 209. Site 1274 peridotites are depleted in TiO_2 (~0.01 wt%), Zr (<2–3.8 ppm), and Sr (<5 ppm) compared to Leg 153 peridotites (Fig. **F53**). These moderately to highly incompatible elements preferentially partition into the liquid during partial melting. Their concentration range suggests that Site 1274 peridotites underwent higher degrees of partial melting compared to Leg 153 peridotites. Variations in TiO_2, Sr, and Zr in Site 1274 peridotites are within analytical error, but V and Sc are positively correlated with CaO and Al_2O_3. V and Sc partition preferentially into clinopyroxene, and their correlation with CaO and Al_2O_3, both proxies for the proportion of pyroxene present, suggests the presence of a small amount of clinopyroxene preserved in these rocks.

F52. Cr, V, and Sc vs. Al_2O_3 in peridotites, p. 87.

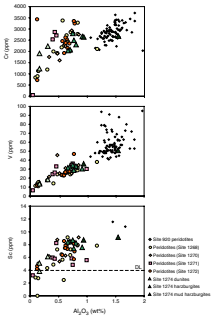

F53. TiO_2 and Zr vs. Al_2O_3 in peridotites, p. 88.

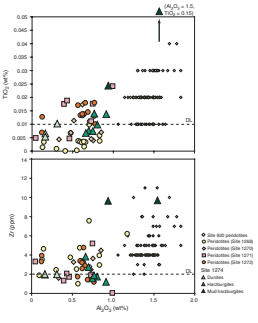

Discussion

Loss on ignition values and volatile contents are high in Site 1274 peridotites (>10 wt%). All these rocks have been modified by alteration, predominantly to serpentine, leading to the addition of significant amounts of volatile constituents including the addition of a S-enriched component in Unit II peridotites. The Unit II mud samples analyzed from Site 1274 are compositionally the same as the peridotites from the

same site, except for a slight enrichment in TiO_2 and Al_2O_3 in one sample that can be attributed to alteration or mechanical mixing of peridotite and gabbroic material in the fault gouge.

Geochemical data on Site 1274 peridotites suggest that prior to alteration these rocks had chemical compositions similar to those of Site 1268, 1270, and 1272 peridotites, apart from higher CaO at Site 1274. In contrast to other Leg 209 peridotites, CaO variations in Site 1274 peridotites are correlated with Sc variations. Both elements are preferentially partitioned into clinopyroxene in peridotites. It should be noted that a few percent clinopyroxenes were observed in Site 1274 samples. This suggests that the apparent CaO enrichment of Site 1274 peridotites is due, in part, to the presence of less altered clinopyroxenes in these rocks compared to peridotites at Sites 1268, 1270, and 1272. At the other sites, CaO may have been mobile in peridotites during alteration. For additional discussion of CaO variation in these peridotites, particularly the possibility of $CaCO_3$ metasomatism, please see Figures **F45,** p. 124, and **F46,** p. 125, with accompanying text, in the "Leg 209 Summary" chapter.

Site 1274 is the first site drilled during Leg 209 that recovered peridotite from north of the 15°20′N Fracture Zone. Previous geochemical studies on dredge samples from the Mid-Atlantic Ridge between 14° and 16°N revealed that the mantle source of basalts south of the 15°20′N Fracture Zone is geochemically "enriched" and similar to the source of hotspot-related mid-ocean-ridge basalt as observed elsewhere along the Mid-Atlantic Ridge (fig. F3 in Kelemen et al., 2002). This may be related to the fact that mantle peridotites seem to have undergone unusually high degrees of melting. North of the fracture zone, however, basalts and peridotites have compositions typical for the Mid-Atlantic Ridge away from hotspots (Fig. **F4,** p. 81, in the "Leg 209 Summary" chapter). Our initial geochemical results on Site 1274 peridotites are not consistent with these other data. Instead, in their major and moderately incompatible element contents, Site 1274 peridotites are similar to the peridotites sampled south of the fracture zone during this leg. All Leg 209 peridotites were more refractory than Leg 153 peridotites.

The average composition of Leg 209 peridotites plots at the most depleted end of the mantle fractionation array on a MgO/SiO_2 vs. Al_2O_3/SiO_2 diagram (Fig. **F54**). Leg 209 peridotites display low Al_2O_3/SiO_2 (<0.01–0.03), similar to those of the most refractory peridotites such as the Izu-Bonin Mariana forearc peridotites (Parkinson and Pearce, 1998), the fast-spreading East Pacific Rise peridotites (Niu and Hekinian, 1997), and the Oman peridotites (Godard et al., 2000). A trend toward low MgO/SiO_2 values observed in Site 1268 peridotites as well as in some samples from the other sites drilled during Leg 209 is due to MgO loss and/or SiO_2 addition during hydrothermal alteration and weathering. The high MgO/SiO_2 ratio in some Leg 209 peridotites mainly reflects the variations of the orthopyroxene/olivine modal ratio, from harzburgites to the dunites. When samples that are most affected by alteration are excluded (Site 1268 and 1270 peridotites), Leg 209 peridotite compositions are consistent with an evolutionary trend parallel to the "mantle array," similar to that shown by Southwest Indian Ocean Ridge and Western Alps peridotites. Leg 209 peridotites represent the most refractory peridotites yet sampled at a slow-spreading ridge.

F54. MgO/SiO_2 vs. Al_2O_3/SiO_2 for peridotites, p. 89.

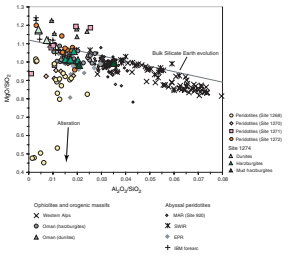

PHYSICAL PROPERTIES

The physical properties of the peridotites cored in Hole 1274A were characterized through a series of measurements on whole-core sections, split-core pieces, and discrete samples as described in "Physical Properties," p. 18, in the "Explanatory Notes" chapter. We measured natural gamma ray (NGR) activity and magnetic susceptibility on the multisensor track (MST) system, thermal conductivity, compressional wave velocity, density, and porosity. The rock names reported in data tables correspond to the primary lithologies determined by the igneous core description group. The data are summarized, as a function of depth, in Figure F55.

Natural Gamma Radiation

All cores recovered during Leg 209 were measured using the NGR logger on the MST at 10-cm intervals with a time period of 30 s. Results are output in counts per second and shown in Figure F56. The cores from Hole 1274A display natural radioactivity in the same range as the background radiation in the core laboratory on board the *JOIDES Resolution*.

Magnetic Susceptibility

Magnetic susceptibility values were acquired on the MST at 2.5-cm intervals for all recovered cores, except Core 209-1274A-28R. The variation of magnetic susceptibility with depth in Hole 1274A is shown in Figure F56. Magnetic susceptibility is comparatively low at the top of the hole and increases gradually to a maximum near 0.1 SI in Core 209-1274A-20R (~103 mbsf). Magnetic susceptibility then decreases to the bottom of the hole (Core 209-1274A-27R; Core 28R was not measured with the MST). This trend is correlated with the observed increase of alteration downhole toward a fault zone at ~100–130 mbsf (Fig. F30). Therefore, it is probably related to a gradual increase of the abundance of magnetite in the upper 100 m of Hole 1274A followed by diminishing magnetite content below 130 mbsf.

Thermal Conductivity

Measurements of thermal conductivity in peridotite samples from Hole 1274A were made at irregularly spaced intervals. The data are summarized in Table T6. The thermal conductivities of the peridotite samples range 2.1–3.0 W/(m·K) (mean = 2.51 W/[m·K]). These values are similar to the thermal conductivities of peridotites from Sites 895 and 920 at Hess Deep (Gillis, Mével, Allan, et al., 1993) and the Kane Fracture Zone (Cannat, Karson, Miller, et al., 1995), respectively. They are also similar to the values measured at Sites 1269 through 1272 (Fig. F57).

As described in "Thermal Conductivity," p. 19, in "Physical Properties" in the "Explanatory Notes" chapter, measurements were taken in three directions on the cut face of the archive sample half, whenever possible. The purpose of these measurements was to determine the degree of apparent anisotropy. The apparent thermal conductivity anisotropy of the peridotites measured in cores from Site 1274 ranges 0.8%–8.6% (Fig. F55; Table T6). Apparent thermal conductivity anisotropies measured since the beginning of Leg 209 (including Sites 1268, 1270,

F55. Physical properties in peridotites, p. 90.

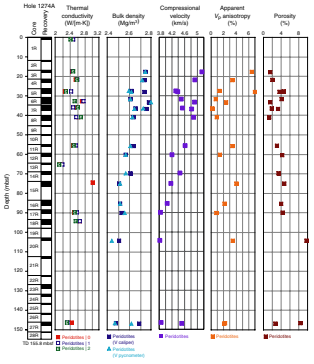

F56. MST magnetic susceptibility and NGR, p. 91.

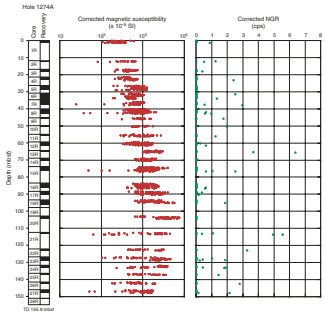

T6. Thermal conductivity measurements, p. 107.

F57. Thermal conductivity of peridotites, p. 92.

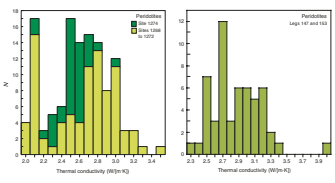

1271, 1272, and 1274) are compiled in Figure F58. The apparent thermal conductivity anisotropy ranges 0.1%–12.6% (mean = 4.23%) in gabbros, diabases, basalts, and peridotites.

Many of the core pieces in which we measured thermal conductivity were also sampled for measurements of porosity, density, velocity, and magnetic susceptibility. In Figure F59, mean values of thermal conductivity are plotted vs. bulk density for all Leg 209 sites through 1274, together with reference single crystal and monomineralic rock data (Clark, 1966; Clauser and Huenges, 1995). As expected from their high degree of alteration, the conductivities of the Leg 209 peridotites and troctolites are close to those of serpentine and talc. Gabbro and diabase values are similar to values reported for anorthite and anorthosite.

Porosity, Density, and Seismic Velocity

Bulk density, grain density, and porosity were measured on small sample chips (~3–6 cm^3) from Hole 1274A. *P*-wave velocity and wet bulk density were measured in cube samples, as described in "*P*-Wave Velocity," p. 20, and "Porosity and Density," p. 20, in "Physical Properties" in the "Explanatory Notes" chapter. These data are summarized in Table T7.

The density and velocity data are compared with data from Legs 147 and 153, as well as Sites 1268, 1270, 1271, and 1272 (see "Physical Properties" in the site chapters for Sites 1268, 1270, 1271, and 1272) in Figure F60. Apparent compressional wave velocity anisotropy in the serpentinized peridotite samples from Site 1274, which ranges 0.2%–7.0%, is comparable to the anisotropy in samples from Sites 1268, 1270, 1271, and 1272.

Bulk densities in the peridotites from Hole 1274A range 2.48–2.78 Mg/m^3, whereas the average *P*-wave velocities range 3.82–5.14 km/s. The lowest velocities and densities in the peridotite samples from Site 1274 overlap the highest densities and velocities from Sites 1268, 1270, 1271, and 1272 and are comparable to the densities and velocities of peridotite samples from Hole 920B from Leg 153 (Cannat, Karson, Miller, et al., 1995) (Fig. F60). An interesting feature of the data from Hole 1274A is that *P*-wave velocities and densities tend to decrease downhole while the bulk porosity increases, as shown in Figure F55. Between the top of the hole and 90 mbsf (Core 209-1274A-17R), densities decrease from >2.70 to ~2.5 Mg/m^3, velocities decrease from 5 to <4 km/s, and porosities increase from ~2% to slightly more than 4%. These trends, together with the gradual increase of magnetic susceptibility with depth (Fig. F55), are consistent with the observed downhole increase in the intensity of alteration in the upper 100 m of Hole 1274A (Fig. F30) (see "Metamorphic Petrology," p. 7).

PALEOMAGNETISM

Hole 1274A penetrated 155.8 m of peridotite and dunite and crossed a fault zone at ~110 mbsf. The mean recovery was 22.2%, with the highest recovery (>50%) between Cores 209-1274A-5R and 7R. Remanence measurements were made on a total of 135 archive-half pieces (35 of these were >20 cm in length) and 18 discrete samples. Both types of data reveal stable positive inclinations that are presumably of normal polarity, although the mean inclination (13°) is significantly shallower than the expected dipole inclination at the site (28°).

F58. Thermal conductivity anisotropy in peridotites, p. 93.

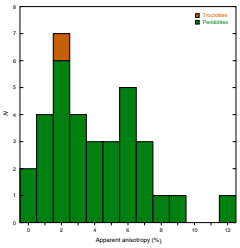

F59. Thermal conductivity vs. bulk density, p. 94.

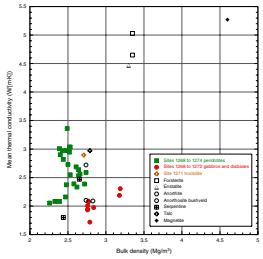

T7. Porosity, density, and velocity from cube and chip samples, p. 108.

F60. *P*-wave velocity vs. wet bulk density, p. 95.

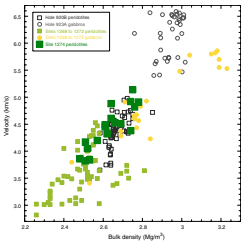

Continuous Measurements

The relatively high recovery from Hole 1274A allows recognition of some depth trends in the magnetic properties (Fig. F61). The natural remanent magnetization (NRM) intensity increases from ~0.5 A/m in the uppermost cores to ~5 A/m in the lower half of lithologic Unit I (see "Igneous and Mantle Petrology," p. 2). NRM intensities of a few amps per meter also characterize the peridotites of lithologic Unit III, whereas the poorly consolidated fault gouge of Unit II (Cores 209-1274A-23R and 24R) have lower intensities. These general trends in NRM intensity are paralleled by variations in the magnetic susceptibility.

The archive halves from Hole 1274A were subjected to stepwise alternating-field (AF) demagnetization, typically to a peak field of 50 mT. Most intervals have a low-stability magnetization component with a steep inclination that is presumably acquired during the drilling/coring process (Fig. F62A, F62B). The relative importance of this low-stability overprint, however, is quite variable, and some intervals exhibit nearly univectorial demagnetization trajectories (Fig. F62C). Demagnetization at peak fields of 20–30 mT is generally sufficient to remove the low-stability overprint and to isolate a characteristic remanence (ChRM) with shallow positive inclinations.

The stability of the remanence, as measured by the ratio of the remanence remaining after 20-mT demagnetization to the original NRM (J_{20mT}/J_{NRM}), generally decreases downhole (Fig. F61). Particularly low stabilities and unstable remanence directions characterize the lower portion of Unit II. The downhole trend in magnetic stability is opposite that observed for NRM intensity and magnetic susceptibility, as well as for the degree of alteration (see "Metamorphic Petrology," p. 7). This inverse relationship can be explained by the increasing abundance of low-coercivity, coarse-grained magnetite with depth (as a result of the degree of serpentinization of the peridotite). As a result of its low coercivity, the coarse-grained multidomain magnetite is most susceptible to a drilling-induced magnetization. The steeper initial inclinations and lower overall magnetic stability in the lower portion of lithologic Unit II can plausibly be attributed to the greater abundance of such coarse-grained magnetite.

F61. Archive-half magnetic measurements, p. 96.

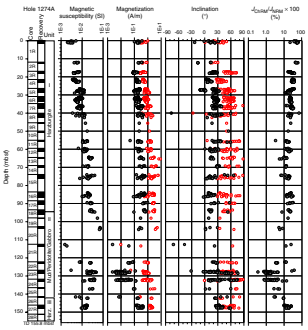

F62. Vector endpoint diagrams, p. 97.

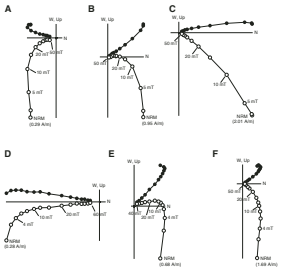

Discrete Samples

Remanence Data

A total of 18 discrete 9.2-cm³ cubic samples of peridotite (15) and dunite (3) were analyzed from Hole 1274A (Table T8). These samples were stepwise demagnetized up to peak fields of 40–60 mT using the D-Tech off-line degausser. At each step, samples were measured in the magnetometer in three orthogonal positions, so that tray positioning and superconducting quantum interference device (SQUID) calibration errors could be averaged at each step. In order to correct for direct-current residual fields in the demagnetizer, double AF demagnetization was applied for peak fields >20 mT (see "Paleomagnetism," p. 22, in the "Explanatory Notes" chapter).

As observed from the archive-half data, the discrete samples from Hole 1274A exhibit a variable low-stability overprint that may be attributed to drilling (Fig. F62D, F62E, F62F). But, as noted for previous sites from Leg 209 (e.g., see "Paleomagnetism," p. 41, in the "Site 1270" chapter), the ChRM is more easily isolated in the discrete samples than

T8. Discrete sample data, p. 109.

in the archive-half data. The characteristic component in discrete samples was normally isolated at low AF fields (8–15 mT), after which the remanence decays univectorially to the origin. The median destructive field (MDF, the alternating field required to reduce the vector difference sum to 50% of its original value) ranges 3–13 mT, and the ChRM represents as much as 25%–50% of the NRM. The fraction of NRM represented by the ChRM is significantly higher than the average fraction in other peridotites recovered from Sites 1268 through 1272.

Magnetic Fabrics

The anisotropy of magnetic susceptibility (AMS) and the anisotropy of anhysteretic remanence (AARM) (McCabe et al., 1985) were determined for all discrete samples from Hole 1274A (Tables **T9, T10**). The AMS tensor was determined using a Kappabridge KLY-2 (Geofyzika Brno) and the standard 15-position measuring scheme. To determine the AARM tensor, the sample was given an ARM (60-mT AF; 0.1-mT bias field) along the six sample axial directions (i.e., +x, +y, +z and –x, –y, –z). After subtraction of a baseline demagnetization step for each ARM acquisition direction, the remanence anisotropy tensor was then calculated in a manner analogous to that used for the susceptibility tensor. These two measures of anisotropy provide complementary information on the preferred orientation/distribution of ferromagnetic minerals in the peridotites. AMS is primarily sensitive to the coarsest-grained magnetite particles, whereas smaller remanence-carrying grains dominate the AARM fabric. In serpentinized peridotites, AMS fabrics have most commonly been found to reflect the distribution of magnetite in serpentine veins (e.g., Lawrence et al., 2002; MacDonald and Ellwood, 1988).

Peridotite samples from Hole 1274A exhibit moderate degrees of susceptibility anisotropy and dominantly oblate AMS fabrics (Fig. **F63**). The degree of anisotropy (P = maximum/minimum eigenvalue) ranges 1.06–1.18. The corresponding remanence anisotropy is more pronounced (P = 1.09–1.46). The higher values in this range are sufficient that some significant deflection of the remanence is possible. The magnitude of this effect will be examined during shore-based studies.

In order to compare the orientations of magnetic fabrics from different samples, some common reference frame is required. Under the assumption that the stable remanent magnetization approximates the time-averaged normal polarity direction (see below), the magnetic fabric data have been restored to a common reference frame by a simple vertical axis rotation that restores the remanent declination to the presumed normal polarity direction (360°). After this reorientation, the maximum eigenvectors of the AMS tensors define a northeast-southwest–trending girdle while the corresponding minimum eigenvectors have shallow northwesterly or southeasterly directions. Thus, the AMS data define a magnetic foliation that is steeply dipping and strikes approximately northeast–southwest. The eigenvectors from the AARM tensors define a similar pattern, suggesting that a broad range of magnetite grain sizes have a common preferred orientation.

Discussion

The direction of the ChRM for both long-core and discrete sample data was estimated by principal component analysis (Kirschvink, 1980), providing orientation information for 135 core pieces (Tables **T8, T11**).

T9. Anisotropy of magnetic susceptibility, p. 110.

T10. Anisotropy of ARM, p. 111.

F63. Discrete sample AMS and AARM, p. 98.

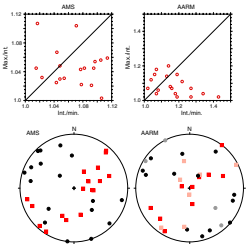

T11. Piece orientations from archive halves, p. 112.

A single discrete sample has a steep negative inclination (–52°). This inclination most likely reflects an orientation error during sampling/curation (in addition, the piece is rounded on all sides and thus the vertical orientation is suspect).

Both the archive-half and discrete samples from Hole 1274A have inclinations that are significantly shallower than the expected dipole inclination at the site (28°) (Fig. F64). The mean inclination calculated from 17 discrete samples is 13.4° (+7.4°/–8.1°, κ = 20.3 using the inclination-only technique of McFadden and Reid, 1982). The characteristic inclinations determined from the archive-half data are more dispersed but most lie between –5° and +35° (Fig. F64), with an average value of 18° (+2°/–3°, *N* = 178). Note that for the longest core pieces (up to 1 m in length), multiple ChRM directions were calculated at ~10-cm intervals. This procedure gives more weight to the data from longer core pieces, an approach validated by the higher scatter evident in directions from pieces <10 cm in length (see below). Given the proximity of the site to the ridge axis and the normal polarity magnetization inferred from inversion of sea-surface magnetic anomaly data (Fujiwara et al., 2003), the shallow positive inclinations most likely represent a normal polarity remanence acquired during the Brunhes Chron (<0.78 Ma) (Cande and Kent, 1995).

The declination of the remanence shows a cluster at ~310° in core coordinates (Fig. F64). This clustering reflects the systematic selection of a splitting plane for the cores, such that the dominant fabric dips toward 090° in the core reference frame. Restoring the mean remanent declination to 360° (the time-averaged normal polarity declination) by a simple vertical axis rotation will result in a southeasterly dip direction for the dominant foliation (see "Structural Geology," p. 12, for a more complete discussion of the orientation of structural features within the core).

Although there is general agreement between the ChRM directions determined from archive halves and discrete samples (Fig. F64), the former exhibit significantly greater scatter. This additional scatter may, at least in part, be attributed to artifacts associated with the measurement of half cores, particularly for small core pieces (see "Appendix," p. 31). If only archive-half data from pieces ≥10 cm are considered, the scatter is significantly reduced (Fig. F65). The combined archive-half and discrete sample data from Hole 1274A reveal no trend with depth in lithologic Unit I. The inclinations for Unit III are much closer to the expected value for the site. Because these two units are separated by fault gouge material, it is possible that some relative motion between the two blocks has occurred. However, given the small number of samples available from below the fault zone, no definitive conclusion can be reached.

F64. Archive-half inclinations and declinations, p. 99.

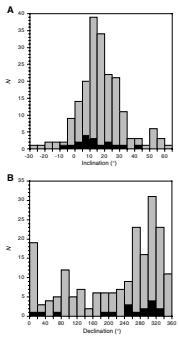

F65. Archive-half ChRM, p. 100.

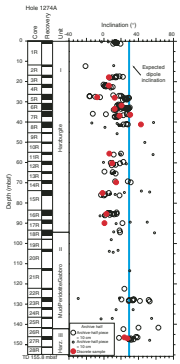

MICROBIOLOGY

Solid Samples

At Site 1274 three rock and two fault gouge intervals were collected to characterize the microbial community inhabiting this environment. The rock samples are variably serpentinized peridotite (Samples 209-1274A-8R-2 [Piece 16, 89–99 cm] [75% alteration], 15R-2 [Piece 7, 54–63 cm] [96% alteration], and 27R-1 [Piece 6, 69–78 cm] [90% alteration]). The lower fault gouge consisted of serpentine, magnetite, and nontron-

ite mud (interval 209-1274A-23R-2, 121–133 cm), whereas the upper fault gouge (interval 23R-2, 71–83 cm) was a serpentine and magnetite mud.

Both the rock and mud samples were prepared as described in "Igneous Rocks," p. 24, in "Microbiology" in the "Explanatory Notes" chapter. Sample 209-1274A-27R-1 (Piece 6) was sealed in a nitrogen-filled container and stored in a 4°C refrigerator for 12 days before it was cultured. Additionally, internal fragments of the fault gouge (~0.5 g each) were inoculated into nutrient broth. These samples were incubated at room temperature and observed daily for signs of microbial growth. Two other fragments of the same size were dissolved in sterile artificial seawater (5 mL each) by shaking the samples for ~5 min. After allowing the clay to settle, 1 mL of each sample was stained with SYBR gold nucleic acid stain and observed for microbial presence via epifluorescent microscopy. No bacteria or viruses were observed in either of the samples.

The type and extent of contamination caused by drill fluids was evaluated as described in "Contamination Tests," p. 26, in "Microbiology" in the "Explanatory Notes" chapter. Samples 209-1274A-8R-2 (Piece 16), 15R-2 (Piece 7), and 27R-1 (Piece 6) were rinsed in nanopure water, and the collected water (50, 41, and 38 mL) was filtered and examined under a fluorescence microscope. For Sample 209-1274A-8R-2 (Piece 16), microsphere concentration was ~340 microspheres/mL of wash. A 0.6-g interior piece of the sample was examined under a fluorescence microscope to detect microsphere penetration, and no microspheres were detected. For Sample 209-1274A-15R-2 (Piece 7), microsphere concentration was >140 microspheres/mL of wash. A 0.15-g piece of the interior of the sample contained no visible microspheres. For Sample 209-1274A-27R-1 (Piece 6), no microspheres were observed in the wash water sample in 20 random fields of view. Only a single microsphere was seen on the entire filter. We cannot determine if the single microsphere represents a very low concentration of microspheres reaching the core or inadvertent contamination during handling. In either case, we consider that the microsphere contamination test on this sample failed. Perfluorocarbon tracer was not used in this hole.

Seawater and Water Samples and Atmospheric Data

One liter of surface water and 1.2 L of bottom water were collected and prepared for deoxyribonucleic acid (DNA) analysis and direct counts as described in "Seawater and Water Samples," p. 26, in "Microbiology" in the "Explanatory Notes" chapter. Results of direct counts of bacteria and viruses from the bottom water were 188.7 bacteria/mL of water and 1132.2 viruses/mL of water. The salinity of this water was 34 psu, which eliminates the possibility that the low counts were due to dilution from nanopure water in the WSTP.

Table T12 is a summary of atmospheric and surface water data for the period of 14–19 June 2003. For surface water direct count data, 1 mL of water was stained as described in "Seawater and Water Samples," p. 26, in "Microbiology" in the "Explanatory Notes" chapter. One milliliter of funnel rinse water was used as a control. Salinity, temperature, and pH values for all surface water values varied; salinity ranged 36.5–37.0 psu, temperature 25.5°–26.1°C, and pH 7.96–7.98. Surface water samples were collected between 1225 and 1354 hr. Air samples were collected for culture-based studies between 0652 and 1845 hr. Air sample

T12. Surface water and atmospheric microbiology data, p. 115.

volumes ranged from 313.2 to 12,040.5 L per sample. Microbial growth (colony forming units) was for the total volume at 48 and >96 hr of incubation (Table T12). Air temperatures, humidity, wind speed, and wind direction ranged 25.6°–26.2°C, 68.1%–79.6%, 3.9–6.3 m/s, and 65°–105°, respectively. Samples for shore-based analysis of bacterial community DNA and bacteria and viral direct counts were collected daily and stored according to protocol.

DOWNHOLE MEASUREMENTS

Temperature Measurements

On 15 June, the WSTP was lowered to an approximate depth of 3931.8 meters below sea level (mbsl), or 8 m above seafloor, for a 38-min station before drilling operations began in Hole 1274A (Fig. F66A). A temperature time series of ocean bottom water and a water sample were obtained for microbiology studies (see "Microbiology," p. 25). The temperature time series shows a gradual increase for ~6.8 min before the water-sampling valve opened, followed by a 2-min period with no sampling of temperature data, one stationary temperature reading, another 2-min interval with no temperature readings while the water-sampling valve was closing, and a 9-min period before the tool began its ascent to the rig floor (Fig. F66B).

The ocean bottom water temperature increased from 3.16° to 3.23°C, or a rate of ~0.0002°C/s over a time interval of 6.8 min before the water-sampling valve was opened (Fig. F66B). These temperatures are consistently higher than the range of 2.91°–3.04°C recorded in Hole 1268A. For comparison, *Shinkai* Dive 6500 Dive 416 traversed this area in 1998 and measured water temperatures of 2.53°C at 3930 mbsl (descending) and 2.52°C at 3927 mbsl (ascending). On the seafloor at 3981 mbsl near Site 1274, the water temperature was measured at 2.515° ± 0.002°C over a period of 13 min during sampling (P. Kelemen, pers. comm., 2003).

A temperature anomaly was recorded after the water-sampling valve closed prior to the tool's ascent. This event is similar to the one recorded above Hole 1268A but is larger in magnitude. The nature of the temperature profile after the water-sampling valve closed and the proximity to the time of tool retrieval profile raises questions about whether this event is an artifact created by electronics of the tool itself or related to warmer fluids emanating from the seafloor.

F66. WSTP temperatures, p. 101.

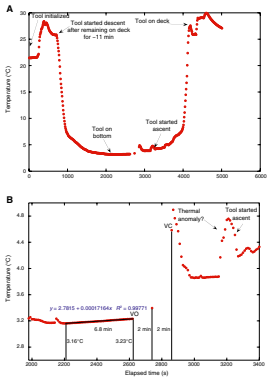

REFERENCES

Agrinier, P., and Cannat, M., 1997. Oxygen-isotope constraints on serpentinization processes in ultramafic rocks from the Mid-Atlantic Ridge (23°N). *In* Karson, J.A., Cannat, M., Miller, D.J., and Elthon, D. (Eds.), *Proc. ODP, Sci. Results,* 153: College Station, TX (Ocean Drilling Program), 381–388.

Agrinier, P., Hékinian, R., Bideau, D., and Javoy, M., 1995. O and H stable isotope compositions of oceanic crust and upper mantle rocks exposed in the Hess Deep near the Galapagos Triple Junction. *Earth Planet. Sci. Lett.,* 136:183–196

Allen, D.E., and Seyfried, W.E., Jr., 2003. Compositional controls on vent fluids from ultramafic-hosted hydrothermal systems at mid-ocean ridges: an experimental study at 400°C, 500 bars. *Geochim. Cosmochim. Acta,* 67:1531–1542.

Bideau, D., Hebert, R., Hekinian, R., and Cannat, M., 1991. Metamorphism of deep-seated rocks from the Garrett ultrafast transform (East Pacific Rise near 13°25'S). *J. Geophys. Res.,* 96:10079–10099.

Bodinier, J.-L., 1988. Geochemistry and petrogenesis of the Lanzo peridotite body, Western Alps., *Tectonophysics,* 149:67–88.

Bonatti, E., Peyve, A., Kepezhinskas, P., Kurentsova, N., Seyler, M., Skolotnev, S., and Udintsev, G., 1992. Upper mantle heterogeneity below the Mid-Atlantic Ridge, 0°–15°N. *J. Geophys. Res.,* 97:4461–4476.

Cande, S.C., and Kent, D.V., 1995. Revised calibration of the geomagnetic polarity timescale for the Late Cretaceous and Cenozoic. *J. Geophys. Res.,* 100:6093–6095.

Cannat, M., Bideau, D., and Bougault, H., 1992. Serpentinized peridotites and gabbros in the Mid-Atlantic Ridge axial valley at 15°37'N and 16°52'N. *Earth Planet. Sci. Lett.,* 109:87–106.

Cannat, M., and Casey, J.F., 1995. An ultramafic lift at the Mid-Atlantic Ridge: successive stages of magmatism in serpentinized peridotites from the 15°N region. *In* Vissers, R.L.M., and Nicolas, A. (Eds.), *Mantle and Lower Crust Exposed in Oceanic Ridges and Ophiolites:* Dordrecht (Kluwer), 5–34.

Cannat, M., Karson, J.A., Miller, D.J., et al., 1995. *Proc. ODP, Init. Repts.,* 153: College Station, TX (Ocean Drilling Program).

Casey, J.F., 1997. Comparison of major- and trace-element geochemistry of abyssal peridotites and mafic plutonic rocks with basalts from the MARK region of the Mid-Atlantic Ridge. *In* Karson, J.A., Cannat, M., Miller, D.J., and Elthon, D. (Eds.), *Proc. ODP, Sci. Results,* 153: College Station, TX (Ocean Drilling Program), 181–241.

Ceuleneer, G., and Cannat, M., 1997. High-temperature ductile deformation of Site 920 peridotites. *In* Karson, J.A., Cannat, M., Miller, D.J., and Elthon, D. (Eds.), *Proc. ODP, Sci. Results,* 153: College Station, TX (Ocean Drilling Program), 23–34.

Clark, S.P., 1966. Thermal conductivity. *In* Clark, S.P. (Ed.), *Handbook of Physical Constants*. Mem.—Geol. Soc. Am., 97:461–482.

Clauser, C., and Huenges, E., 1995. Thermal conductivity of rocks and minerals. *In* Ahrens, T.J. (Ed.), *A Handbook of Physical Constants: Rock Physics and Phase Relations* (Vol. 3), Am. Geophys. Union, Ref. Shelf Ser., 3:105–126.

Deer, W.A., Howie, R.A., and Zussman, J., 1992. *An Introduction to the Rock-Forming Minerals* (2nd ed.): Harlow, United Kingdom (Longman Scientific Technical).

Dick, H.J.B., 1989. Abyssal peridotites, very slow spreading ridges and ocean ridge magmatism. *In* Saunders, A.D., and Norry, M.J. (Eds.), *Magmatism in the Ocean Basins*. Spec. Publ.—Geol. Soc. London, 42:71–105.

Dick, H.J.B., and Kelemen, P.B., 1992. Light rare earth element enriched clinopyroxene in harzburgite from 15°05'N on the Mid-Atlantic Ridge. *Eos, Trans. Am. Geophys. Union,* 73:584.

Dilek, Y., Coulton, A., and Hurst, S.D., 1997. Serpentinization and hydrothermal veining in peridotites at Site 920 in the MARK area. *In* Karson, J.A., Cannat, M., Miller, D.J., and Elthon, D. (Eds.), *Proc. ODP, Sci. Results,* 153: College Station, TX (Ocean Drilling Program), 35–59.

Evans, B.W., 1977. Metamorphism of alpine peridotite and serpentinite. *Annu. Rev. Earth Planet. Sci.,* 5:398–447.

Früh-Green, G.L., Plas, A., and Lécuyer, C., 1996. Petrologic and stable isotope constraints on hydrothermal alteration and serpentinization of the EPR shallow mantle at Hess Deep (Site 895). *In* Mével, C., Gillis, K.M., Allan, J.F., and Meyer, P.S. (Eds.), *Proc. ODP, Sci. Results,* 147: College Station, TX (Ocean Drilling Program), 255–291.

Fujiwara, T., Lin, J., Matsumoto, T., Kelemen, P.B., Tucholke, B.E., and Casey, J., 2003. Crustal evolution of the Mid-Atlantic Ridge near the Fifteen-Twenty Fracture Zone in the last 5 Ma. *Geochem., Geophys., Geosyst.,* 4:10.1029/2002GC000364.

Gillis, K., Mével, C., Allan, J., et al., 1993. *Proc. ODP, Init. Repts.,* 147: College Station, TX (Ocean Drilling Program).

Godard, M., Jousselin, D., and Bodinier, J.-L., 2000. Relationships between geochemistry and structure beneath a paleo-spreading centre: a study of the mantle section in the Oman ophiolite. *Earth Planet. Sci. Lett.,* 180:133–148.

Hebert, R., Adamson, A.C., and Komor, S.C., 1990. Metamorphic petrology of ODP Leg 109, Hole 670A serpentinized peridotites: serpentinization processes at slow spreading ridge environment. *In* Detrick, R., Honnorez, J., Bryan, W.B., and Juteau, T., et al., *Proc. ODP, Sci. Results,* 106/109: College Station, TX (Ocean Drilling Program), 103–115.

Iturrino, G.J., Miller, D.J., and Christensen, N.I., 1996. Velocity behavior of lower crustal and upper mantle rocks from a fast-spreading ridge at Hess Deep. *In* Mével, C., Gillis, K.M., Allan, J.F., and Meyer, P.S. (Eds.), *Proc. ODP, Sci. Results,* 147: College Station, TX (Ocean Drilling Program), 417–440.

Janecky, D.R., and Seyfried, W.E., Jr., 1986. Hydrothermal serpentinization of peridotite within the oceanic crust: experimental investigations of mineralogy and major element chemistry. *Geochim. Cosmochim. Acta,* 50:1357–1378.

Jaroslow, G.E., Hirth, G., and Dick, H.J.B., 1996. Abyssal peridotite mylonites: implications for grain-size sensitive flow and strain localization in the oceanic lithosphere. *Tectonophysics,* 256:17–37.

Kelemen, P.B., Kikawa, E., Miller, D.J., and Baldauf, J., 2002. Leg 209 Scientific Prospectus: Drilling Mantle Peridotite Along the Mid-Atlantic Ridge from 14° to 16°N [Online]. Available from World Wide Web: <www-odp.tamu.edu/publications/prosp/209_prs/209toc.html>. [Cited 2003-07-06]

Kirschvink, J.L., 1980. The least-squares line and plane and the analysis of palaeomagnetic data. *Geophys. J. R. Astron. Soc.,* 62:699–718.

Lawrence, R.M., Gee, J.S., and Karson, J.A., 2002. Magnetic anisotropy of serpentinized peridotites from the MARK area: implications for the orientation of mesoscopic structures and major fault zones. *J. Geophys. Res.,* 107:10.1029/2000JB000007.

MacDonald, W.D., and Ellwood, B.B., 1988. Magnetic fabric of peridotite with intersecting petrofabric surfaces, Tinaquillo, Venezuela. *Phys. Earth Planet. Inter.,* 51:301–312.

McCabe, C., Jackson, M., and Ellwood, B.B., 1985. Magnetic anisotropy in the Trenton Limestone: results of a new technique, anisotropy of anhysteretic susceptibility. *Geophys. Res. Lett.,* 12:333–336.

McFadden, P.L., and Reid, A.B., 1982. Analysis of paleomagnetic inclination data. *Geophys. J. R. Astron. Soc.,* 69:307–319.

Miller, D.J., and Christensen, N.I., 1997. Seismic velocities of lower crustal and upper mantle rocks from the slow-spreading Mid-Atlantic Ridge, south of the Kane Fracture Transform Zone (MARK). *In* Karson, J.A., Cannat, M., Miller, D.J., and Elthon, D. (Eds.), *Proc. ODP, Sci. Results,* 153: College Station, TX (Ocean Drilling Program), 437–454.

Niu, Y., and Hekinian, R., 1997. Basaltic liquids and harzburgitic residues in the Garrett Transform: a case study at fast-spreading ridges. *Earth Planet. Sci. Lett.,* 146:243–258.

Normand, C., Williams-Jones, A.E., Martin, R.F., and Vali, H., 2002. Hydrothermal alteration of olivine in a flow-through autoclave: nucleation and growth of serpentine phases. *Am. Mineral.,* 87:1699–1709.

O'Hanley, D.S., 1996. Serpentinites: records of tectonic and petrological history. *Oxford Monogr. Geol. Geophys.,* Vol. 34.

O'Hanley, D.S., and Wicks, F.J., 1995. Conditions of formation of lizardite, chrysotile and antigorite, Cassiar, British Columbia. *Can. Mineral.,* 33:753–773.

Parker, R.L., and Gee, J.S., 2002. Calibration of the pass-through magnetometer—II. Application. *Geophys. J. Int.,* 150:140–152.

Parkinson, I.J., and Pearce, J.A., 1998. Peridotites from the Izu-Bonin-Mariana forearc (ODP Leg 125); Evidence for partial melting and melt-mantle interactions in a supra-subduction zone setting. *J. Petrol.,* 39:1577–1618.

Rampone, E., Hofmann, A.W., Piccardo, G.B., Vannucci, R., Bottazzi, P., and Ottolini, L., 1996. Trace element and isotope geochemistry of depleted peridotites from an N-MORB type ophiolite (Internal Liguride, N. Italy). *Contrib. Mineral. Petrol.,* 123:61–76.

Sanford, R.F., 1981. Mineralogical and chemical effects of hydration reactions and applications to serpentinization. *Am. Mineral.,* 66:290–297.

Seyler, M., Toplis, M.J., Lorand, J.-P., Luguet, A., and Cannat, M., 2001. Clinopyroxene microtextures reveal incompletely extracted melts in abyssal peridotites. *Geology,* 29:155–158.

Snow, J.E., and Dick, H.J.B., 1995. Pervasive magnesium loss by marine weathering of peridotite. *Geochim. Cosmochim. Acta,* 59:4219–4235.

Sobolev, A.V., Tsamerian, O.P., and Dmitriev, L.V., 1992a. The geochemical anomaly in Mid-Atlantic Ridge basalts between 12°–18°N: geochemical structure and origin. *Proc. 29th Int. Geol. Cong.,* 29:58.

Sobolov, A.V., Tsamerian, G.P., Dmitriev, L.V., and Basilev, B., 1992b. The correlation between the mineralogy of basalt and the associated peridotites: the data from the MAR between 8°–18°N. *Eos, Trans. Am. Geophys. Union,* 73:584.

Toft, P.B., Arkani-Hamed, J., and Haggerty, S.E., 1990. The effects of serpentinization on density and magnetic susceptibility: a petrophysical model. *Phys. Earth Planet. Inter.,* 65:137–157.

Wenner, D.B., and Taylor, H.P., Jr., 1971. Temperatures of serpentinization of ultramafic rocks based on O^{18}/O^{16} fractionation between coexisting serpentine and magnetite. *Contrib. Mineral. Petrol.,* 32:165–185.

Wicks, F.J., and Whittaker, E.J.W., 1977. Serpentine textures and serpentinization. *Can. Mineral.,* 15:459–488.

APPENDIX

In addition to routine half-core measurements, whole-core NRM data were obtained from two sections in Core 209-1274A-6R that had the highest recovery (Sections 6R-2 and 6R-3). The aim of these measurements was to test the influence of the core geometry on both the intensity and directional data obtained from the 2G Enterprises magnetometer (Fig. AF1). The measurement of pieces >50 cm permits easier comparison between the whole-core and archive-half data without the interference of edge effects at piece ends.

To first test homogeneity of the remanence in the core, pieces from Section 209-1274A-6R-3 were measured in two different positions, first with the core +x parallel to the SQUID +x-axis, and then with the core +x parallel to the SQUID +y-axis (Fig. AF1A). The inclination and intensity records from these two runs are essentially identical. After accounting for the ~90° rotation described above, the declinations from these two measurements differ by a consistent offset (≤10°) but have the same pattern. From this agreement in direction and intensity, we conclude that the core pieces can be regarded as homogeneously magnetized.

Having established the homogeneity of the magnetization, we next compared the results obtained for the whole-core and archive-half measurements (Fig. AF1B). The two sets of measurements show differences both in intensity and direction of the remanence. Inclination and intensity appear to be negatively correlated; higher intensities are associated with lower inclinations and vice versa. In addition, the sense of the discrepancy between the two measurements is apparently dependent on the length of piece from which the readings were taken. Archive-half data from shorter pieces (Section 209-1274A-6R-2 [Pieces 2, 3]) yielded higher intensity and lower inclination than whole-core measurements. In contrast, archive-half measurements at the center of a long piece (Section 209-1274A-6R-2 [Piece 1]) showed lower intensities but steeper inclinations than whole-core runs. An unexpected result was that the largest discrepancies (as much as 8° in inclination and several tens of degrees in declination) between whole-core and half-core data in long core pieces were observed in the middle region of the piece.

The fact that the fluctuations in direction correlate with remanence intensity suggests that it is a measurement artifact that affects both the whole-core and the half-core data, but is more accentuated in the latter. It may be caused by a signal from source along the z-axis inducing a signal in the x- and y- SQUID sensors, particularly from off-axis sample regions (Parker and Gee, 2002). The symmetry of the magnetometer helps to cancel some of this cross-talk for whole-core measurements, but the likely centimeter-scale variability in the intensity of the remanence will produce inevitable nonzero average cross-talk. This problem will be even more severe for archive-half measurements, because these measurements lack a mirror symmetry about the y–z plane (x = 0).

AF1. Whole-core vs. archive-half NRM, inclination, and declination, p. 116.

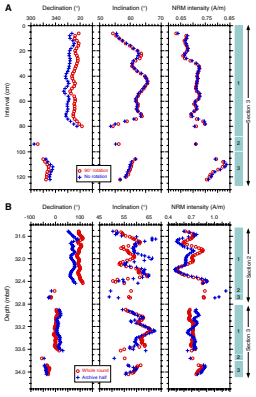

Figure F1. Bathymetric map indicating the subsea camera survey track and location of Hole 1274A. Bathymetric data courtesy of T. Fujiwara and T. Matsumoto of JAMSTEC (Fujiwara et al., 2003).

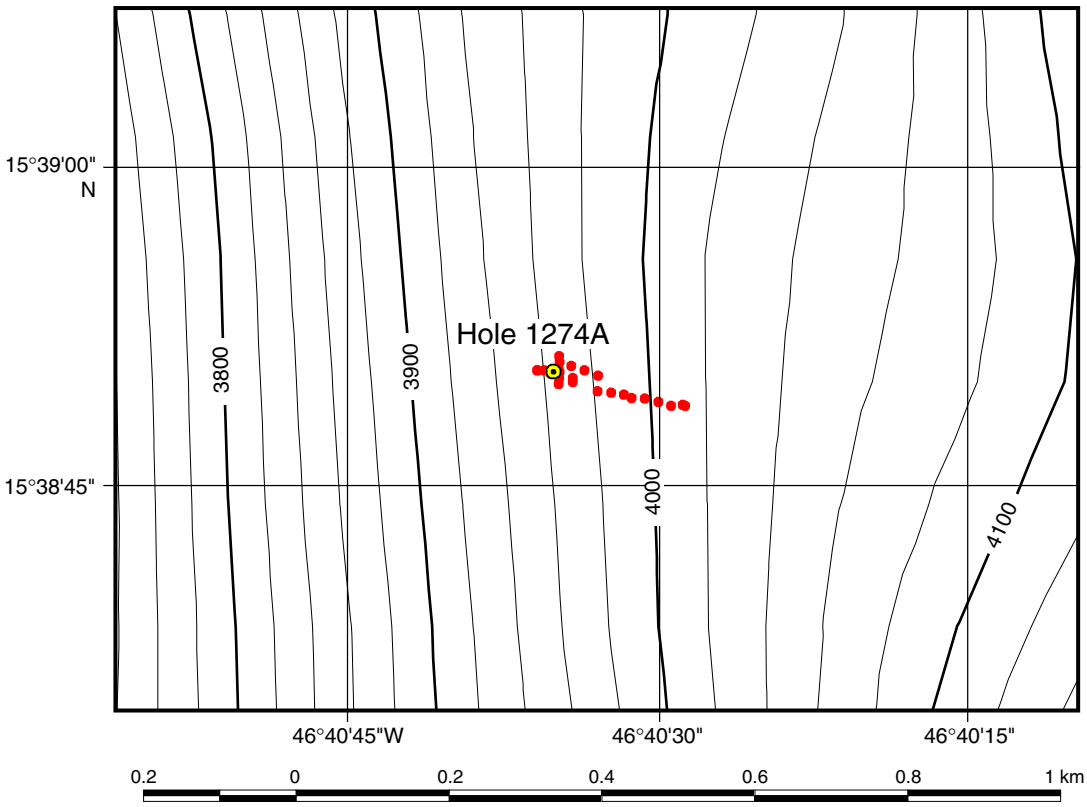

Figure F2. A. Location map with track of *Shinkai* 6500 Dive 416 (red dotted line), locations and lithologies of samples from that dive, and the approximate position of Hole 1274A. (Continued on next page.)

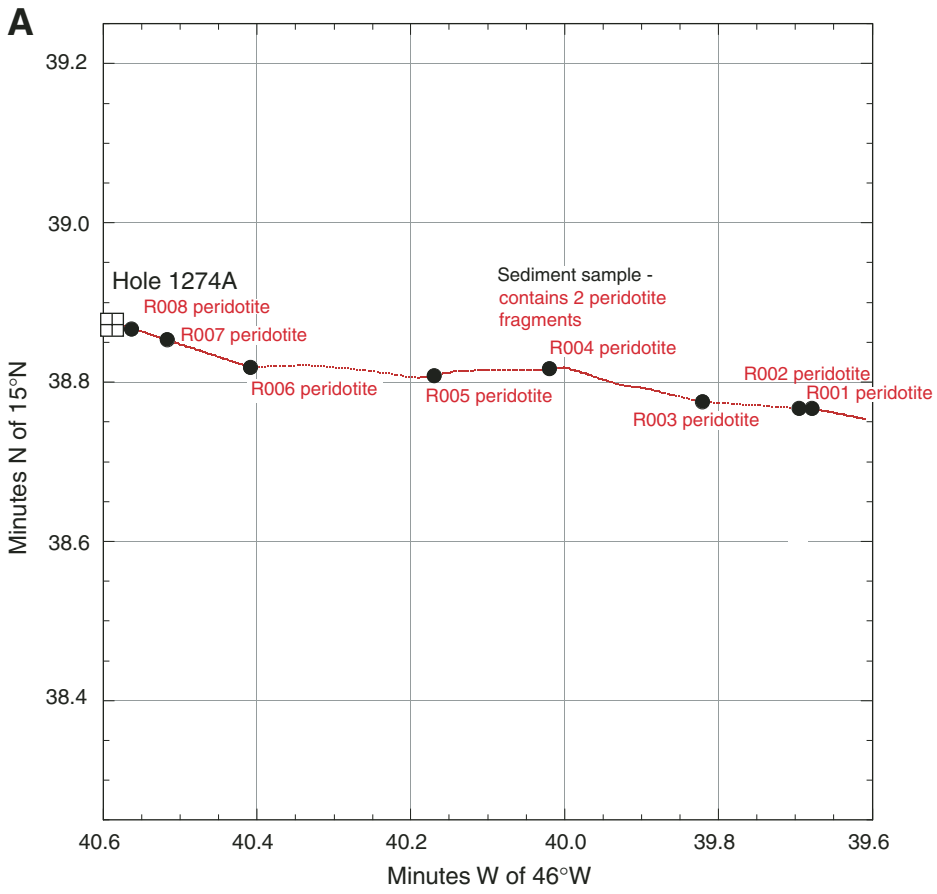

Figure F2 (continued). B. Bathymetric section based on *Shinkai* 6500 Dive 416, projected along 278° with no vertical exaggeration. Locations and lithologies of samples collected during the dive, as well as the approximate position of Hole 1274A, are indicated.

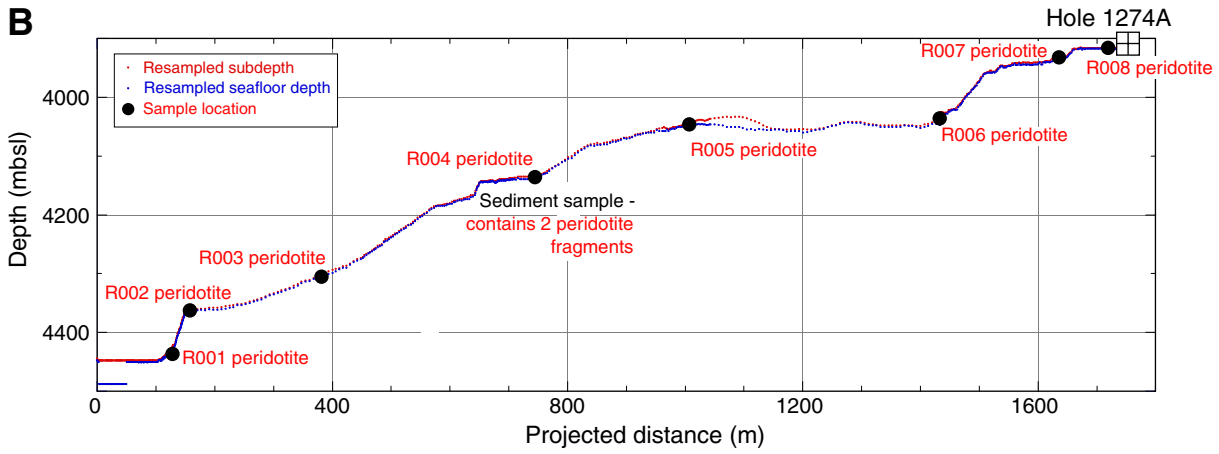

Figure F3. Lithology and stratigraphy of Hole 1274A. TD = total depth.

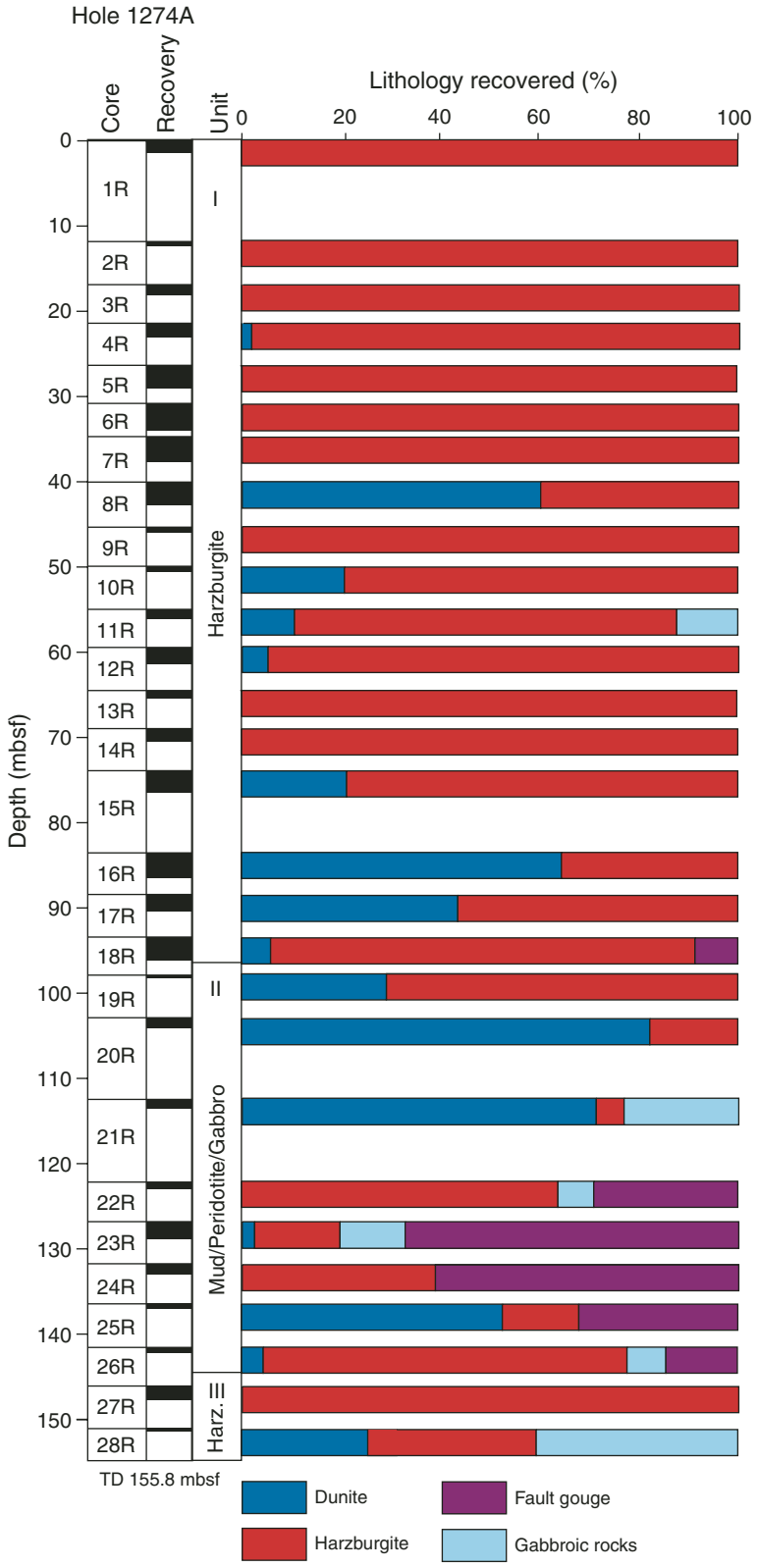

Figure F4. Close-up photograph of typical harzburgite (interval 209-1274A-3R-1, 26–54 cm).

Figure F5. Close-up photograph of the gradational contact from harzburgite to dunite (interval 209-1274A-16R-2, 1–38 cm).

Figure F6. Close-up photograph of pebble of mylonitic harzburgite (interval 209-1274A-2R-1 [Piece 1, 0–4 cm]).

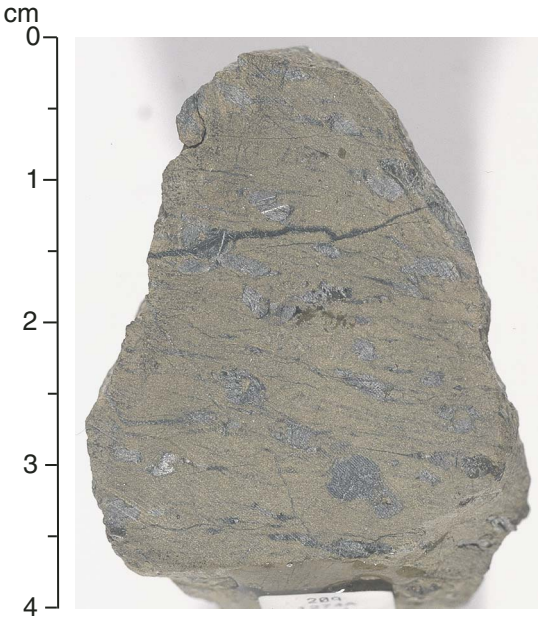

Figure F7. Close-up photograph of mud interval from the fault gouge zone (interval 209-1274A-24R-1, 3–29 cm).

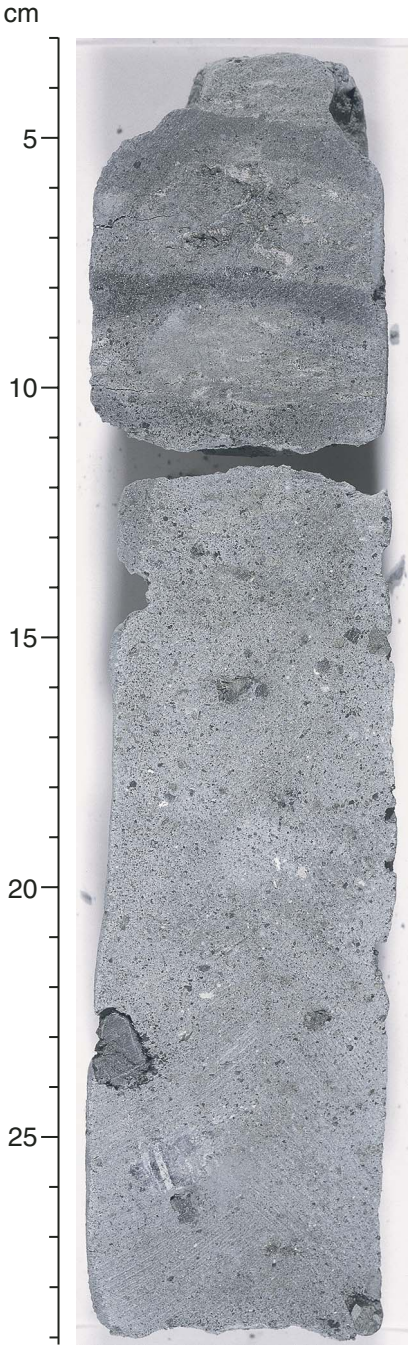

Figure F8. Close-up photograph of altered gabbro (interval 209-1274A-21R-1 [Piece 5, 13–20 cm]).

Figure F9. Modal orthopyroxene percentage downhole, as estimated from visual core description.

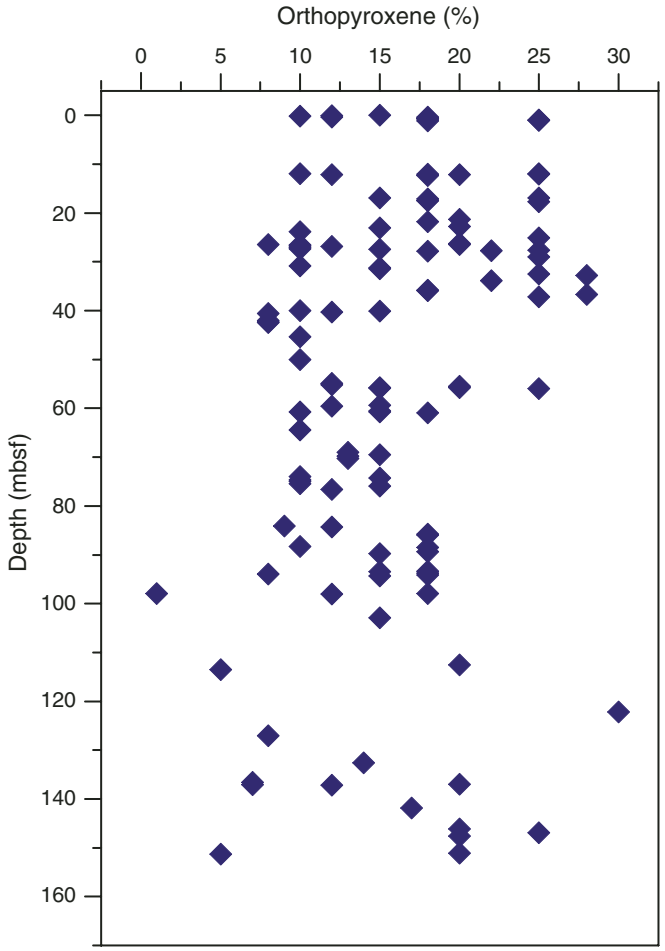

Figure F10. Photomicrographs of orthopyroxene. **A.** Protogranular texture with smoothly curved olivine/orthopyroxene grain boundary (Sample 209-1274A-1R-1, 15–17 cm) (cross-polarized light [XPL]: blue filter; field of view [FOV] = 0.7 mm; image 1274A_008). **B.** Anhedral to interstitial orthopyroxene, partially enclosing medium-sized grains of olivine along its margin (Sample 209-1274A-8R-1, 15–18 cm) (XPL: blue + dark gray filters; FOV = 11 mm; image 1274A_060). **C.** Orthopyroxene at the contact with olivine, showing deep embayment within olivine. A symplectite of spinel and a strongly birefringent mineral (olivine or clinopyroxene) is present along one olivine/orthopyroxene contact (Sample 209-1274A-7R-1, 101–105 cm) (XPL; FOV = 0.7 mm; image 1274A_048).

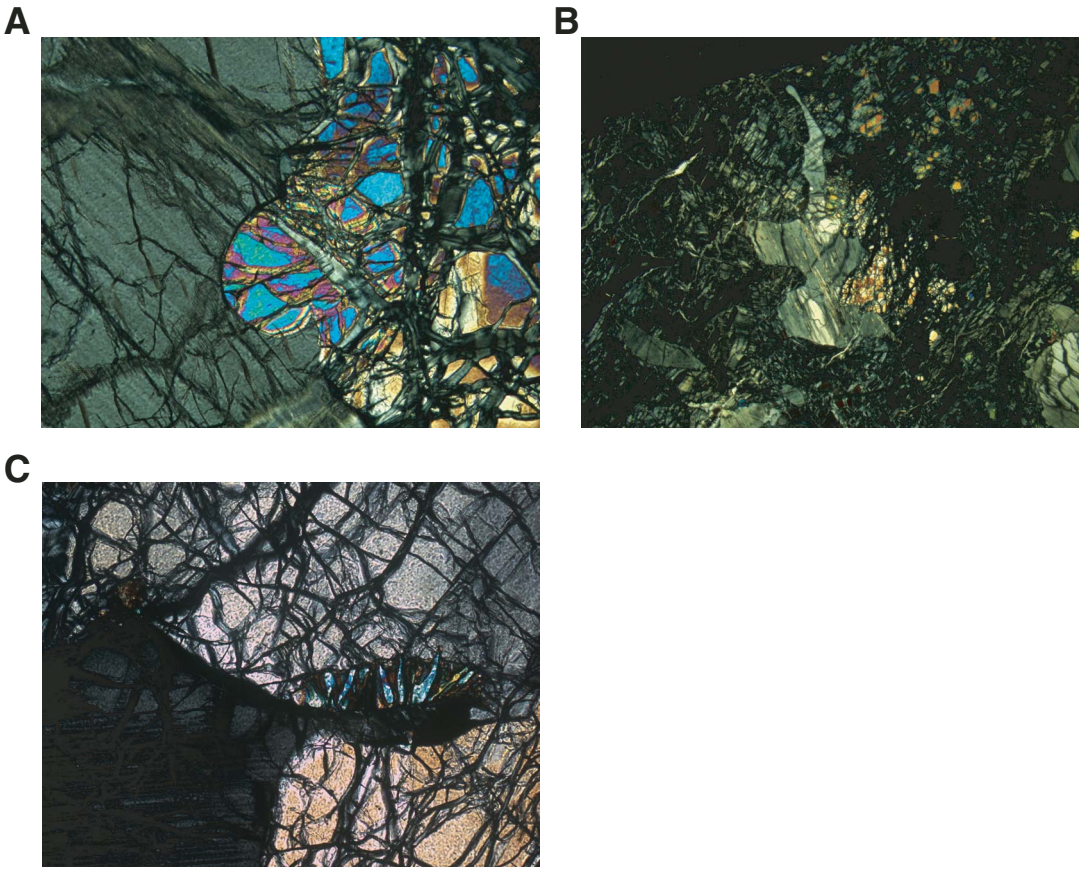

Figure F11. Photomicrographs showing olivine–orthopyroxene protogranular texture with spinel-bearing symplectite along the orthopyroxene margin (Sample 209-1274A-7R-1, 101–105 cm). **A.** Plane-polarized light; field of view (FOV) = 2.75 mm; image 1274A_044. **B.** Cross-polarized light; FOV = 2.75 mm, image 1274A_045. **C.** Close-up showing the mineral assemblage forming the intergrowth spinel, a highly birefringent mineral in the upper part of the image and orthopyroxene (cross-polarized light; FOV = 0.7 mm; image 1274A_046).

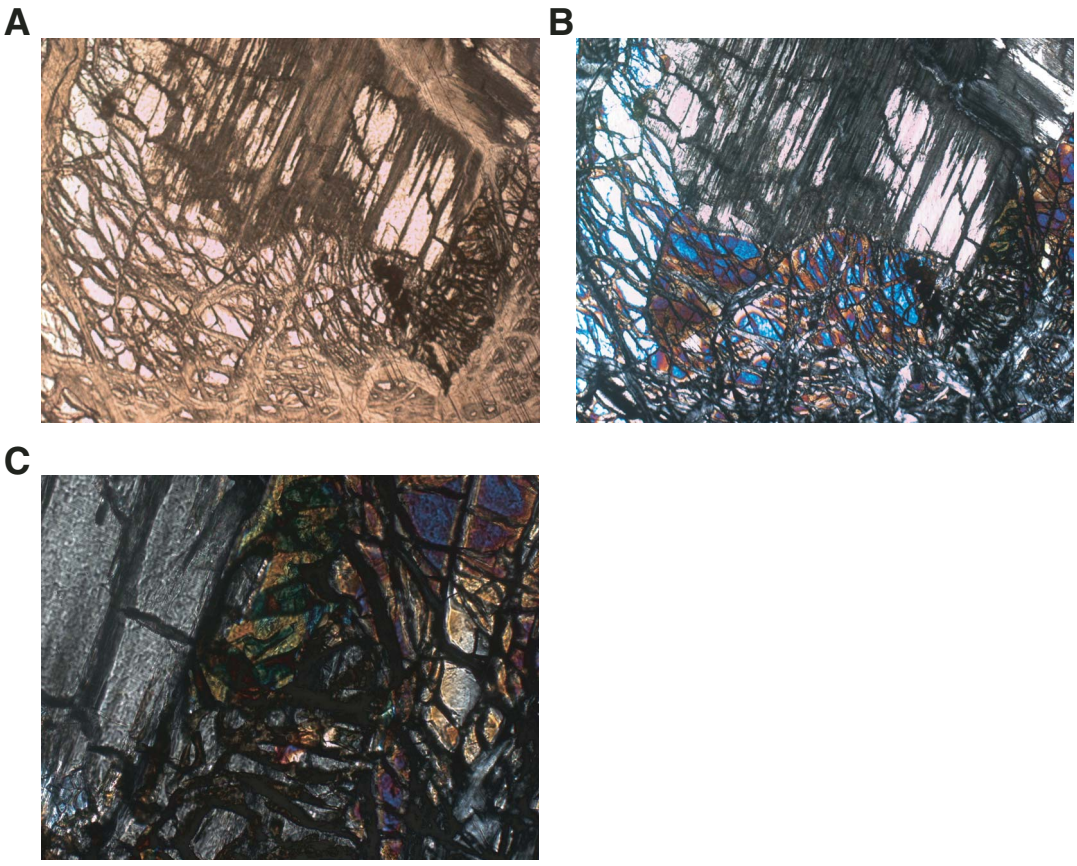

Figure F12. Photomicrographs of clinopyroxene (Sample 209-1274A-8R-1, 15–18 cm). **A.** Clinopyroxene–spinel symplectite at the contact between protogranular orthopyroxene and olivine. The symplectite extends into the olivine (cross-polarized light; field of view = 2.75 mm; image 1274A_049). **B.** Close-up showing that the clinopyroxene is a single crystal with undulatory extinction (cross-polarized light; field of view = 1.4 mm; image 1274A_050).

A

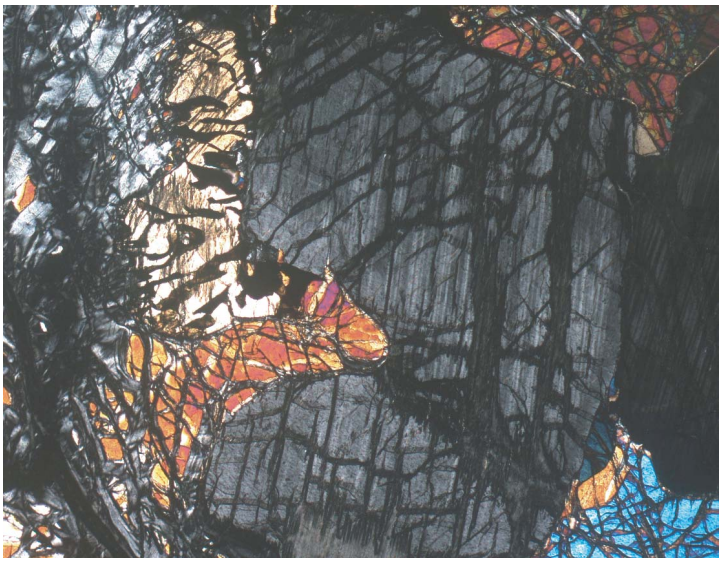

B

Figure F13. Photomicrographs of poikilitic clinopyroxene. **A.** Enclosing small olivine grains at a contact with orthopyroxene (Sample **209-1274A-7R-1, 48–51 cm**) (plane-polarized light; field of view [FOV] = 0.7 mm; image 1274A_043). **B.** Enclosing small recrystallized orthopyroxene grains (Sample **209-1274A-8R-1, 61–64 cm**) (cross-polarized light [XPL]; FOV = 0.7 mm; image 1274A_054). **C.** Enclosing small olivine grains (Sample **209-1274A-1R-1, 15–17 cm**) (XPL: blue filter; FOV = 1.4 mm; image 1274A_006). **D.** Enclosing (replacing or exsolved from?) orthopyroxene (Sample **209-1274A-1R-1, 15–17 cm**) (XPL: blue filter; FOV = 1.4 mm; image 1274A_007).

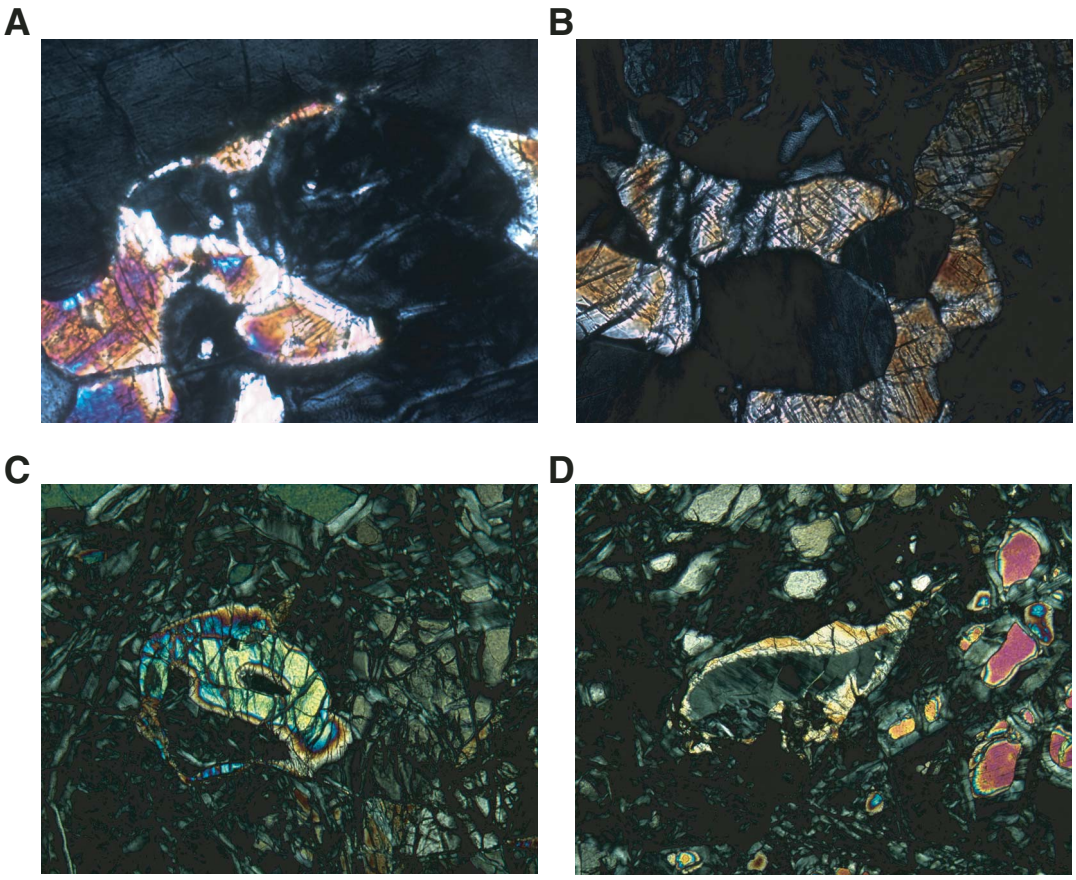

Figure F14. Photomicrograph showing one of the largest clinopyroxene crystals observed in Hole 1274A. Note that the left extremity is interstitial to olivine and recrystallized orthopyroxene (Sample **209-1274A-7R-1, 48–51 cm**) (plane-polarized light; field of view = 2.75 mm; image 1274A_035).

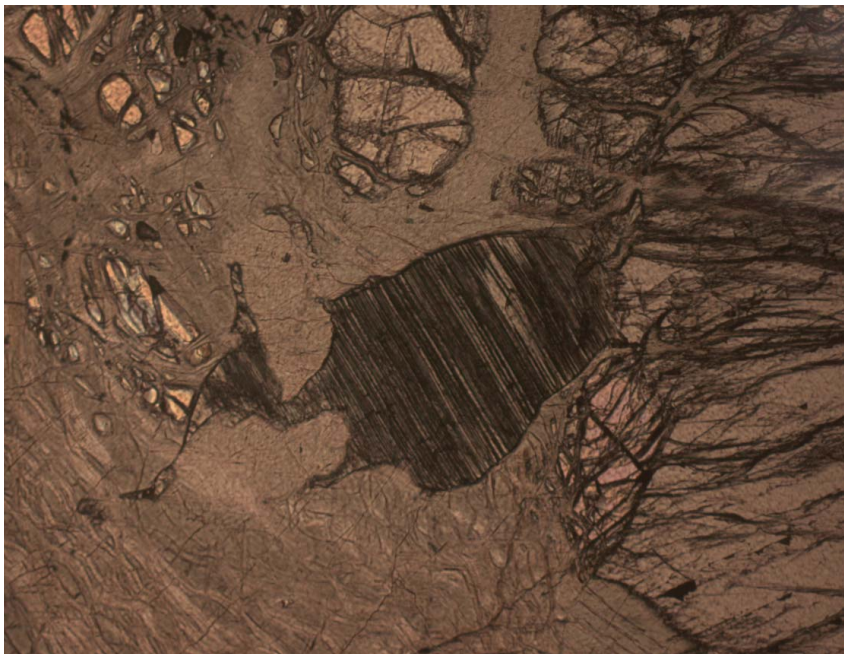

Figure F15. Photomicrographs of orthopyroxene. **A.** Incipient recrystallization of orthopyroxene into subgrains surrounded by clinopyroxene. A large spinel is included in the orthopyroxene porphyroclast. Clinopyroxene lamellae grew within the orthopyroxene subgrain along the contact with this spinel. In the lower right corner, a small grain of olivine is present together with clinopyroxene at the junction between the two orthopyroxenes and a large olivine crystal (Sample **209-1274A-4R-1, 52–54 cm**) (cross-polarized light [XPL]; field of view [FOV] = 1.4 mm; image 1274A_028). **B.** Kinked and partially recrystallized orthopyroxene. Clinopyroxene mantles a subgrain. Lamellae of clinopyroxene grew within the orthopyroxene along the kink (Sample **209-1274A-7R-1, 101–105 cm**) (XPL; FOV = 1.4 mm; image 1274A_047). **C.** Cluster of two orthopyroxenes, with clinopyroxene developed around them. Note that all the clinopyroxene is in optical continuity (Sample **209-1274A-7R-1, 48–51 cm**) (XPL; FOV = 1.4 mm; image 1274A_039). **D.** Close-up of same sample shown in C showing that the orthopyroxenes are divided into subgrains containing interstitial clinopyroxene (XPL; FOV = 0.7 mm; image 1274A_041). (Continued on next page.)

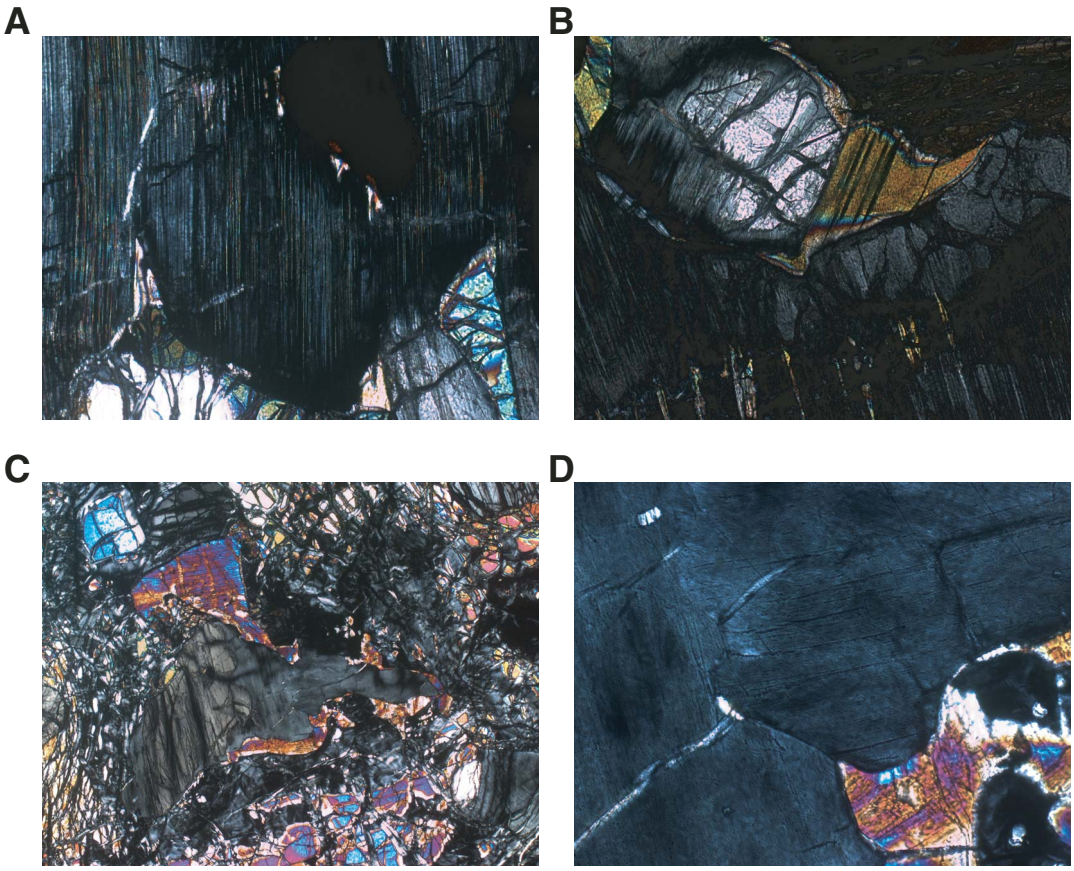

Figure F15 (continued). E, F. Contact between a large spinel and orthopyroxene. Thin lamellae of clinopyroxene grew within orthopyroxene along the contact. Clinopyroxene also surrounds a small orthopyroxene grain to the left; (E) Sample **209-1274A-11R-1, 67–70 cm** (plane-polarized light; FOV = 1.4 mm; image 1274A_057); (F) Sample **209-1274A-11R-1, 67–70 cm** (XPL; FOV = 1.4 mm, image 1274A_058).

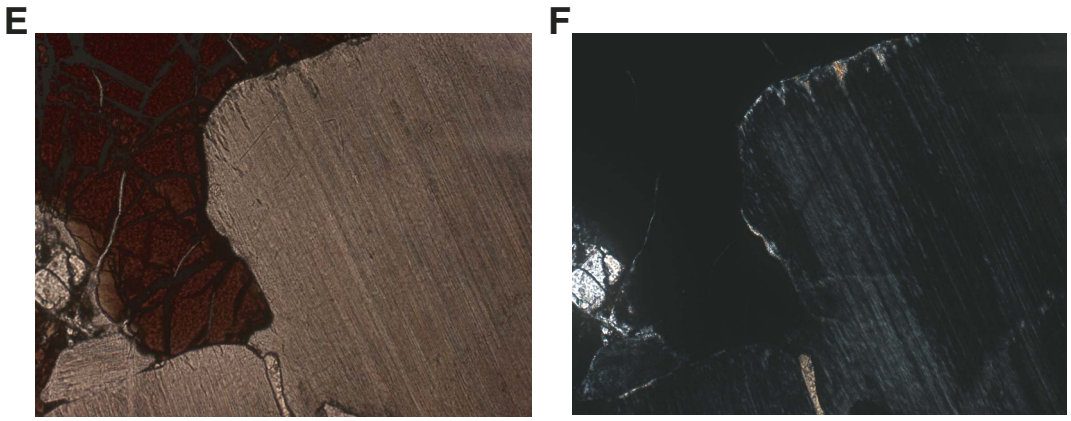

Figure F16. Photomicrographs of orthopyroxene. **A–C.** Orthopyroxene separated into two grains. The orthopyroxene on the left is separated from the orthopyroxene on the right by a microscopic granular assemblage of olivine, clinopyroxene, and spinel (Sample **209-1274A-3R-1, 92–94 cm**) (cross-polarized light [XPL]). (A) Field of view (FOV) = 5.5 mm; image 1274A_025. (B) Close-up showing small grains of olivine and clinopyroxene filling the cracks. A larger clinopyroxene grew at the junction between the two orthopyroxene grains and adjacent olivine (FOV = 1.4 mm; image 1274A_ 026). (C) Close-up, after rotation, of the contact between the two orthopyroxenes in A, showing the fine-grained assemblage of olivine, clinopyroxene, and spinel between them (FOV = 2.75 mm; image 1274A_034). **D.** Incipient subdivision of kinked orthopyroxene, with microfracture filled with small grains of olivine, clinopyroxene, and spinel (Sample **209-1274A-4R-1, 52–54 cm**) (XPL; FOV = 5.5 mm; image 1274A_029).

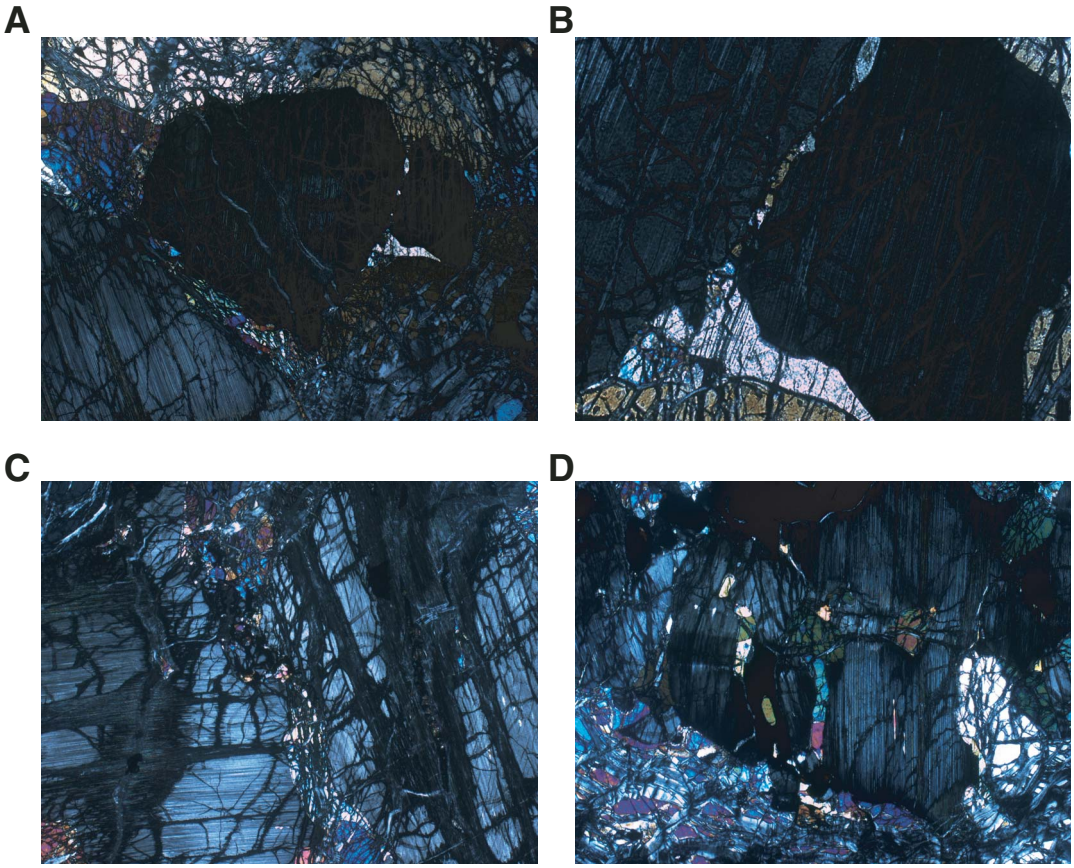

Figure F17. Photomicrographs of clinopyroxene (Sample 209-1274A-4R-1, 52–54 cm) (cross-polarized light). **A.** Euhedral clinopyroxene associated with spinel within orthopyroxene along a contact with olivine (field of view = 0.7 mm; image 1274A_032). **B.** Close-up showing igneous twinning in the clinopyroxene (field of view = 0.35 mm; image 1274A_030).

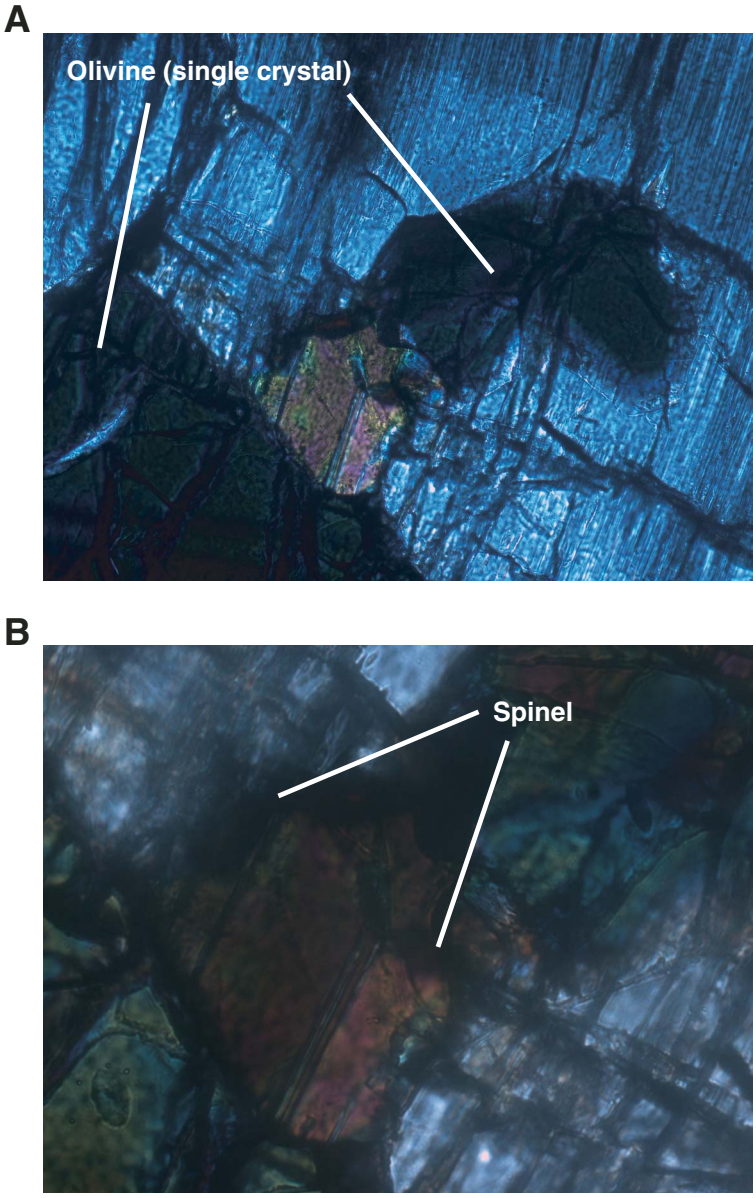

Figure F18. Distribution of orthopyroxene and clinopyroxene grain sizes in peridotites from Hole 1274A, estimated from visual core descriptions and thin sections.

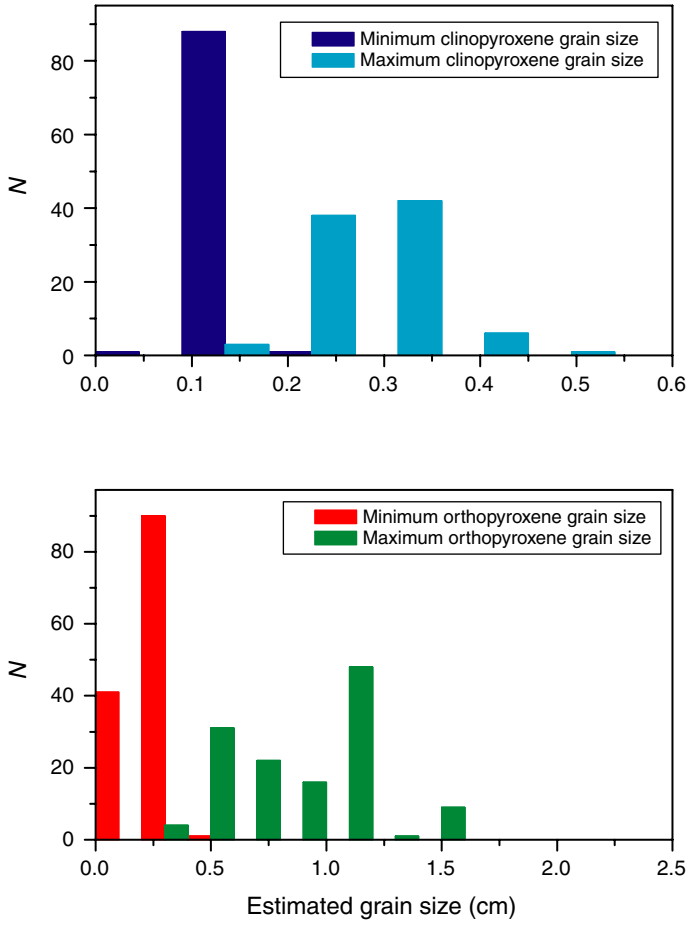

Figure F19. Variation of observed spinel shape from visual core description and thin sections in dunite and harzburgite from Hole 1274A. V = vermicular, I = interstitial, E = equant. V + I = both vermicular and interstitial spinel occurs in the same interval. For comparison, the lithologic variation in Hole 1274A is shown in the right panel.

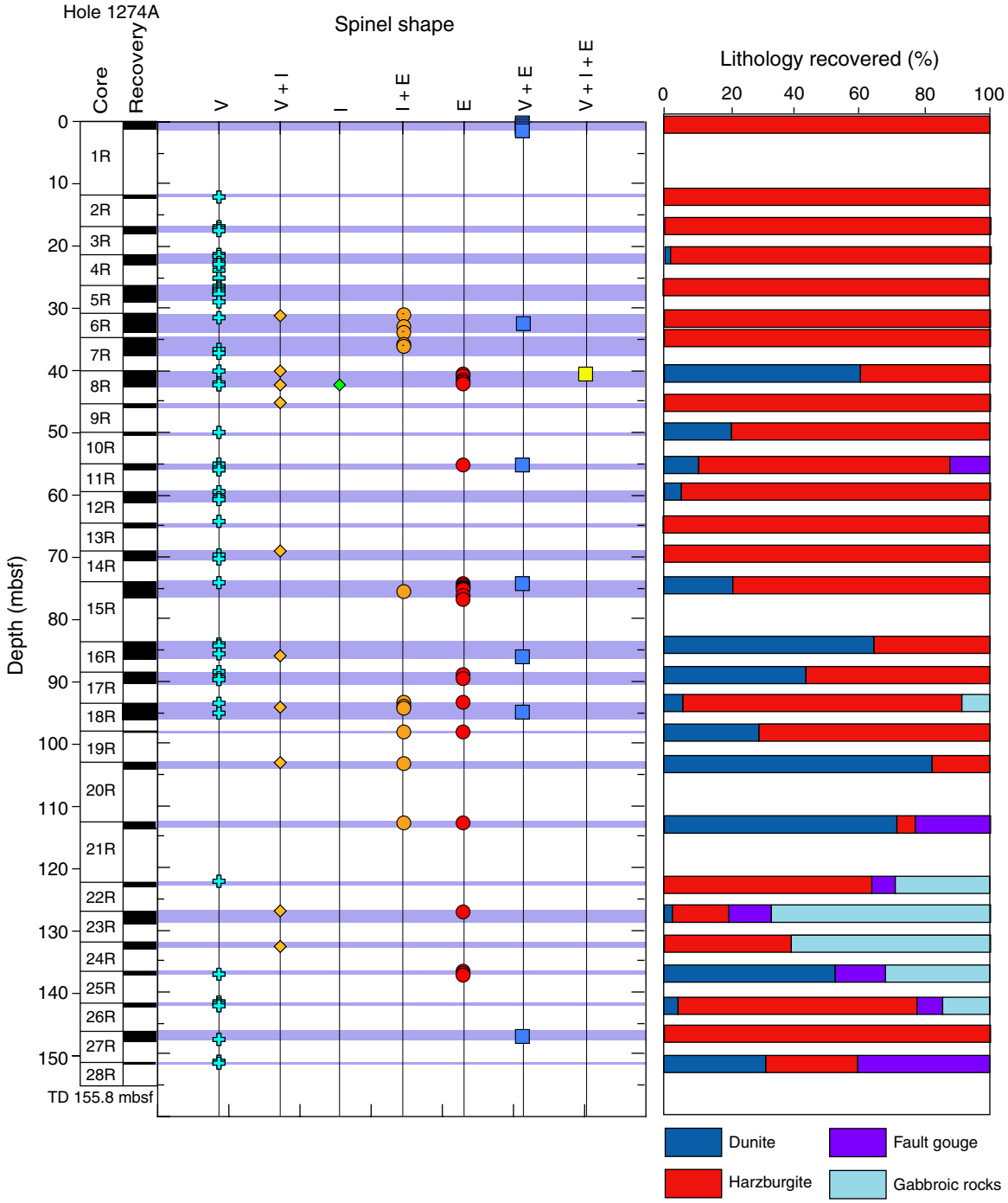

Figure F20. Distribution of observed spinel shape from visual core description and thin sections in dunite and harzburgite from Hole 1274A.

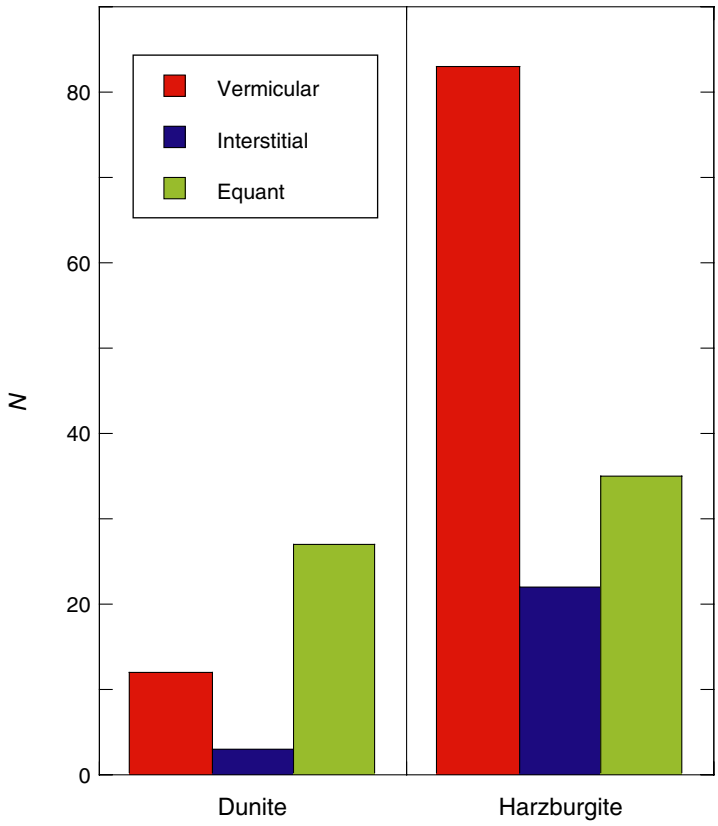

Figure F21. Variation in spinel texture in harzburgite and dunite. Proportions of the spinel texture for each lithology are normalized to 100%. Axes scales are in percent.

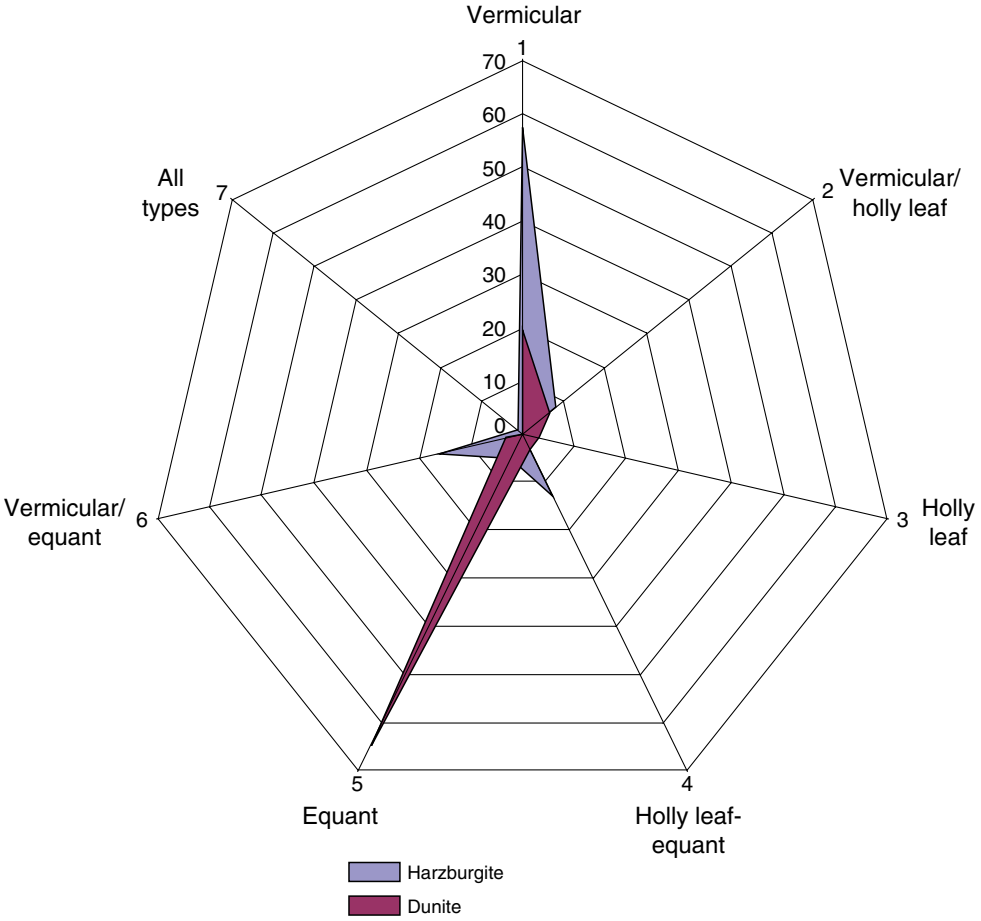

Figure F22. Photomicrographs of elongate, interstitial clinopyroxene and spinel–clinopyroxene symplectite (upper left) in dunite (Sample 209-1274A-8R-1, 109–111 cm) (field of view = 2.75 mm). **A.** Plane-polarized light: blue filter; image 1274A_013. **B.** Cross-polarized light: blue filter; image 1274A_012.

A

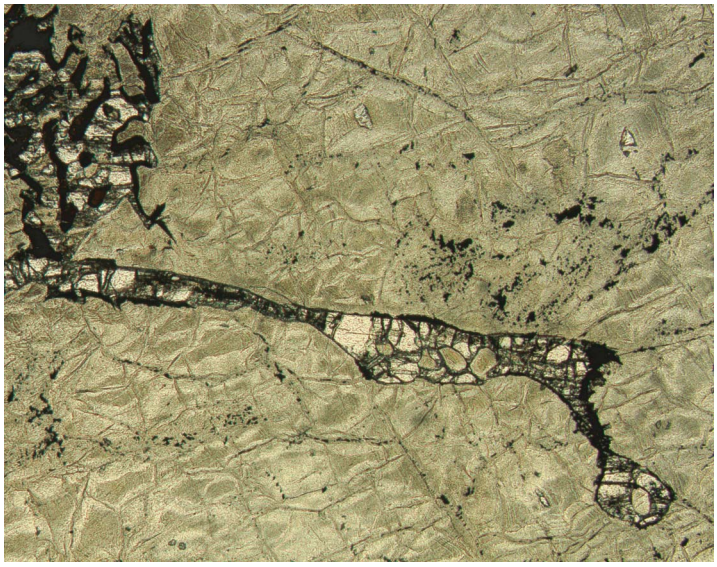

B

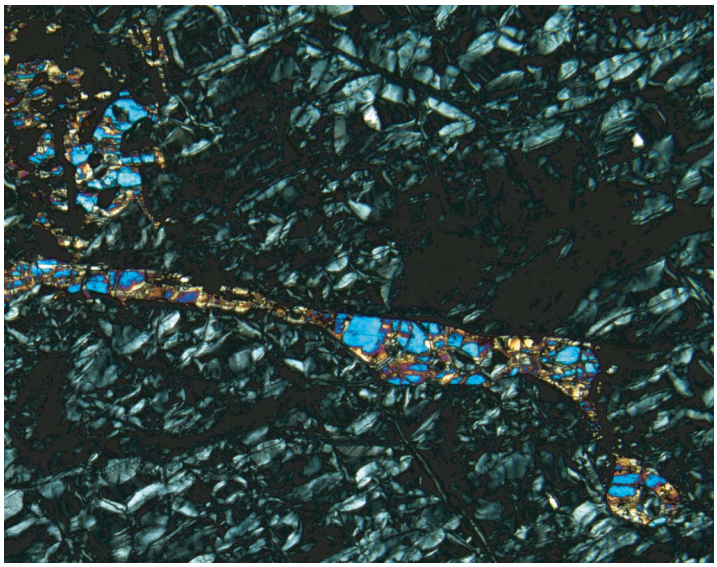

Figure F23. Close-up photograph of gabbro in Unit I (interval 209-1274A-11R-1, 43–55 cm).

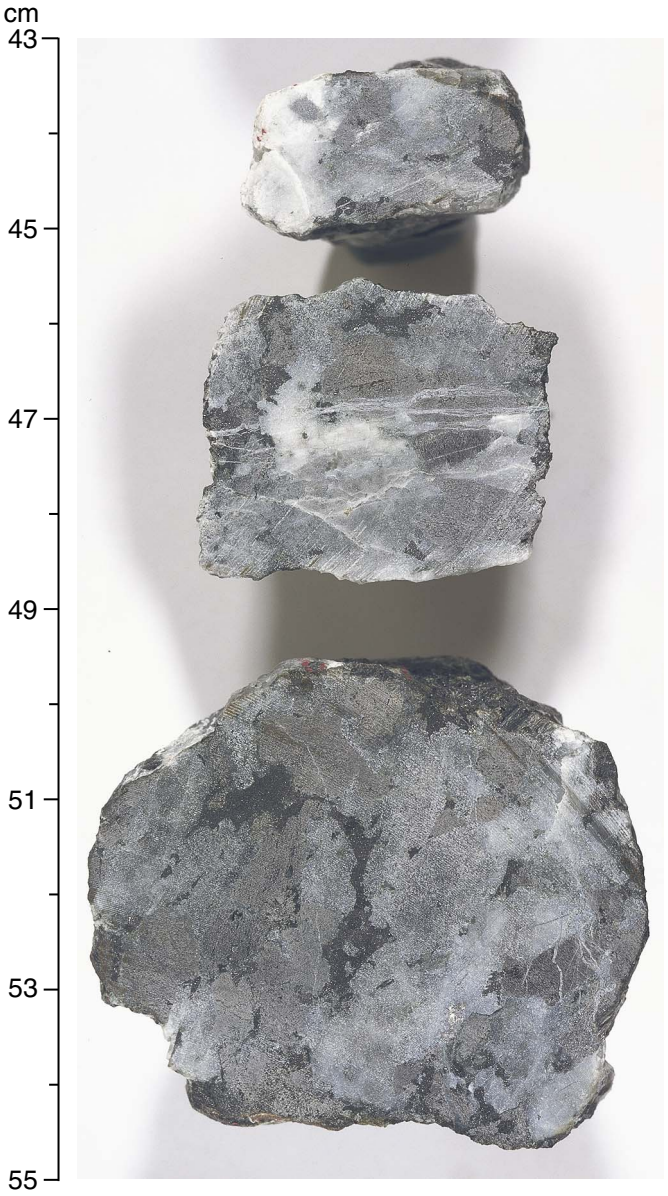

Figure F24. Photomicrograph showing 120° triple junctions between recovered plagioclase neoblasts (Sample **209-1274A-11R-1, 46–49 cm**) (cross-polarized light: blue filter; field of view = 2.75 mm; image 1274A_067).

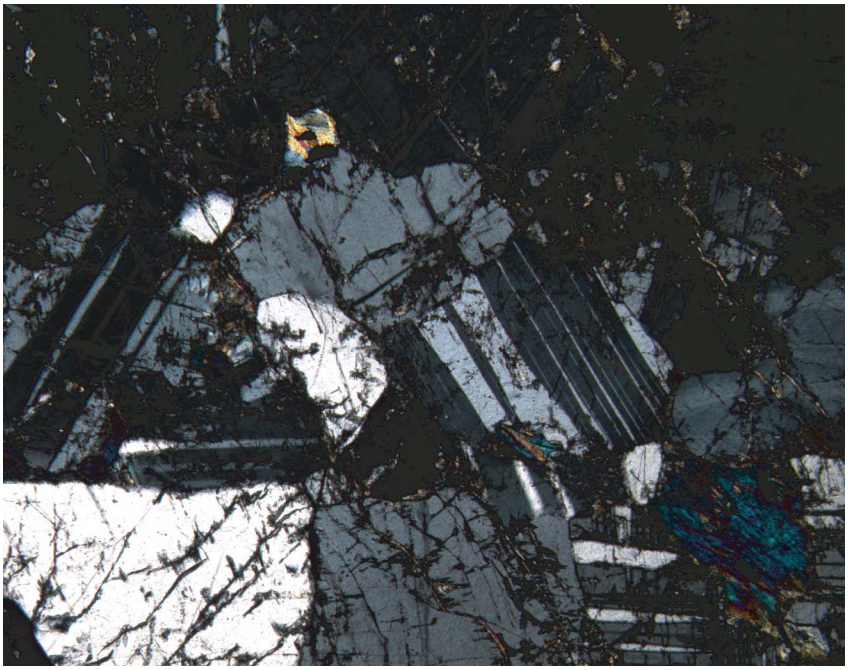

Figure F25. Photomicrograph showing bent plagioclase twins (Sample **209-1274A-11R-1, 46–49 cm**) (cross-polarized light; blue + light gray filters; field of view = 2.75 mm; image 1274A_066).

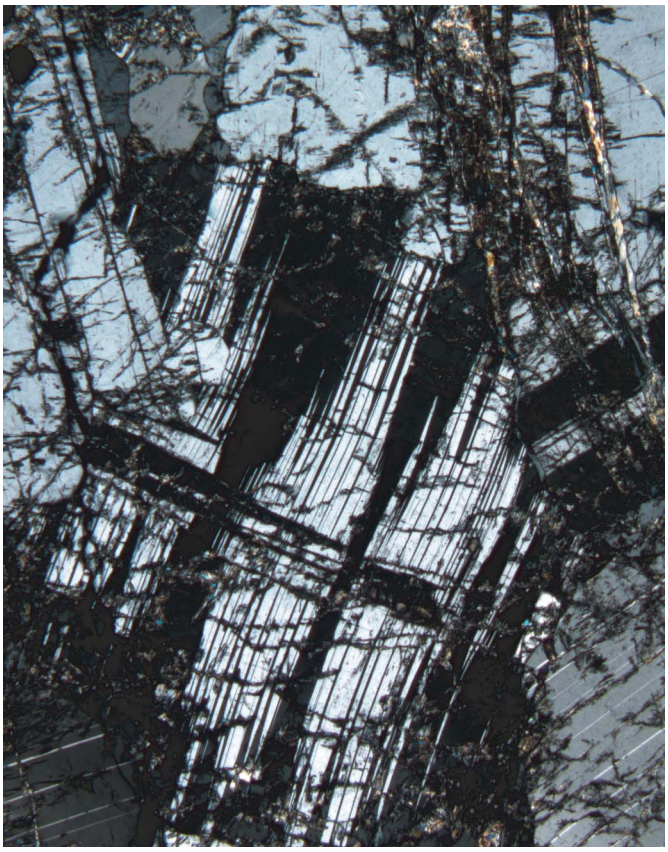

Figure F26. Close-up photograph of a reaction zone along harzburgite/gabbro contact in Unit II (interval 209-1274A-21R-1 [Piece 23, 91–98 cm]).

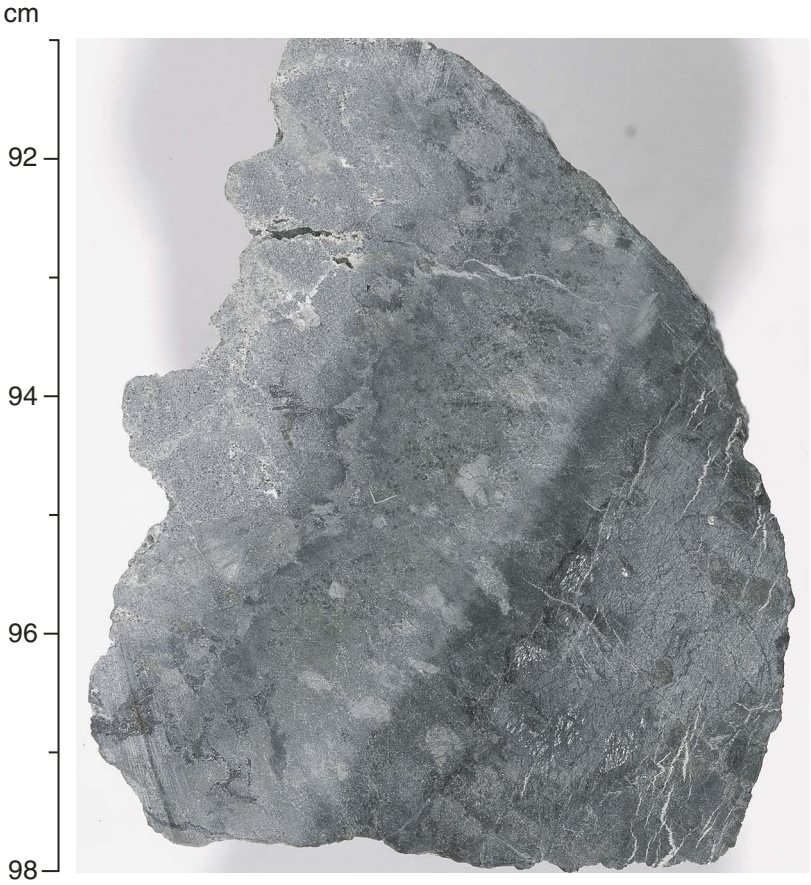

Figure F27. Brucite alteration is particularly common in dunite of Hole 1274A. **A.** Photograph of hand specimen of brucite-altered dunite (interval 209-1274A-20R-1, 141–149 cm). **B.** XRD analysis of Sample 209-1274A-20R-1, 141–144 cm, shows that brucite alteration is particularly prominent in this dunite. However, brucite and serpentine are indistinguishable in hand specimen.

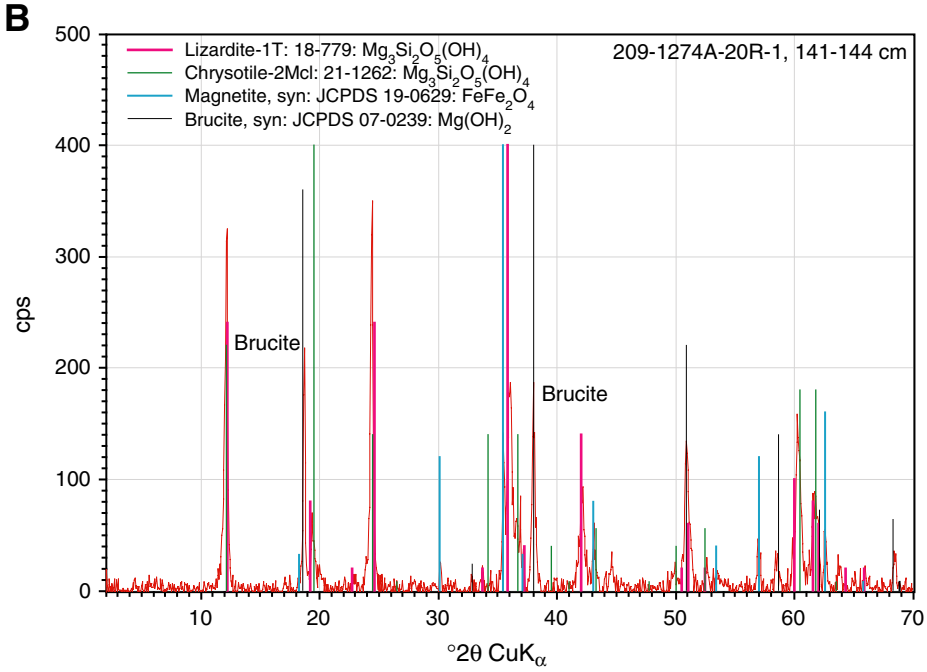

Figure F28. A. Close-up photograph of serpentinized harzburgite (interval 209-1274A-17R-2, 14–25 cm). **B.** XRD analysis of Sample 209-1274A-17R-2, 16–19 cm, indicating the presence of serpentine (lizardite) and orthopyroxene. **C.** Photomicrograph showing typical orthopyroxene (opx) partially pseudomorphed by bastite (b), while olivine is altered to prominent mesh-textured serpentine with relict olivine crystals (o) in the mesh centers. Fine serpentine-magnetite and chrysotile veinlets crosscut the serpentinized olivine groundmass and the pseudomorphed orthopyroxene (arrow) (Sample **209-1274A-17R-2, 14–17 cm**) (plane-polarized light: blue + light gray filters; field of view = 2.75 mm; image 1274A_019).

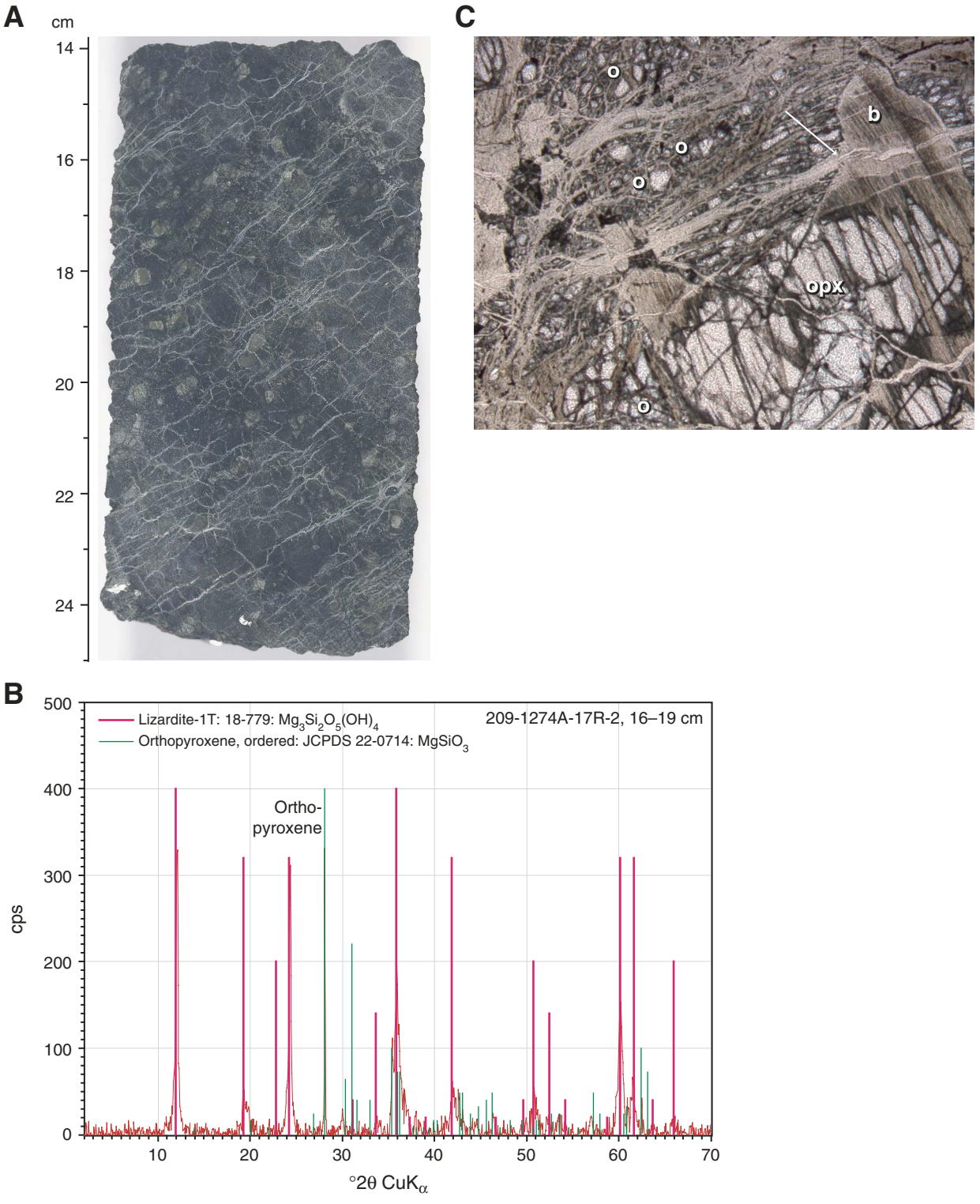

Figure F29. Photomicrographs showing kernels of olivine and brucite. **A.** Locally, olivine is preserved within the kernels of the serpentine mesh texture. Along its margins it is replaced by a mineral assemblage consisting of brucite (b), serpentine (s), and magnetite (arrow) (Sample **209-1274A-17R-1, 39–42 cm**) (cross-polarized light: blue filter + condenser lens; field of view = 0.7 mm; image 1274A_017). **B.** Locally, relict olivine kernels are surrounded by serpentine (s) and brucite (b), forming a mesh texture (Sample **209-1274A-11R-1, 7–12 cm**) (plane-polarized light; field of view = 0.7 mm; image 1274A_059). **C.** Brucite (b) (anomalous brown interference colors) in dunite is readily recognizable, forming kernels within the serpentine mesh texture (Sample **209-1274A-17R-1, 39–42 cm**) (cross-polarized light: blue filter; field of view = 1.4 mm; image 1274A_018).

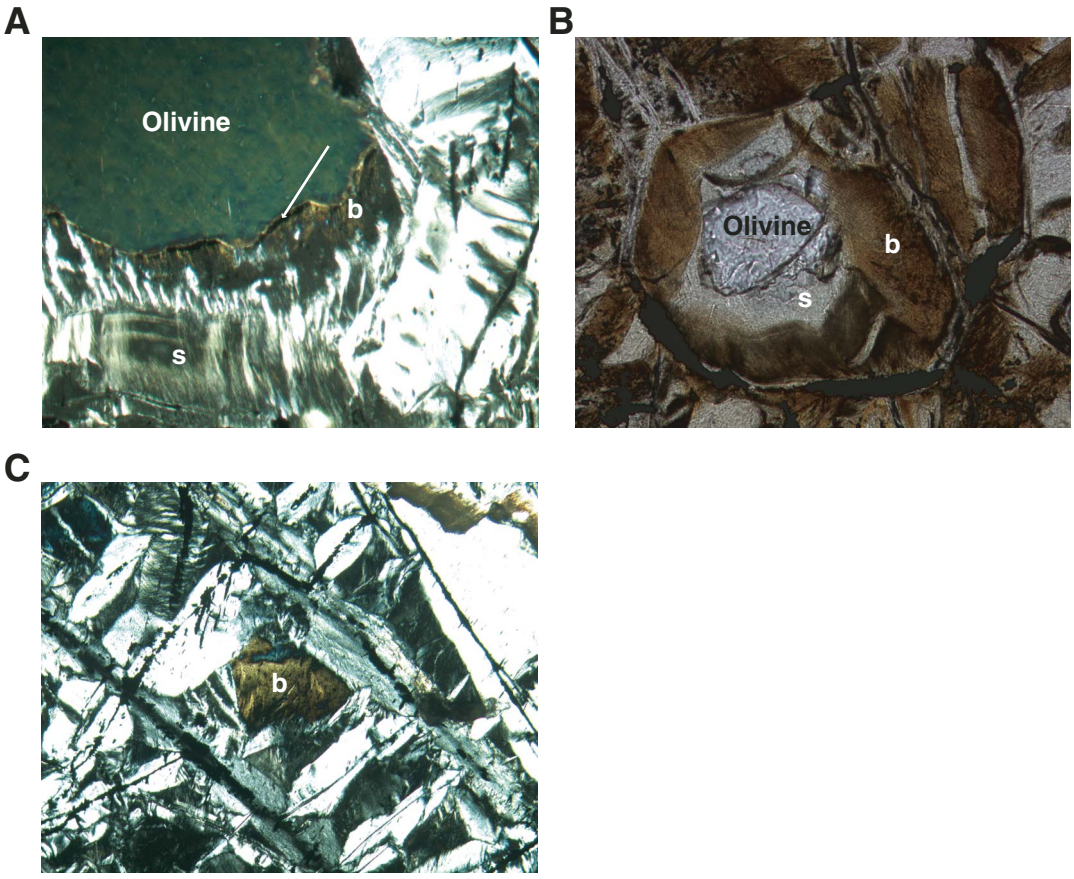

Figure F30. A. Downhole variation of alteration intensity. **B.** Running average of alteration intensity of harzburgites and dunites in Hole 1274A. **C.** Percentage of red alteration halos. All data are based on visual core descriptions. TD = total depth.

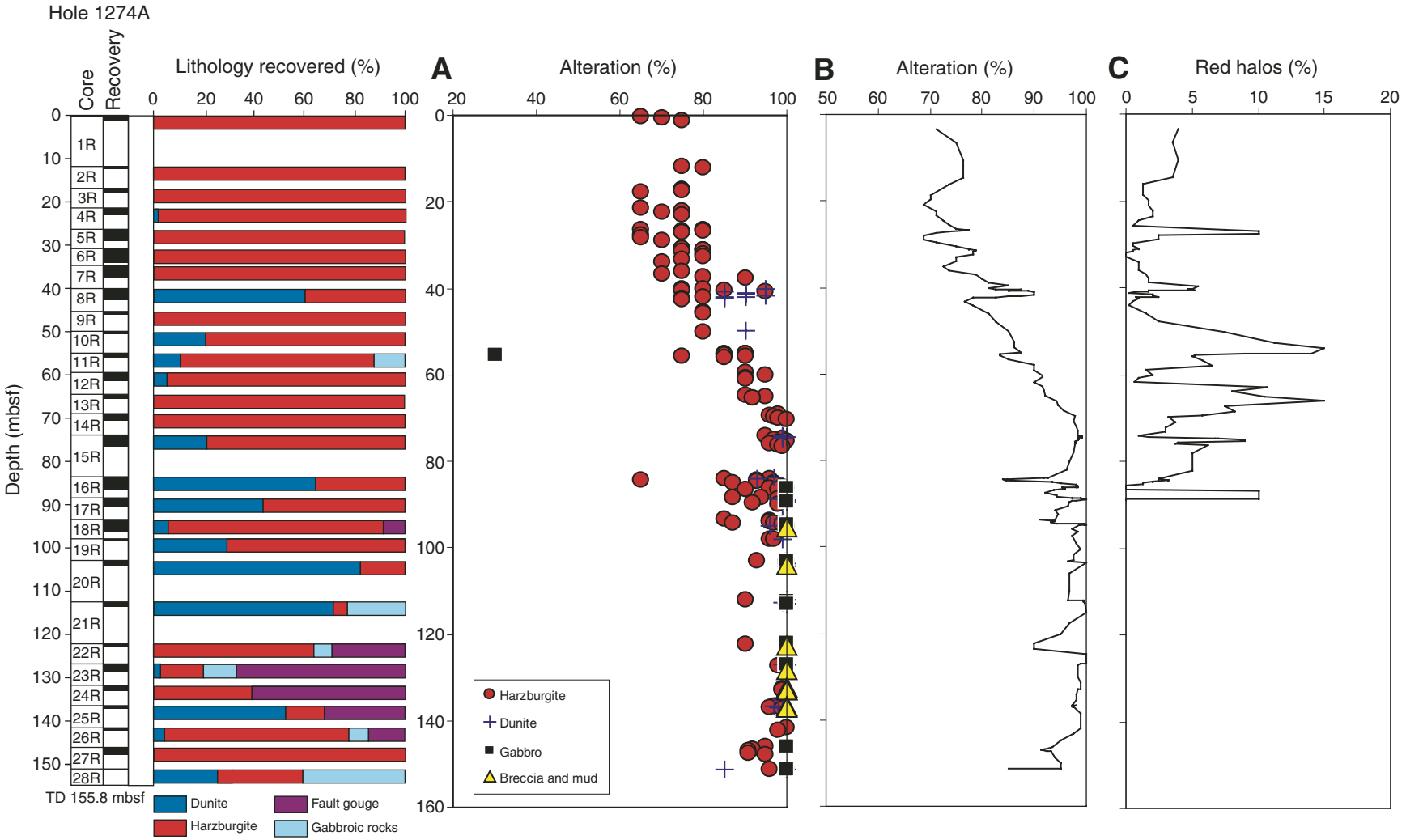

Figure F31. Photograph of prominent orange-brown halos typically developed along aragonite veins in serpentinized harzburgite in the upper part of Hole 1274A. These consist of iron oxyhydroxide–carbonate–clay and indicate oxidative conditions during alteration (interval 209-1274A-10R-1, 44–53 cm).

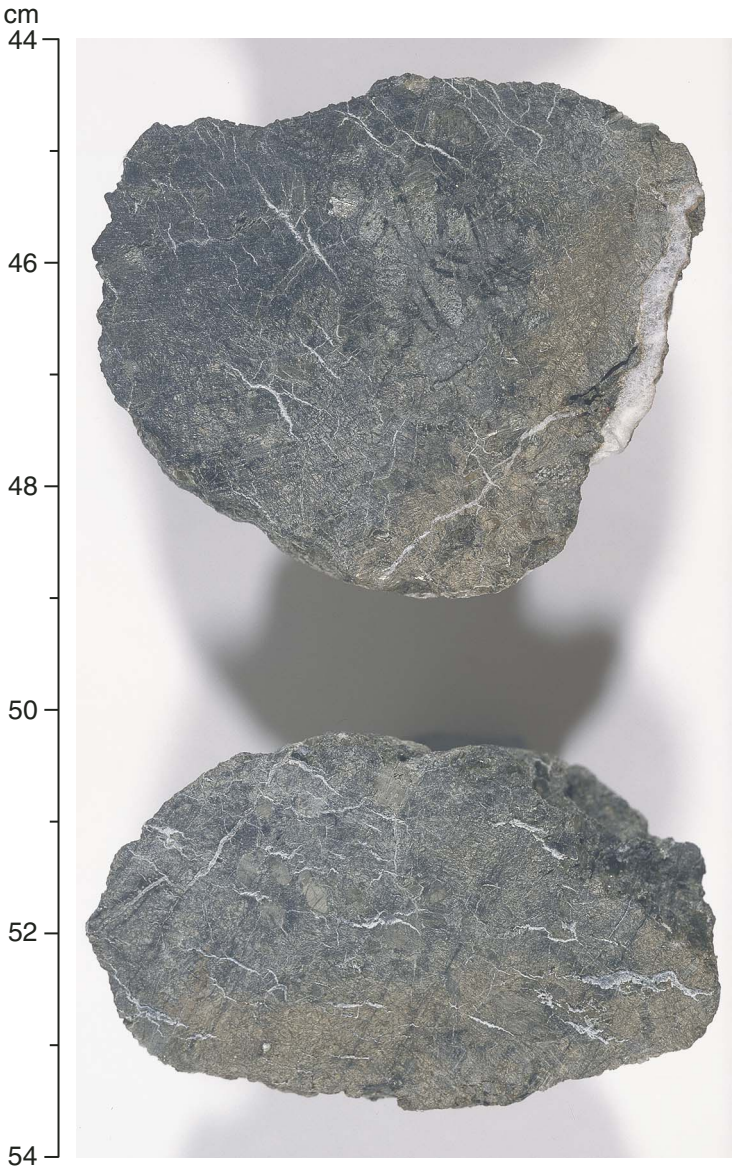

Figure F32. A. Close-up photograph of a greenish serpentine mud breccia (interval 209-1274A-23R-2, 0–10 cm). Arrow indicates approximate area from which a sample for XRD analyses (B) was taken. **B.** XRD analysis of Sample 209-1274A-23R-2, 0–3 cm, revealing the presence of serpentine and magnetite. **C.** Photograph of a grayish-black serpentine mud breccia (interval 209-1274A-23R-2, 60–70 cm). Arrow indicates approximate area from which a sample for XRD analysis (D) was taken. **D.** XRD analysis of Sample 209-1274A-23R-2, 67–70 cm, revealing the presence of serpentine, magnetite, and nontronite. Note that magnetite is more abundant in this sample than in the green serpentine mud breccia.

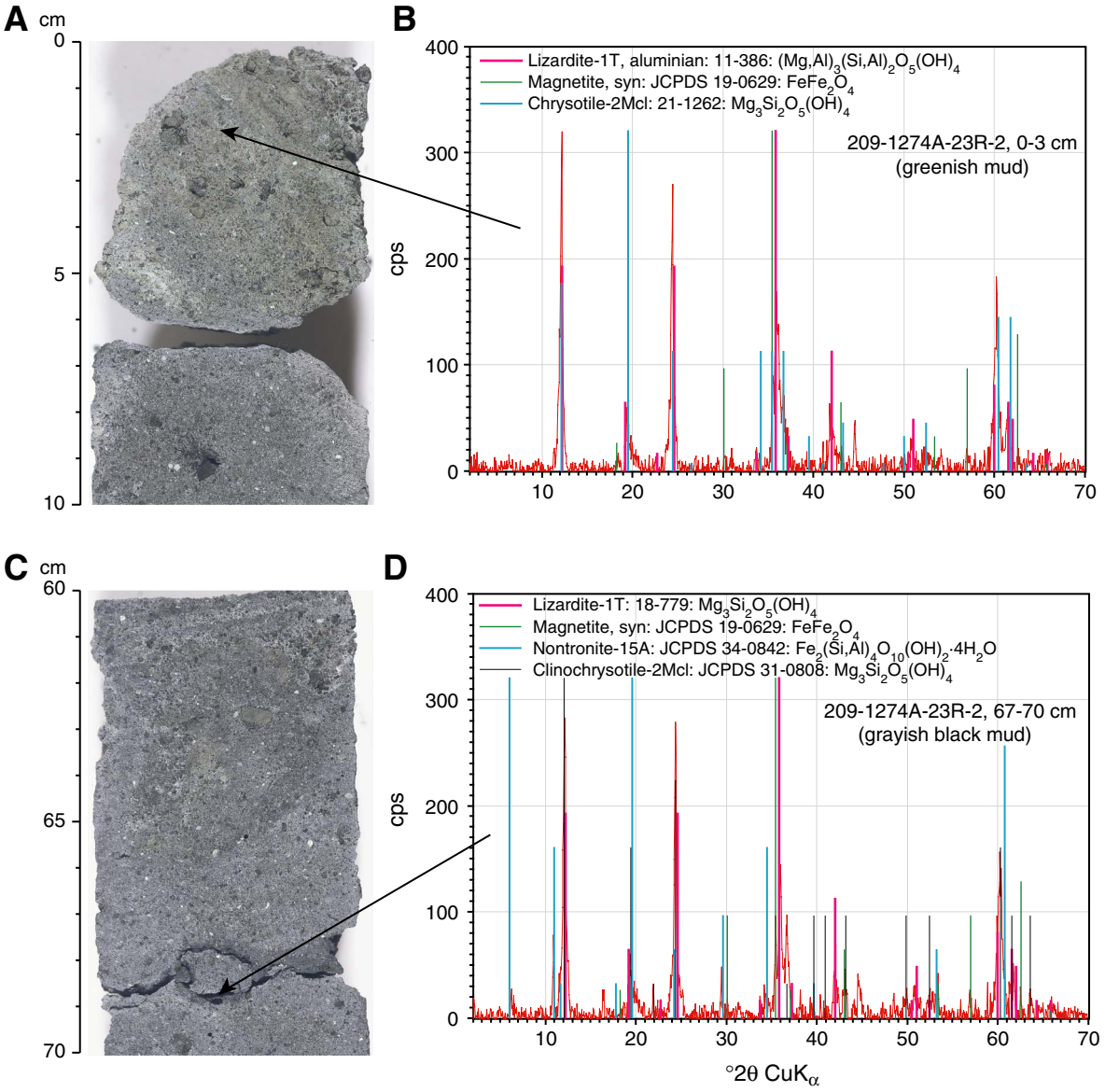

Figure F33. A. Photomicrograph showing patchy replacement of plagioclase by prehnite (prh) (Sample 209-1274A-11R-1, 46–49 cm) (cross-polarized light: blue filter; field of view = 2.75 mm; image 1274A_016). **B.** Close-up photograph of a rodingitized gabbro (interval 209-1274A-21R-1, 12–20 cm). **C, D.** Photomicrographs of Sample 209-1274A-21R-1, 12–17 cm (cross-polarized light: blue filter; field of view = 2.75 mm); (C) zoisite (zoi) replacing plagioclase (image 1274A_022); (D) euhedral andradite (and) crystal (image 1274A_023).

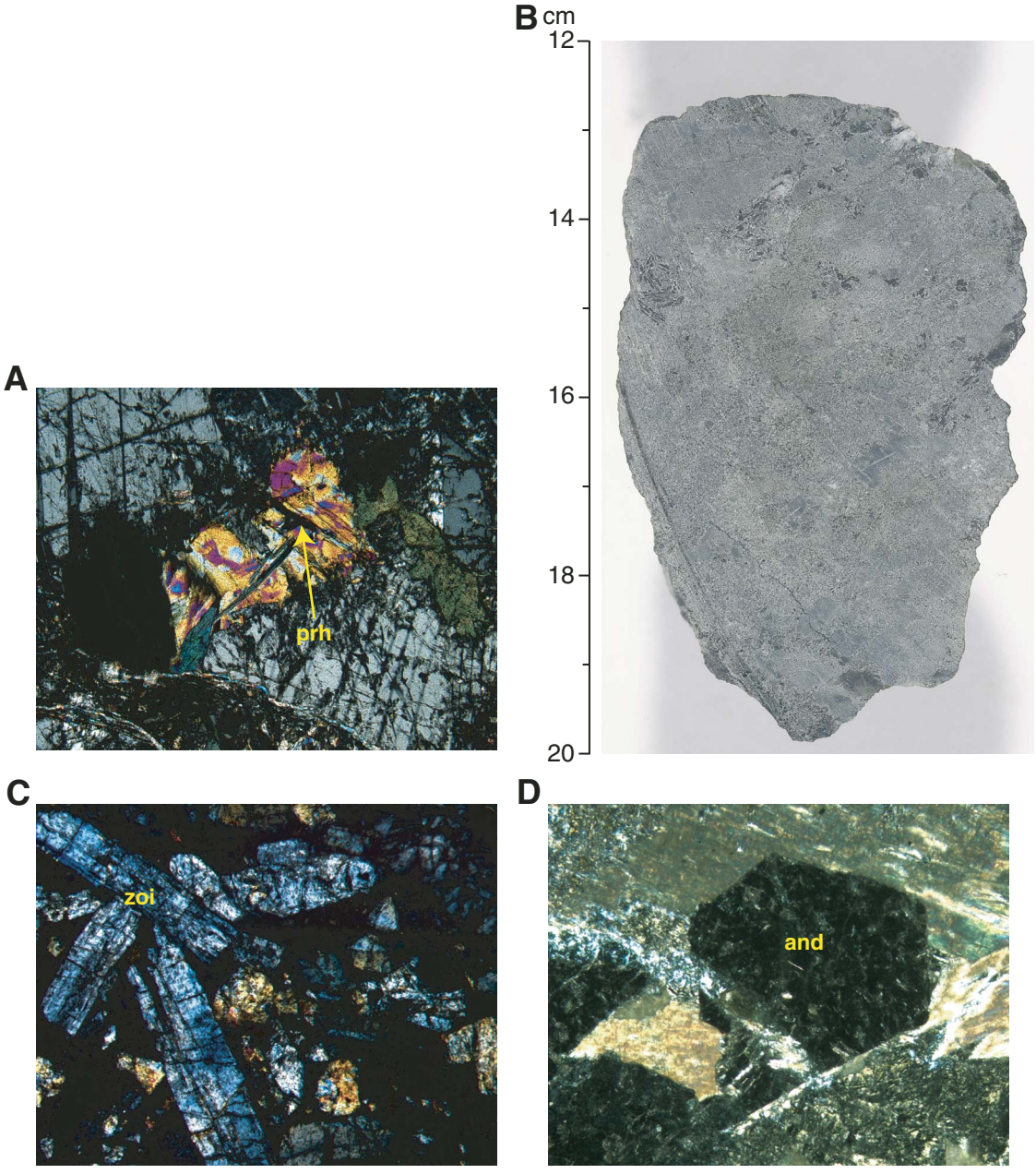

Figure F34. Relative proportions of vein minerals in Hole 1274A.

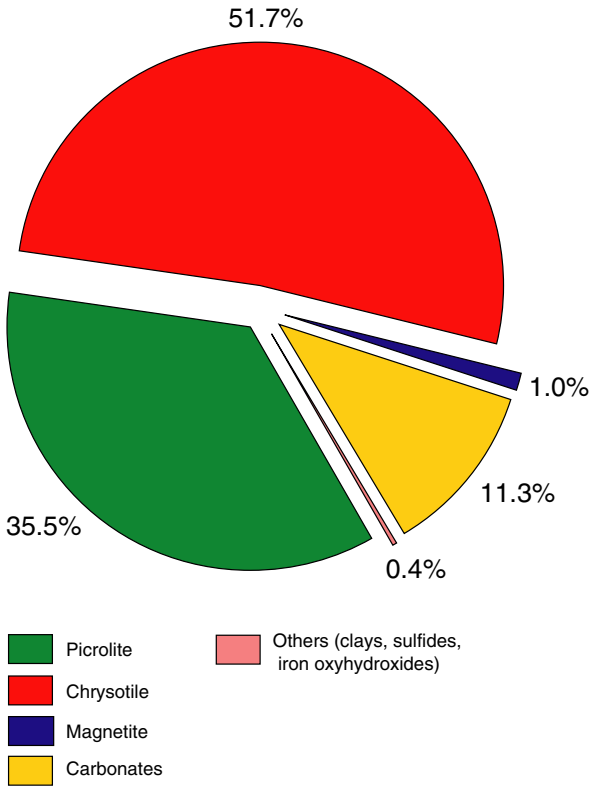

Figure F35. **A.** Downhole variations of picrolite and chrysotile abundance in veins. **B.** Abundances of paragranular and transgranular chrysotile veins. **C.** Aragonite and magnetite abundance in veins. Horizontal lines mark positions of fault gouges.

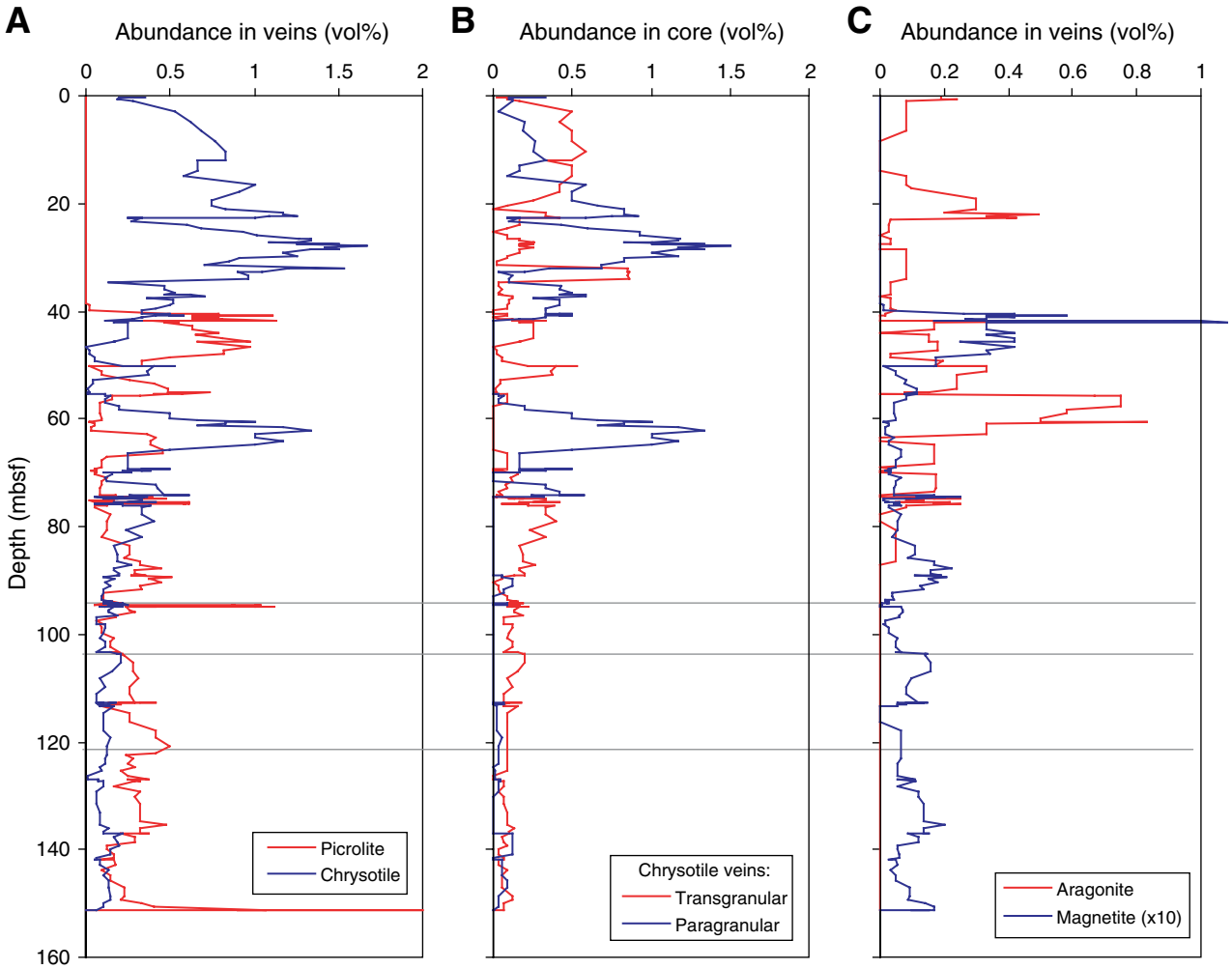

Figure F36. Photomicrographs showing protogranular textured orthopyroxenes in Hole 1274A harzburgites. Ol = olivine, Opx = orthopyroxene. **A.** Granular orthopyroxene (Sample 209-1274A-8R-1 [Piece 10, 61–64 cm]) (cross-polarized light [XPL]; field of view [FOV] = 5.5 mm; image 1274A_115). **B.** Protogranular orthopyroxene (Sample 209-1274A-4R-1 [Piece 3, 52–54 cm]) (XPL: blue + light gray filters; FOV = 11 mm; image 1274A_075). **C.** Protogranular orthopyroxene with occluded olivine (Sample 209-1274A-5R-2 [Piece 1, 17–29 cm]) (XPL; FOV = 2.75 mm; image 1274A_094). **D.** Irregular protogranular texture (Sample 209-1274A-6R-2 [Piece 1, 62–64]) (XPL; FOV = 5.5 mm; image 1274A_100).

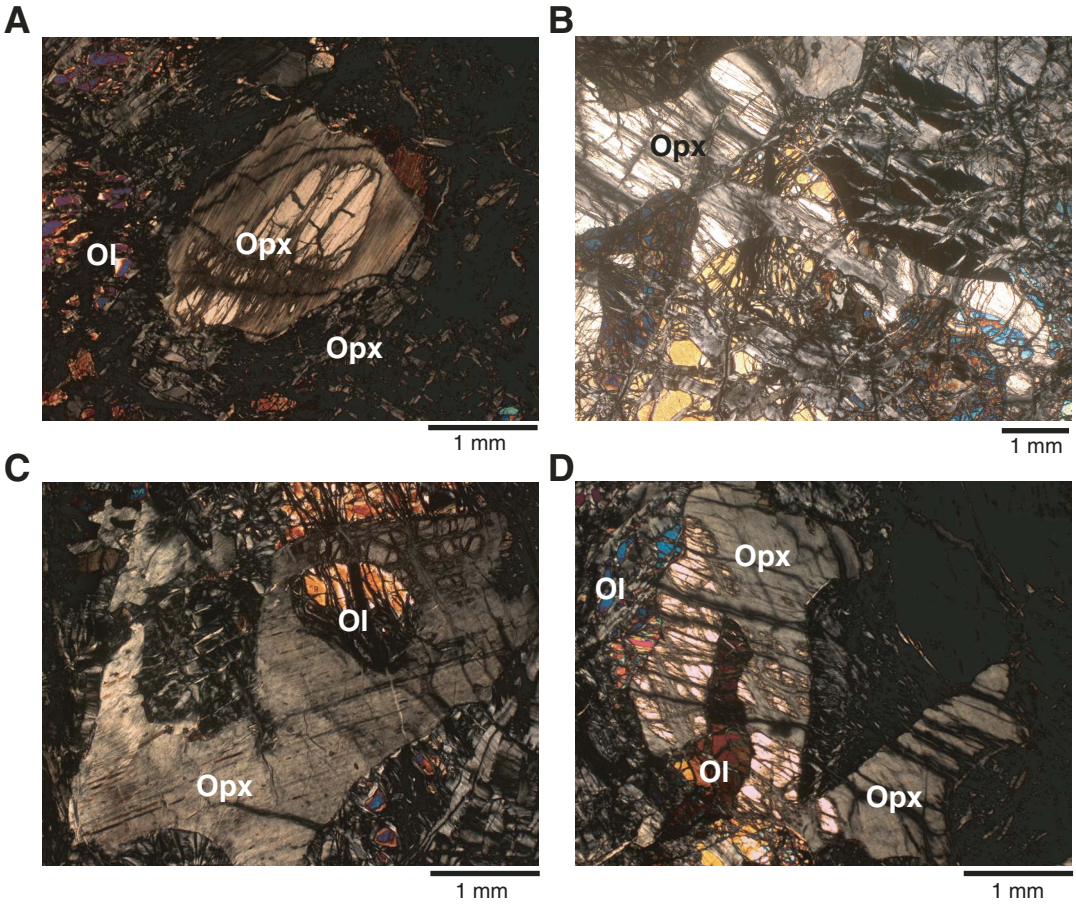

Figure F37. Photomicrographs showing high-temperature deformation textures in harzburgites from Hole 1274A. Opx = orthopyroxene, Ol = olivine. **A.** Kink bands in orthopyroxene (Sample **209-1274A-13R-1 [Piece 1, 3–6 cm]**) (cross-polarized light [XPL]; field of view [FOV] = 5.5 mm; image 1274A_127). **B.** Kink bands with clinopyroxene exsolution along the boundaries (Sample **209-1274A-5R-2 [Piece 1, 17–29 cm]**) (XPL; FOV = 1.4 mm; image 1274A_96). **C.** Parallel kink bands in olivine and orthopyroxene (Sample **209-1274A-2R-1 [Piece 1, 0–3 cm]**) (XPL; FOV = 2.75 mm; image 1274A_126). **D.** Neoblasts formed at old kink band boundaries (Sample **209-1274A-8R-1 [Piece 10, 61–64 cm]**) (XPL; FOV = 2.75 mm; image 1274A_113). Note the interstitial clinopyroxene. Neoblasts and porphyroclasts show no signs of internal strain. (Continued on next page.)

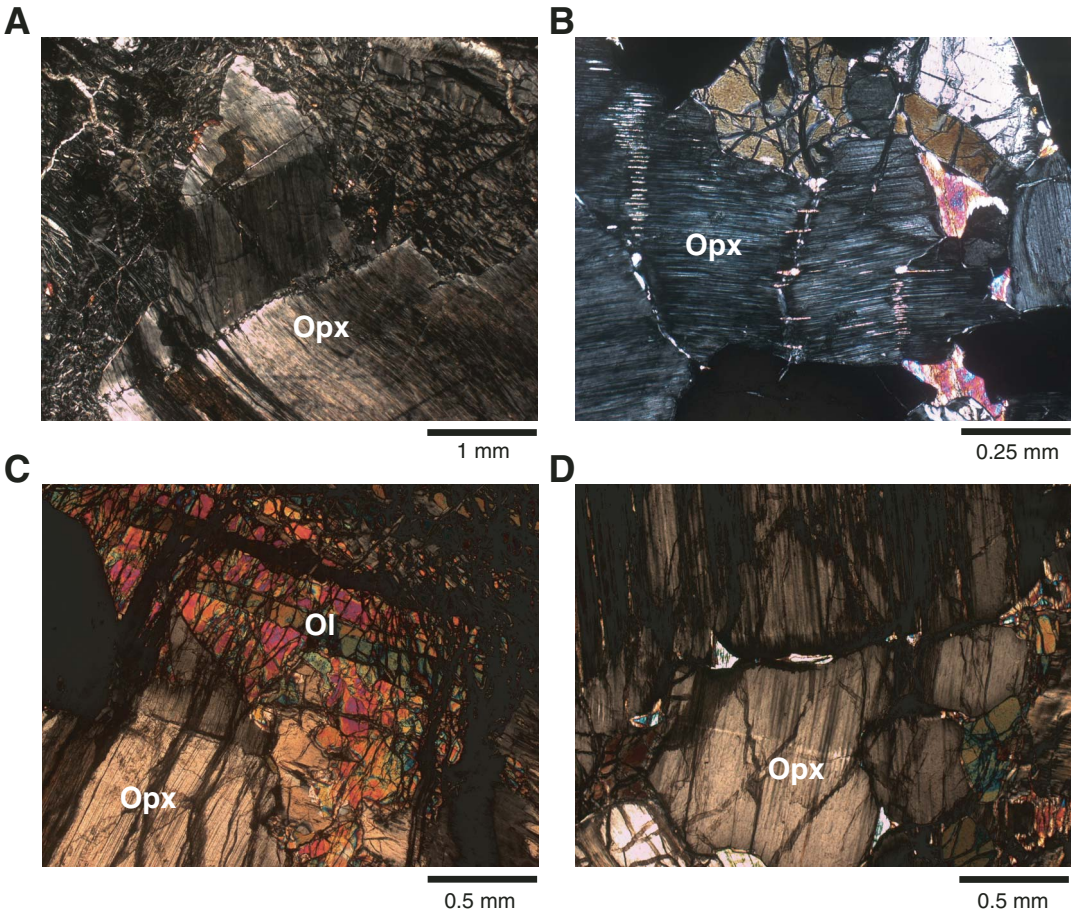

Figure F37 (continued). E. Polygonalized neoblasts of orthopyroxene (Sample **209-1274A-18R-1 [Piece 19, 115–118 cm]**) (XPL; FOV = 5.5 mm; image 1274A_138). **F.** Neoblasts of orthopyroxene with incipient polygonalization (Sample **209-1274A-22R-1 [Piece 4A, 20–23 cm]**) (XPL; FOV = 1.4 mm; image 1274A_139). **G.** Neoblast formation along kink bands and grain boundaries (Sample **209-1274A-12R-1, 98–101 cm**) (XPL: blue filter; FOV = 2.75 mm; image 1274A_103).

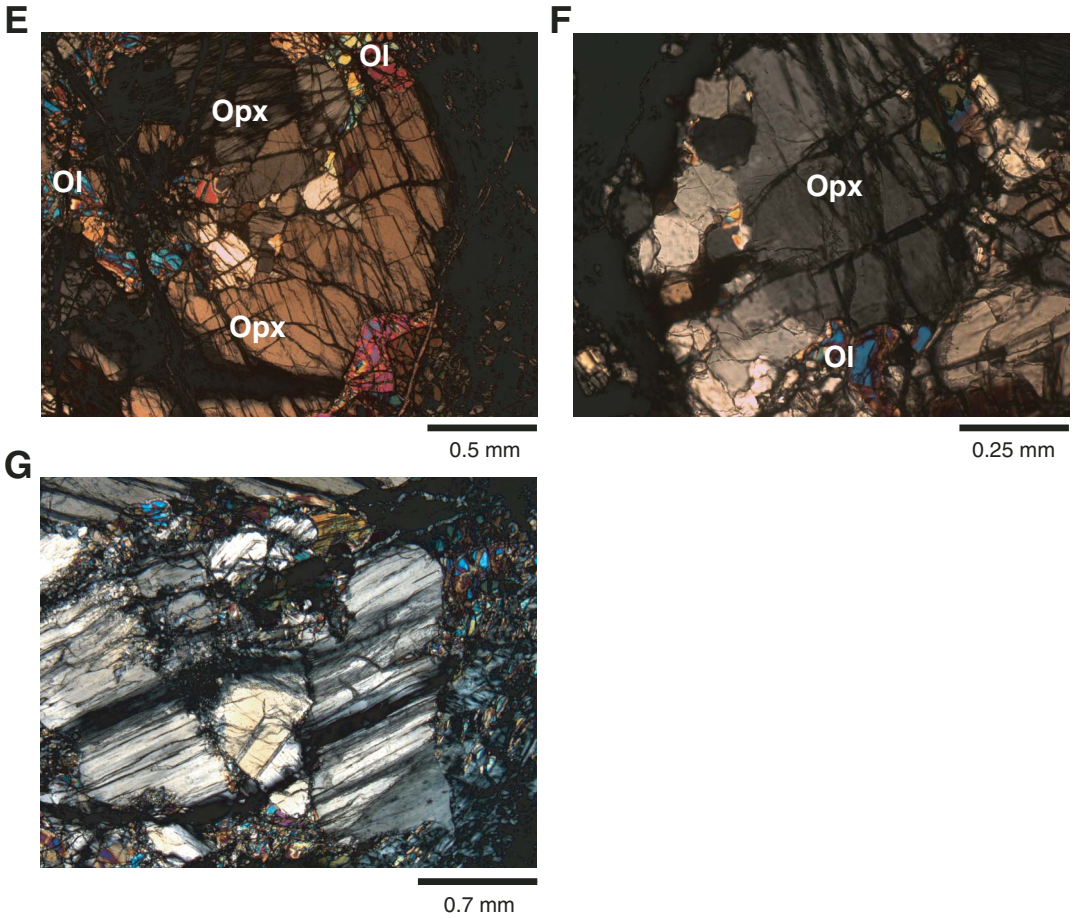

Figure F38. Downhole plot of crystal-plastic deformation, brittle deformation, and alteration vein intensities in Hole 1274A and locations of main deformation features. Expanded depth of cored interval is plotted on the vertical axis. Recovery column: black bars = actual core recovery, yellow cones = depth range of expansion for each core; Lithology column: green = harzburgites and dunites, red = gabbros, black = intervals of gouge material. Intensity estimate is based on visual core description of individual core pieces. Intensities are plotted as a running downhole average of seven pieces weighted by piece length at each depth (468 pieces total). Crystal-plastic deformation intensities were not recorded for the gouge zones. TD = total depth.

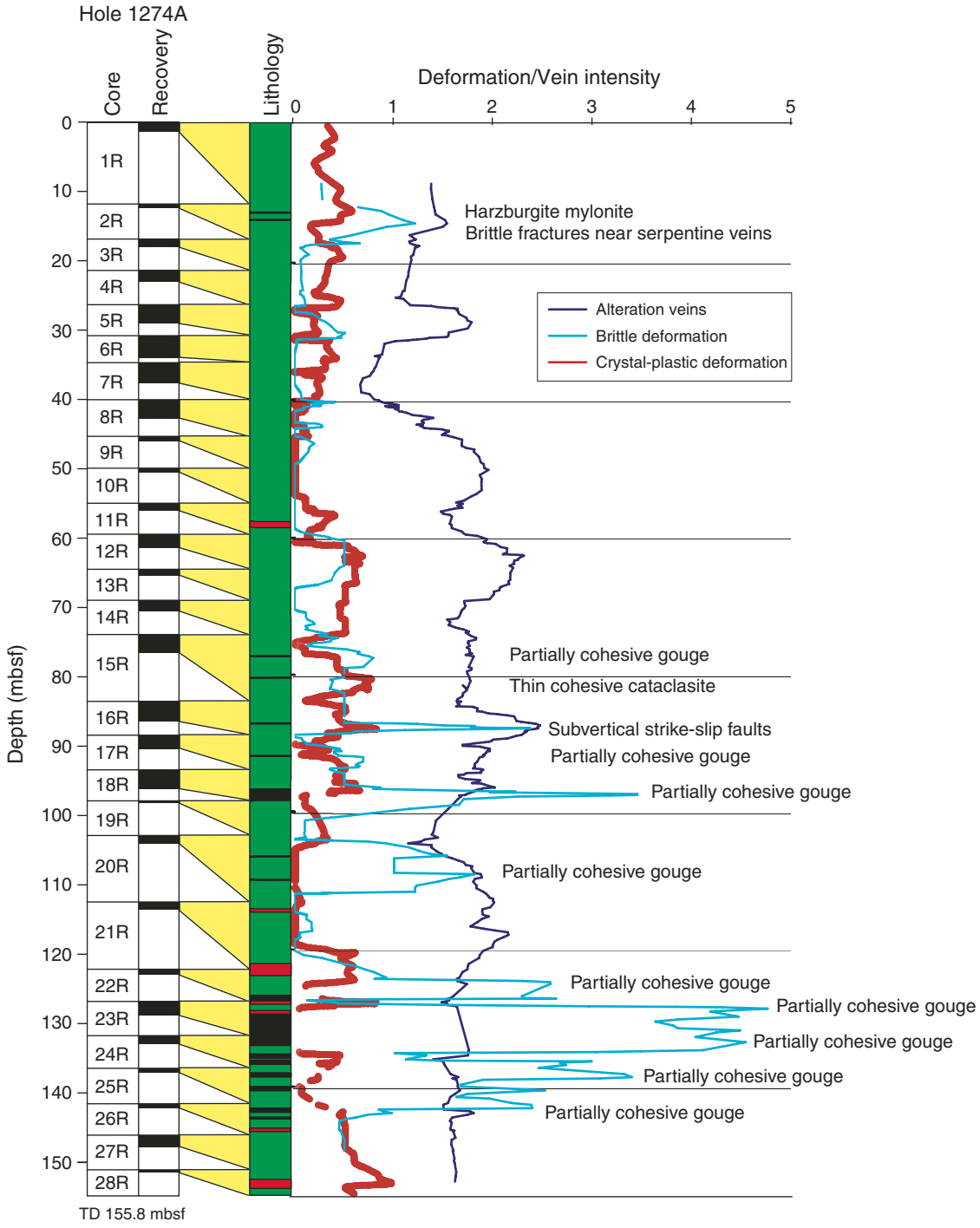

Figure F39. Crystal-plastic deformation (CPf) intensity for Hole 1274A using a scale from 0 (undeformed) to 5 (ultramylonite) as explained in the **"Explanatory Notes"** chapter. A total of 3250 cm of core was logged in 458 pieces from the hole. Plot and totals exclude recovered sand, gravel, and fault gouge.

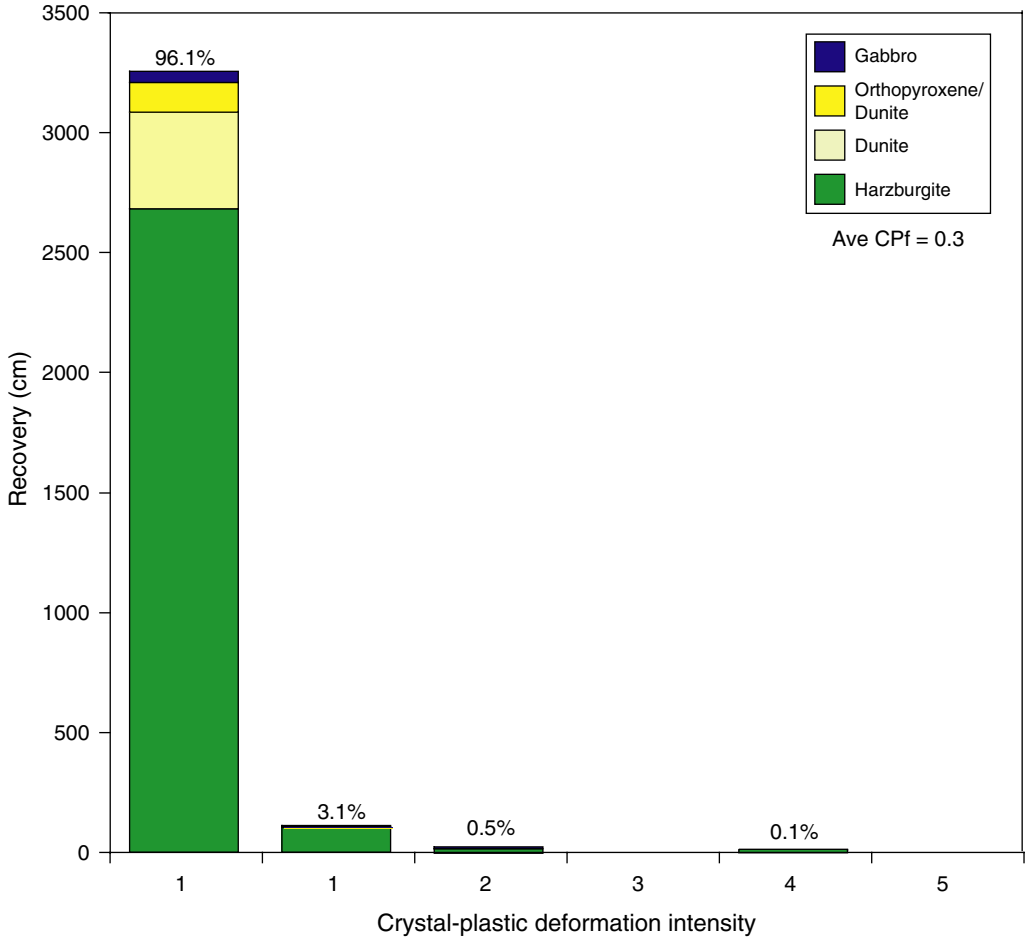

Figure F40. Photomicrographs of deformation textures in a weathered harzburgite mylonite (Sample 209-1274A-2R-1 [Piece 1, 0–3 cm]). Opx = orthopyroxene, Ol = olivine, Sp = spinel. **A.** Recrystallized olivine (Ol_2) between stretched orthopyroxene porphyroclasts (cross-polarized light [XPL]; field of view [FOV] = 2.75 mm; image 1274A_133). **B.** Parallel kink bands in a stretched orthopyroxene grain (XPL; FOV = 1.4 mm; image 1274A_132). **C.** Olivine porphyroclasts (Ol_1) in a matrix of recrystallized olivine (XPL; FOV = 11 mm; image 1274A_105). **D.** Spinel-pyroxene-olivine porphyroclast located in a recrystallized olivine matrix (XPL; FOV = 2.75 mm; image 1274A_109).

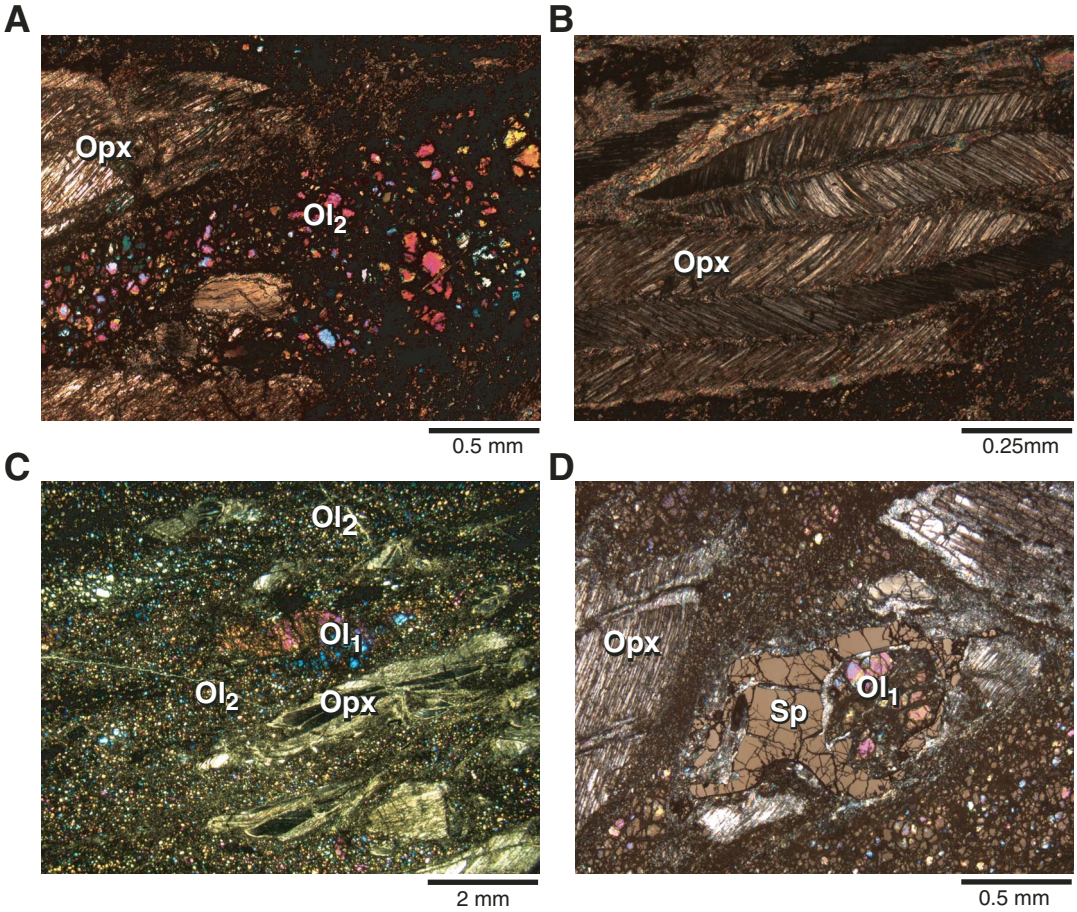

Figure F41. Lower hemisphere stereographic projection of poles to crystal-plastic foliations. **A.** Apparent dips as measured in the core face. **B.** Apparent dips rotated using the measured paleomagnetic declination back to a common orientation as described in **"Structures in Peridotite and Gabbroic Intrusions,"** p. 8, in "Mantle Upwelling, Melt Transport, and Igneous Crustal Accretion" in the "Leg 209 Summary" chapter. All samples have a normal polarity. All points are for protogranular shape fabrics in harzburgite.

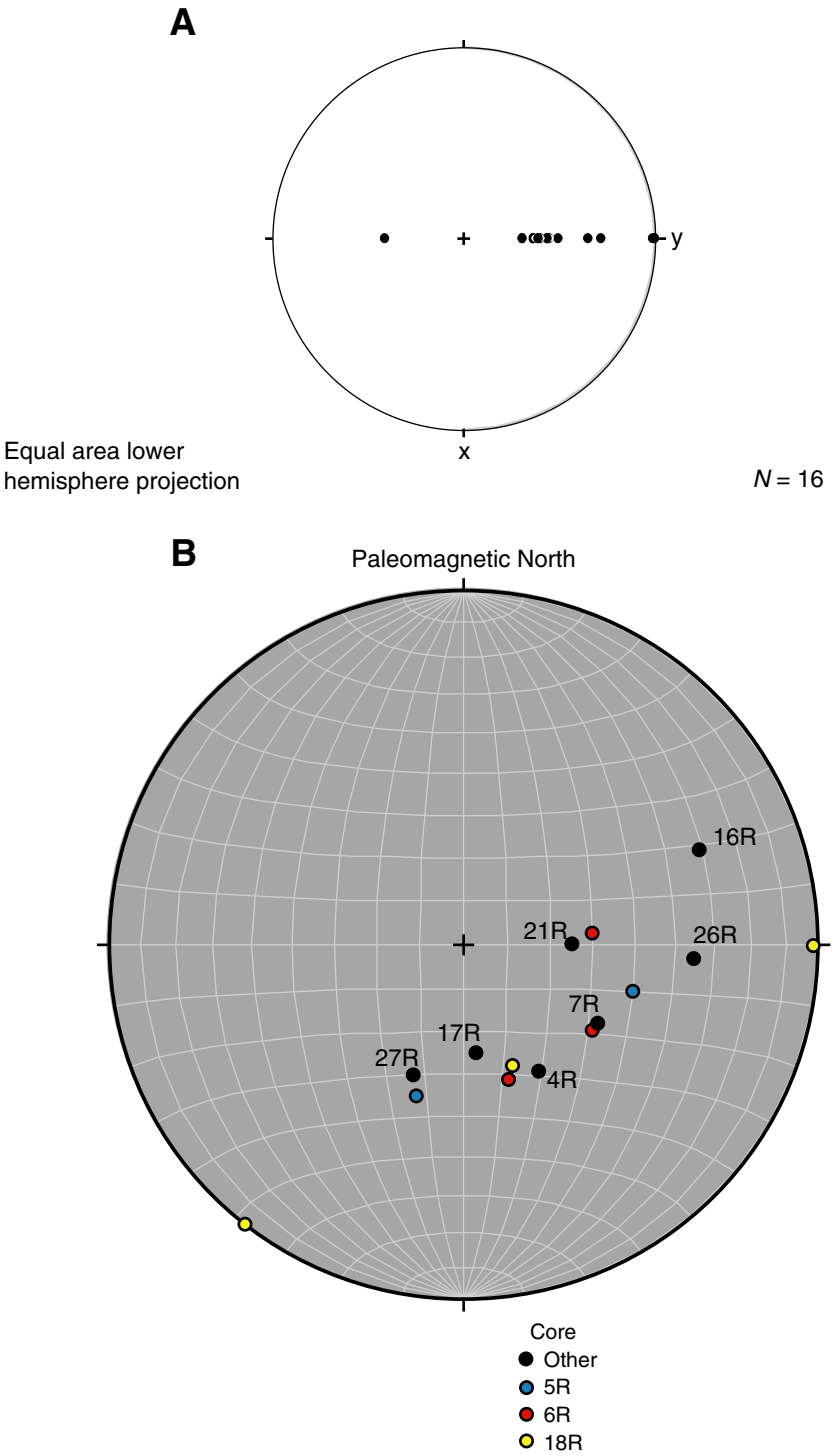

Figure F42. Photomicrographs of deformation textures in a weakly deformed oxide gabbro intruding Hole 1274A peridotites (Sample 209-1274A-11R-1 [Piece 10, 46–49 cm]; ~57 mbsf). **A.** Bent plagioclase with deformation twins (cross-polarized light: blue filter; field of view = 2.75 mm; image 1274A_066). **B.** Recrystallized plagioclase with polygonal grain boundaries (cross-polarized light; field of view = 5.5 mm; image 1274A_118.

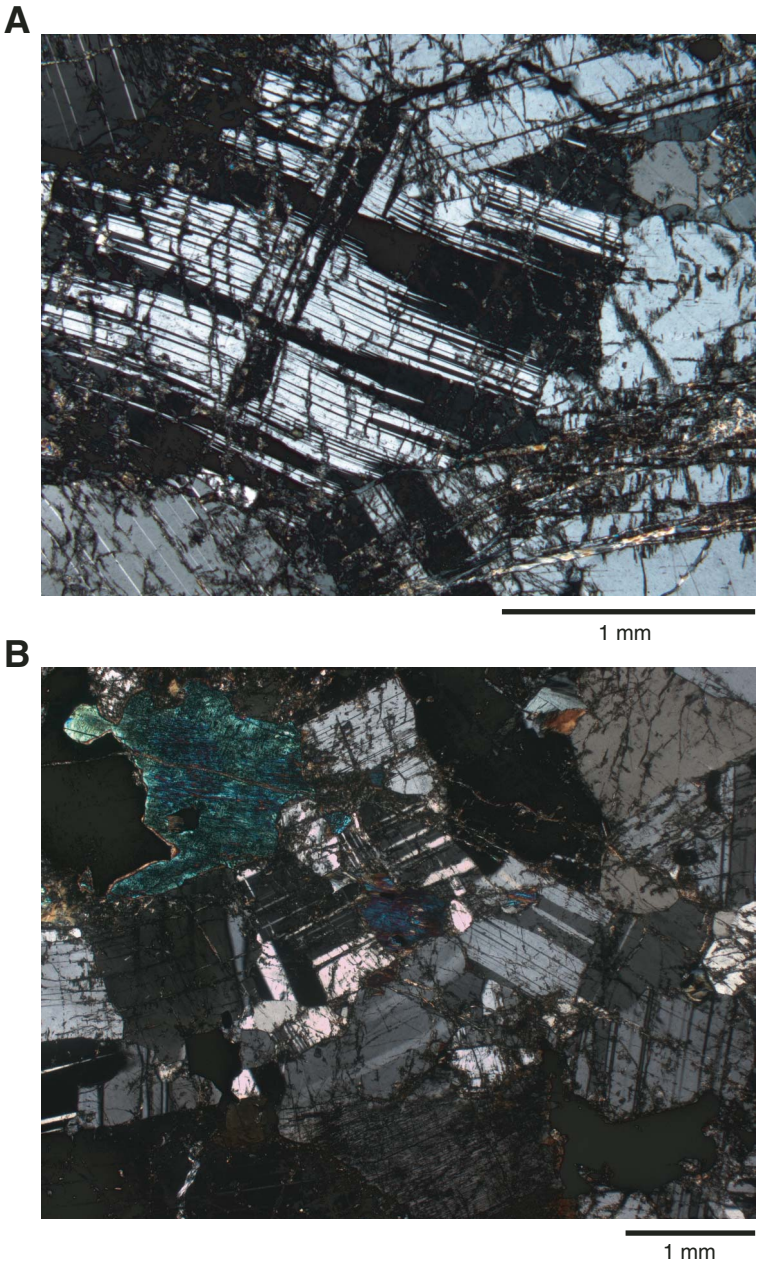

Figure F43. Photomicrograph of partially serpentinized harzburgite. Ribbon texture serpentine defines a moderate to weak foliation on the right side of the photo. Fine serpentine veins cut relict olivine grains between orthopyroxene porphyroclasts on the left side of the photo (Sample **209-1274A-7R-1 [Piece 7, 101–105 cm]**) (cross-polarized light: blue + light gray filters; field of view = 11 mm; image 1274A_140).

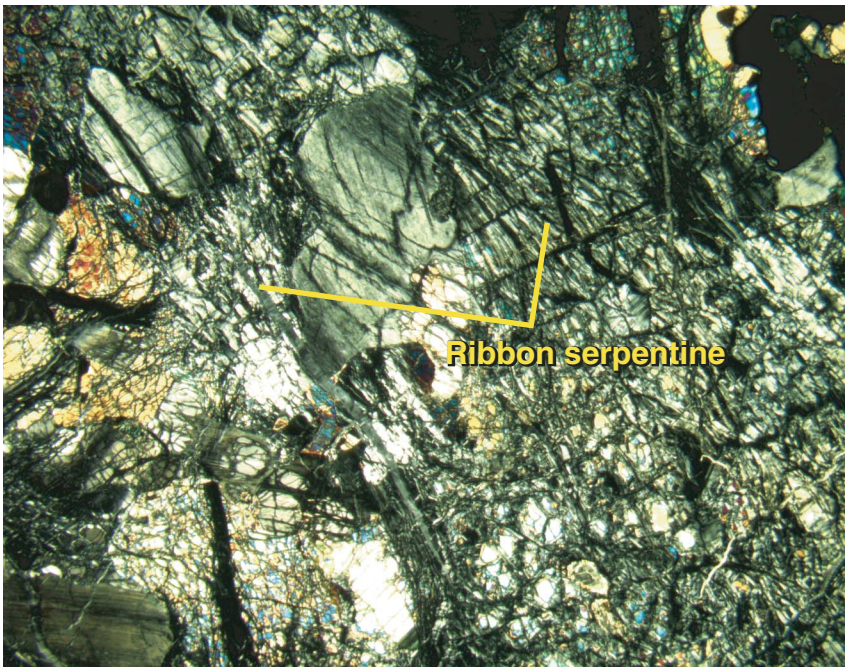

Figure F44. Examples of alteration veins and their crosscutting relationships in harzburgites and dunites from Hole 1274A. **A.** Typical serpentine foliation defined by chrysotile veins in a harzburgite (interval 209-1274A-17R-2, 5–12 cm). **B.** Weak serpentine foliation defined by chrysotile veins in a harzburgite with a conjugate set of more steeply dipping veins (interval 209-1274A-15R-2, 7–17 cm). **C.** An example of the mesh/anastomosing vein sets occasionally shown by the chrysotile veins in the harzburgites (interval 209-1274A-16R-2, 125–133 cm). **D.** Typical dunite, showing an early planar magnetite-serpentine vein, cut by a later white picrolite vein and sparse white chrysotile veins (interval 209-1274A-20R-1, 97–104 cm). (Continued on next page.)

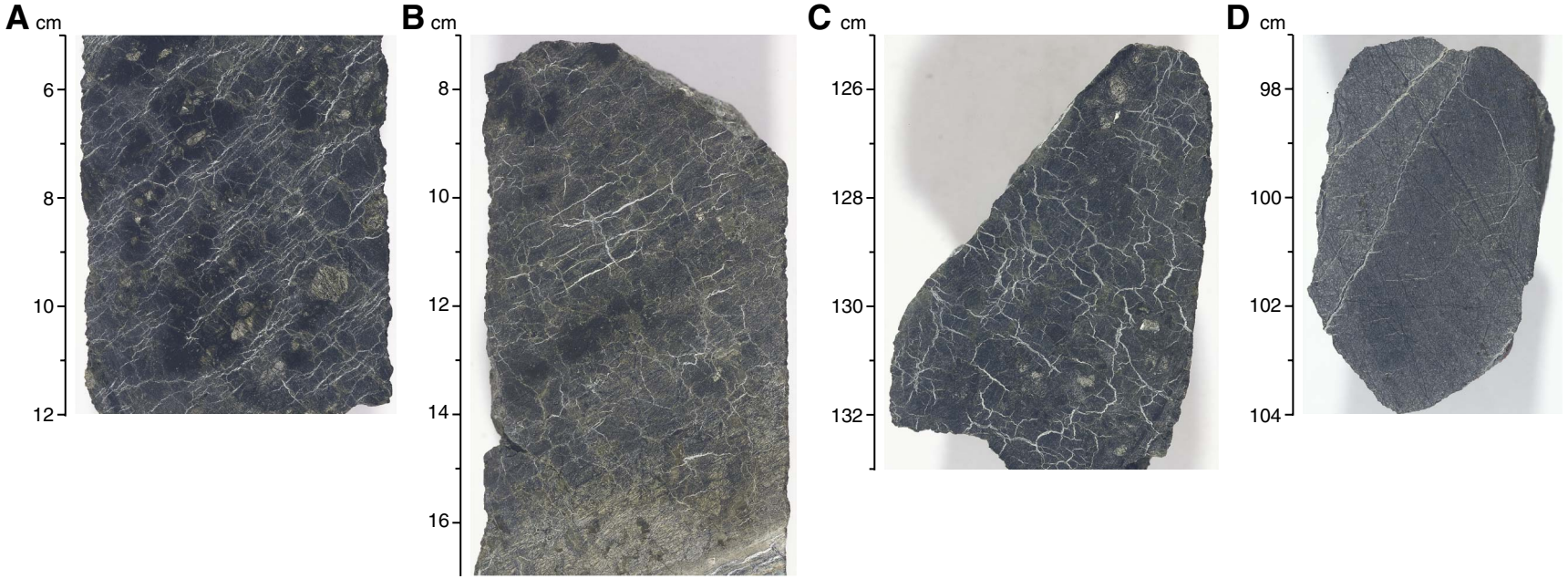

Figure F44 (continued). **E.** Harzburgite showing early pale gray picrolite vein cut by chrysotile veins (interval 209-1274A-5R-2, 108–117 cm). **F.** Harzburgite showing early black magnetite-serpentine vein cut by chrysotile veins (interval 209-1274A-27R-1, 124–133 cm). **G.** Harzburgite showing chrysotile vein foliation cut by late carbonate vein on the right side of the piece (interval 209-1274A-12R-1, 22–32 cm).

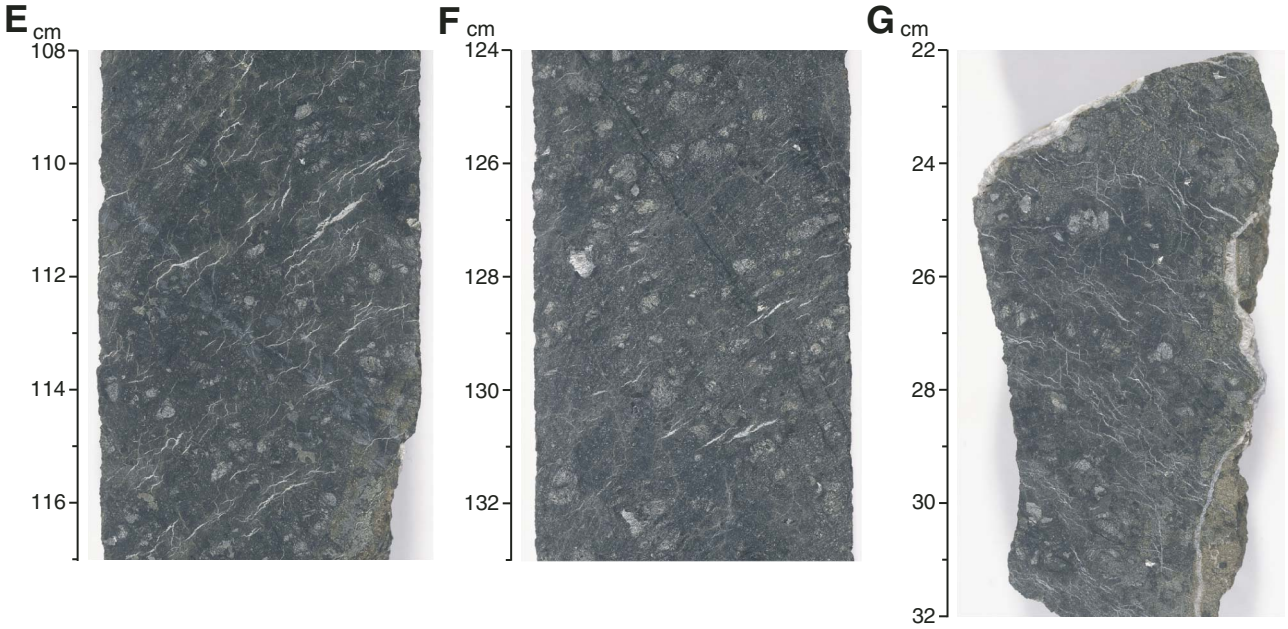

Figure F45. The dips of black magnetite-serpentine veins, the foliation delineated by the chrysotile veins, and the carbonate veins, with expanded depth in the core reference frame for Hole 1274A.

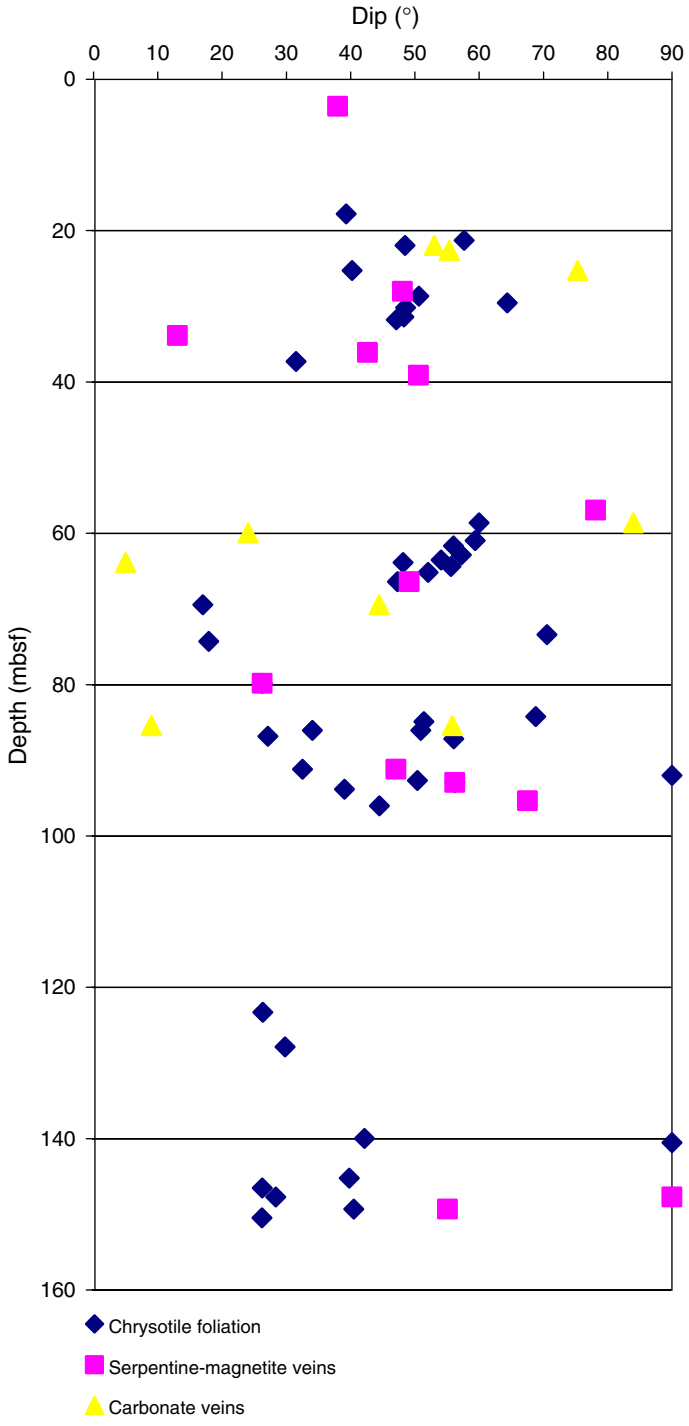

Figure F46. Lower hemisphere equal-area stereographic projection of poles to brittle shear zones and fractures and the chrysotile foliation in Hole 1274A, measured in the core reference frame and rotated using the measured paleomagnetic declination back to a common orientation as described in **"Structures in Peridotite and Gabbroic Intrusions,"** p. 8, in "Mantle Upwelling, Melt Transport, and Igneous Crustal Accretion" in the "Leg 209 Summary" chapter.

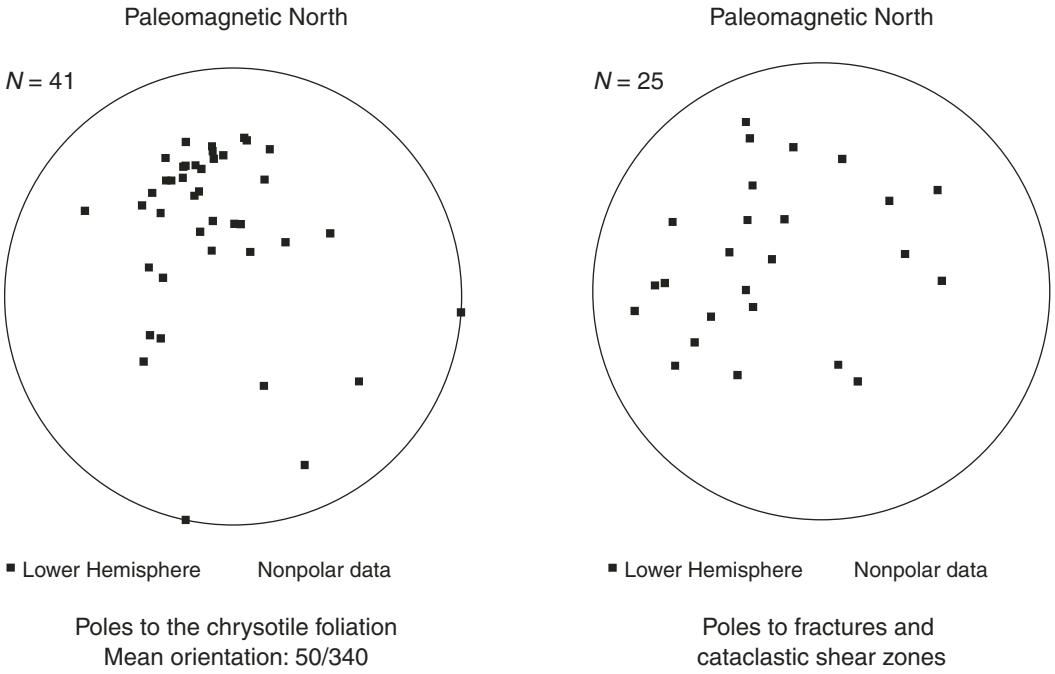

Figure F47. Close-up photograph of horizontally layered gouge overlying clast-rich gouge, which overlies a clast-poor nonlayered gouge (interval 209-1274A-23R-2, 42–58 cm).

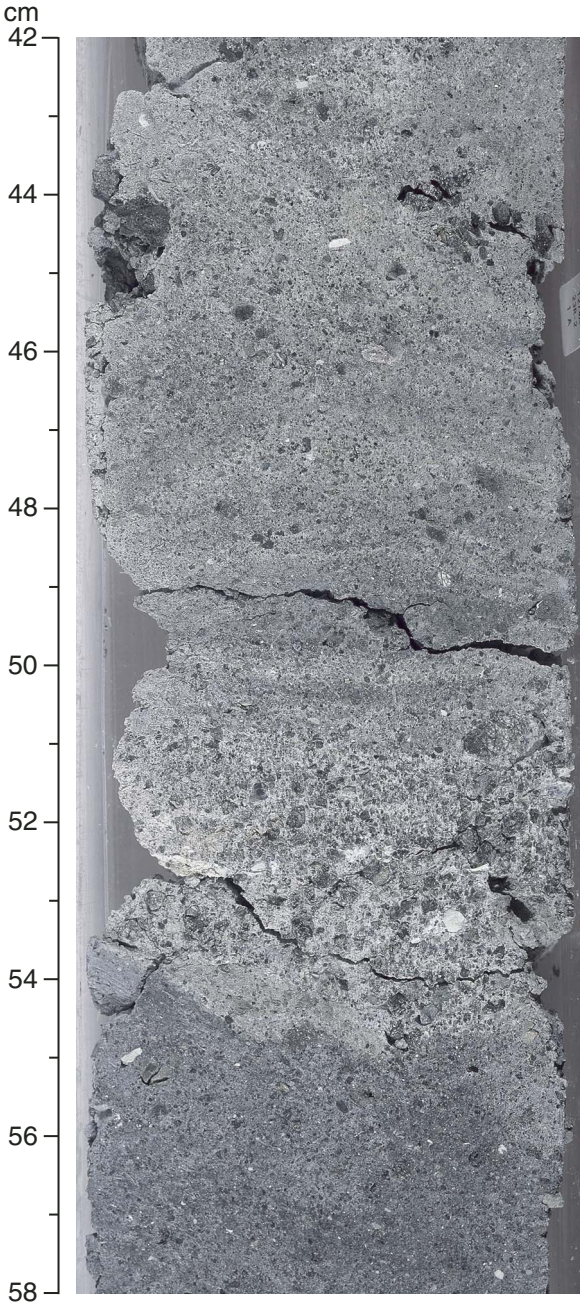

Figure F48. Close-up photograph of a fault gouge with irregular, steeply dipping layering (interval 209-1274A-24R-1, 24–52 cm).

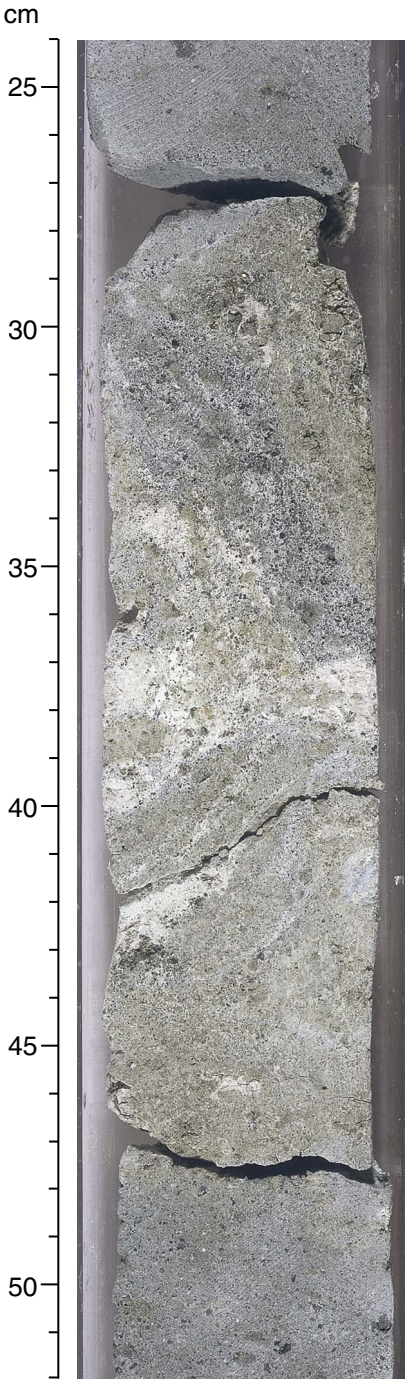

Figure F49. SiO_2 and H_2O vs. MgO for peridotites from Site 1274. Bulk rock compositions of Site 1268, 1270, 1271, and 1272 peridotites are shown for comparison. Also shown for comparison are end-member compositions for lizardite and talc (Deer et al., 1992).

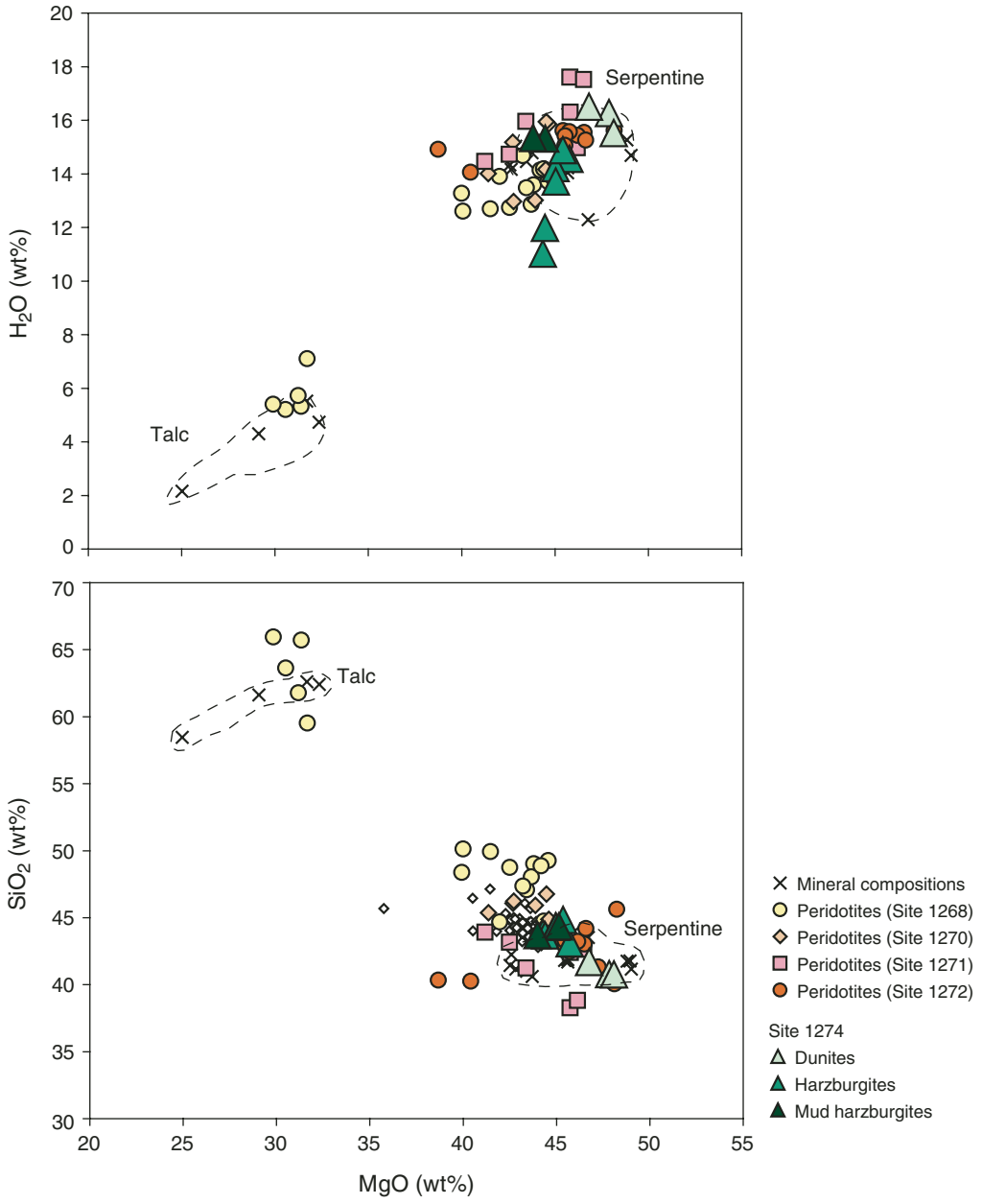

Figure F50. FeO vs. MgO whole-rock concentrations of Site 1274 peridotites (green triangle = harzburgite, light green triangles = dunite, dark green triangles = harzburgite mud). Published data and data from previous Leg 209 peridotites are shown for comparison: yellow circles = Site 1268, orange circles = Site 1272, pink diamonds = Site 1270, pink squares = Site 1271, open circles = Mid-Atlantic Ridge peridotites from Leg 109 Site 670 and Leg 153 Site 920. Published data are also shown for comparison: open diamonds = Mid-Atlantic Ridge peridotites from Leg 109 Site 670 (Hebert et al., 1990) and Leg 153 Site 920 (Casey, 1997). Other symbols: * = Southwest Indian Ridge (Snow and Dick, 1995), + = Izu-Bonin Mariana forearc peridotites (Parkinson and Pearce, 1998), diamond = East Pacific Rise peridotites (Niu and Hekinian, 1997), X = Western Alps orogenic lherzolites and ophiolites (Bodinier, 1988; Rampone et al., 1996), circle = Oman ophiolite harzburgites (Godard et al., 2000); triangle = Oman ophiolite mantle transition zone dunites (Godard et al., 2000). Whole-rock compositions are presented on a volatile-free basis assuming all Fe is FeO. The solid black lines show olivine and orthopyroxene composition as a function of Fe/Mg. Fine gray lines show constant values of Mg# (Mg# = 100 × molar Mg/[Mg + Fe_{total}]). Fe_{total} = total Fe as FeO.

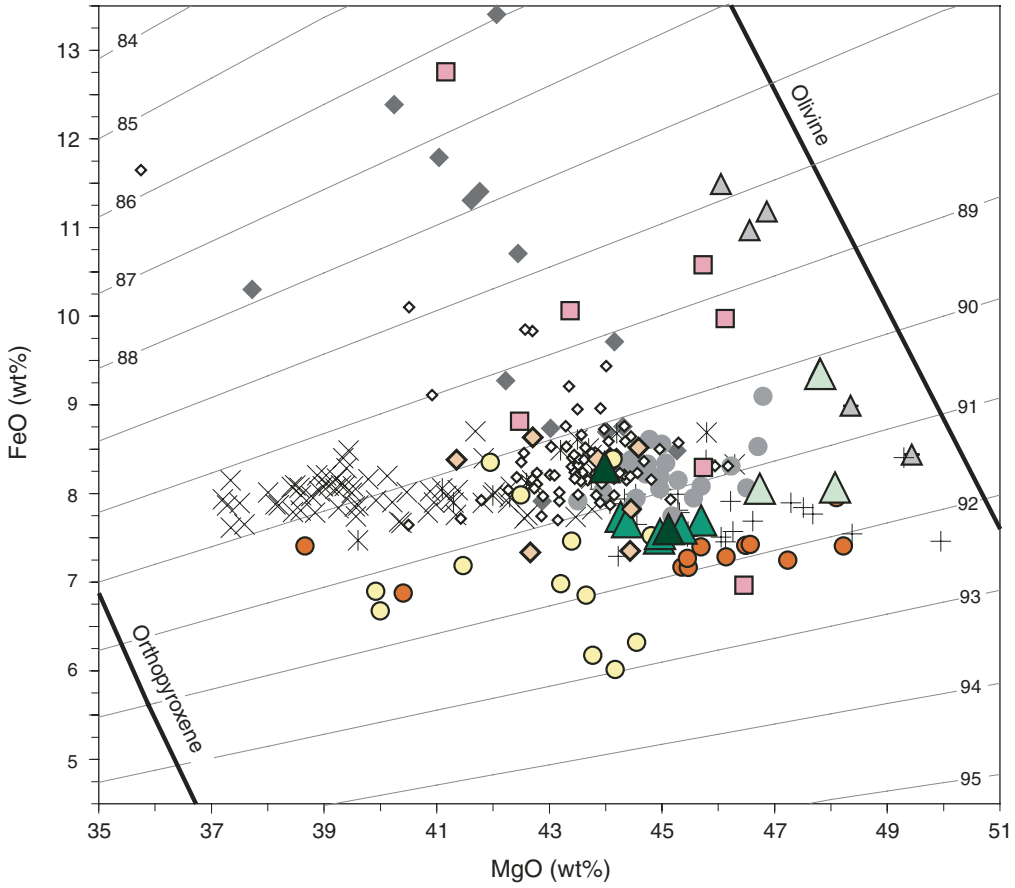

Figure F51. CaO vs. Al_2O_3 in peridotites from Site 1274. Site 1268, 1270, 1271, and 1272 peridotite compositions and published data on Leg 153 Site 920 peridotites (Casey, 1997) are shown for comparison.

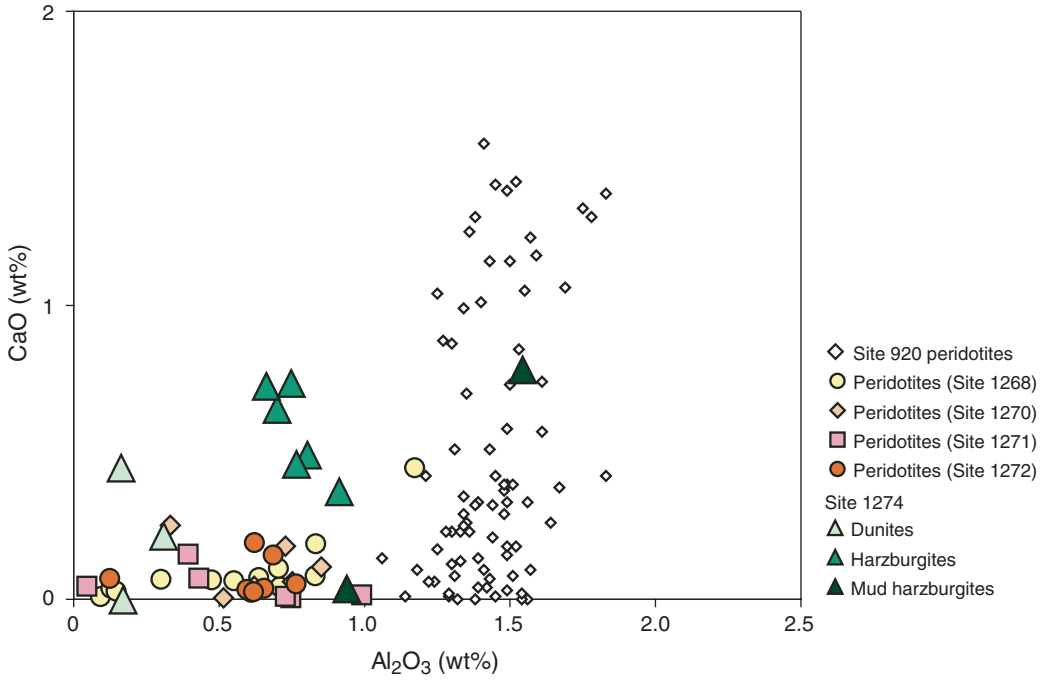

Figure F52. Cr, V, and Sc vs. Al_2O_3 for Site 1274 peridotites. Published data on Leg 153 Site 920 peridotites (Casey, 1997) are shown for comparison. Dashed line = detection limit (DL).

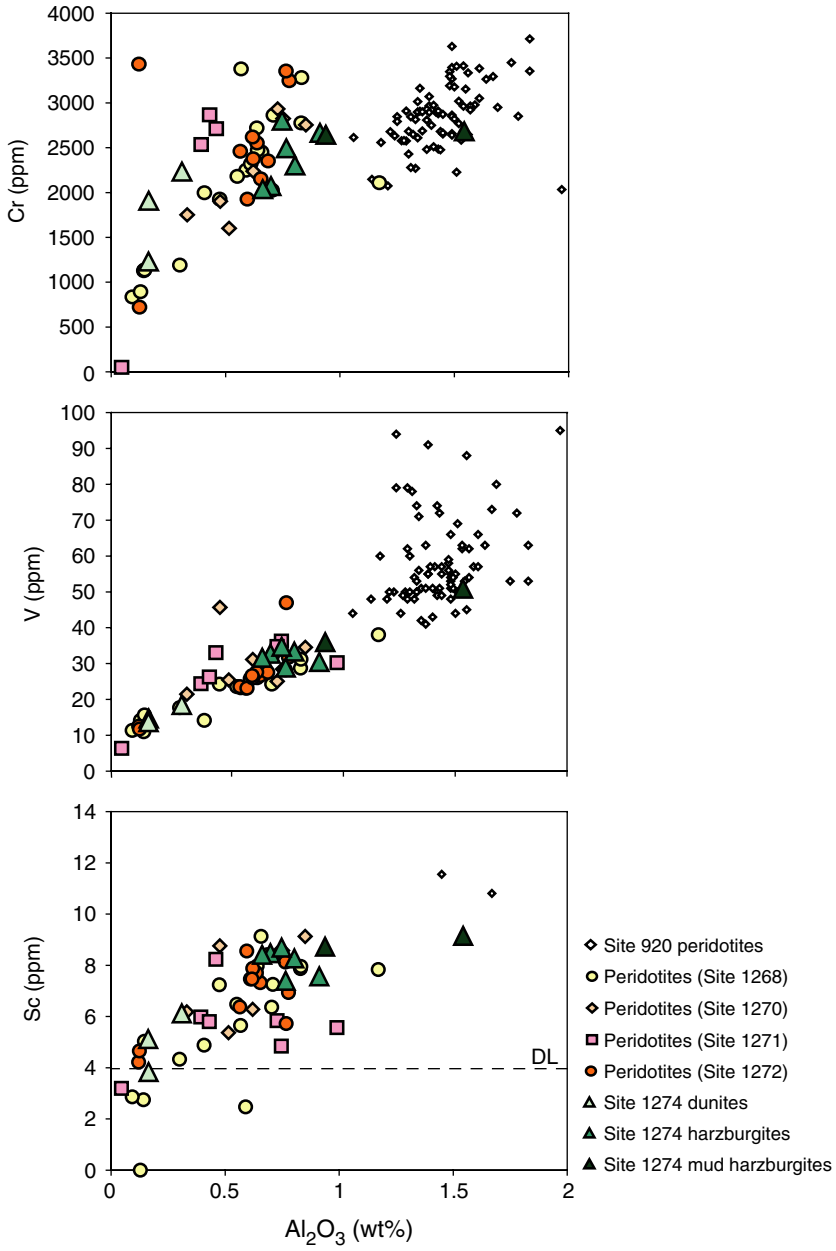

Figure F53. TiO_2 and Zr vs. Al_2O_3 in peridotites from Site 1274. Site 1268, 1270, 1271, and 1272 peridotite compositions and published data on Leg 153 Site 920 peridotites (Casey, 1997) are shown for comparison. Dashed line = detection limit (DL).

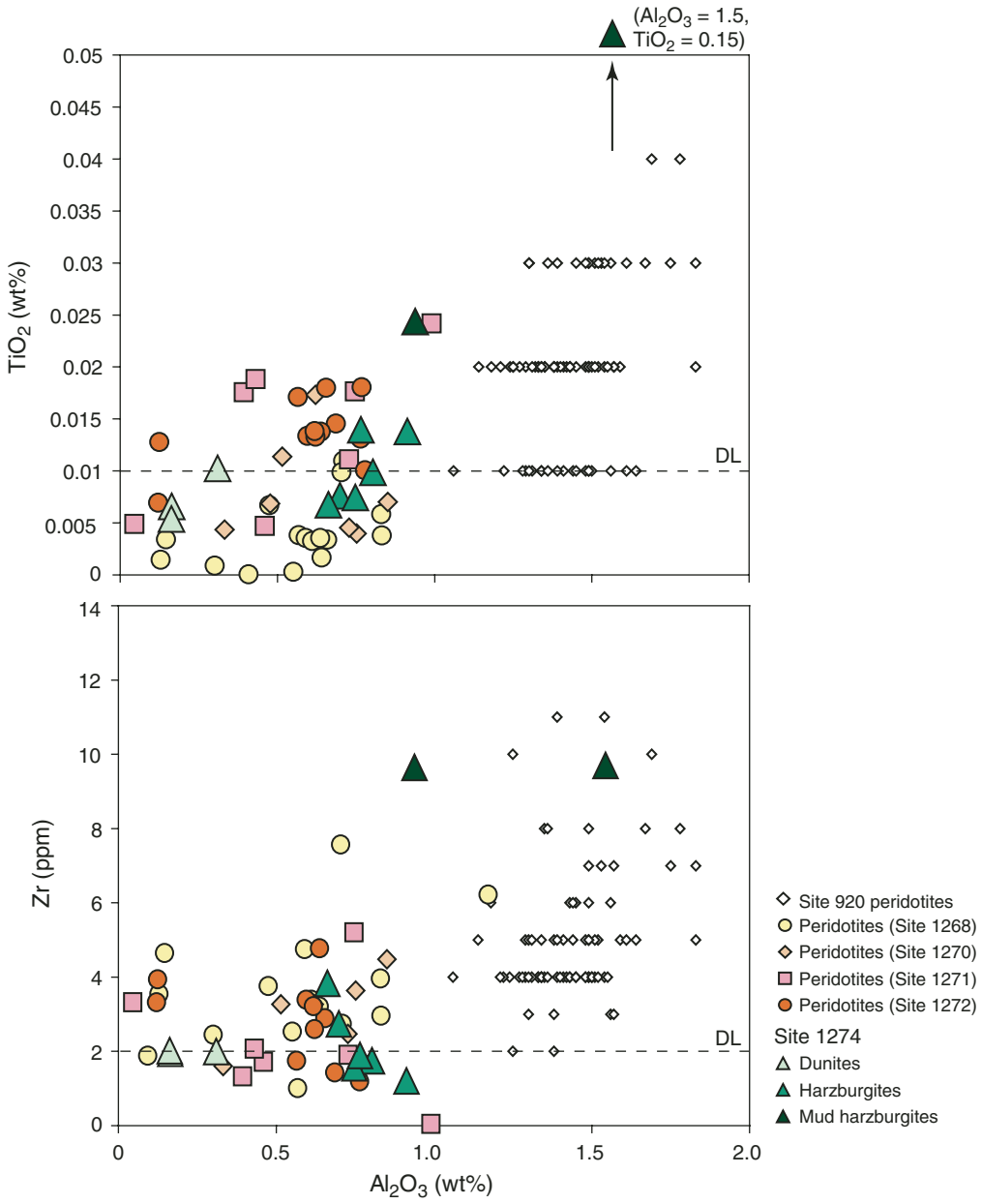

Figure F54. MgO/SiO_2 vs. Al_2O_3/SiO_2 for Site 1274 peridotites. Site 1268, 1270, 1271, and 1272 peridotites are shown for comparison. Also shown for comparison are published data on ophiolitic and orogenic peridotites (Western Alps orogenic lherzolites and ophiolites [Bodinier, 1988; Rampone et al., 1996); Oman dunites and harzburgites [Godard et al., 2000]) and abyssal peridotites (Southwest Indian Ridge [SWIR] [Snow and Dick, 1995]; Mid-Atlantic Ridge [MAR] Site 920 [Casey, 1997]; East Pacific Rise [EPR] [Niu and Hekinian, 1997]; Izu-Bonin Mariana [IBM] [Parkinson and Pearce, 1998]).

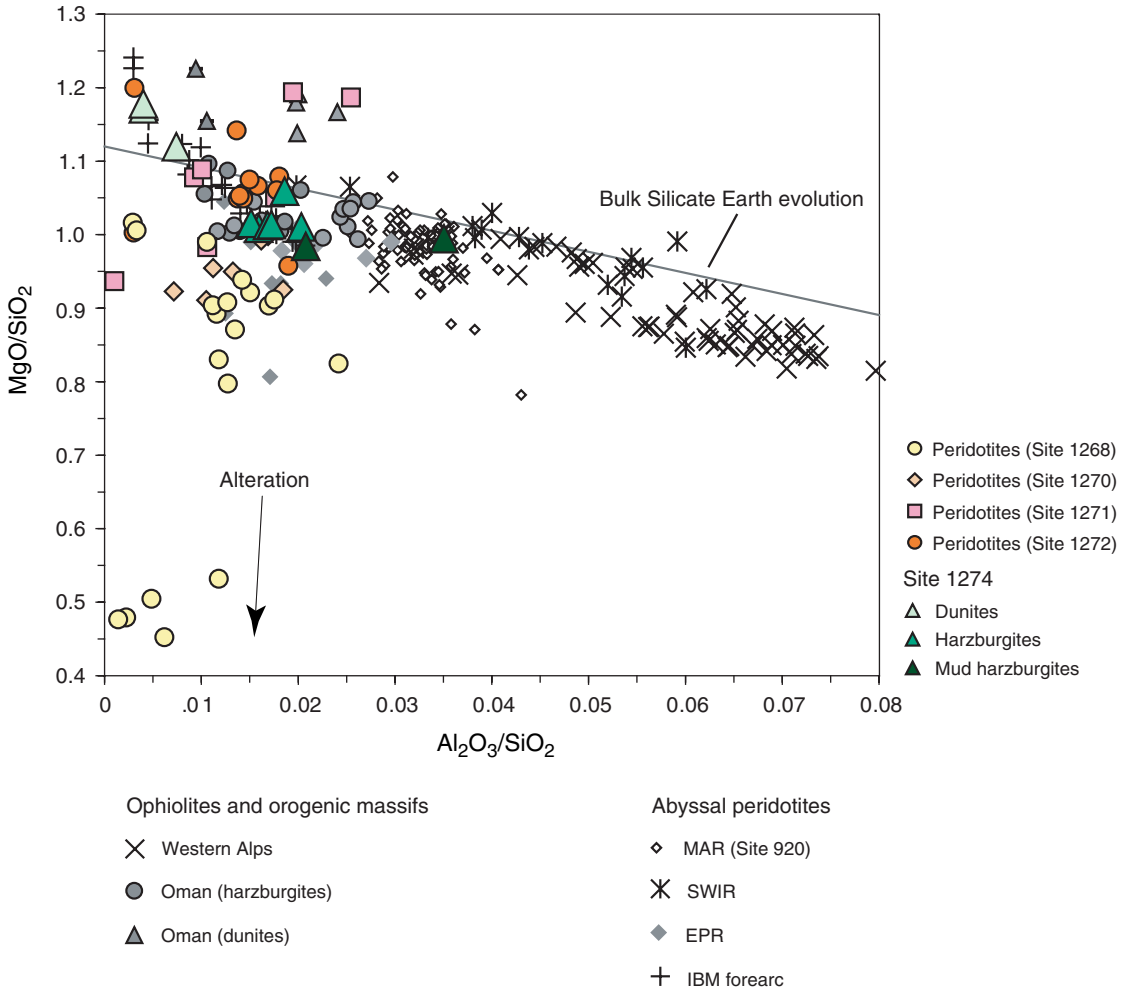

Figure F55. Thermal conductivity, bulk density, *P*-wave velocity, apparent *P*-wave anisotropy, and porosity in peridotites recovered from Hole 1274A. The numbers 0, 1, and 2 in the legend of the thermal conductivity graph refer to the probe needle orientation with the respect of the core axis (0= parallel to the core axis, 1 and 2 = oblique to the core axis), as shown in Figure F11, p. 53, in the "Explanatory Notes" chapter. TD = total depth.

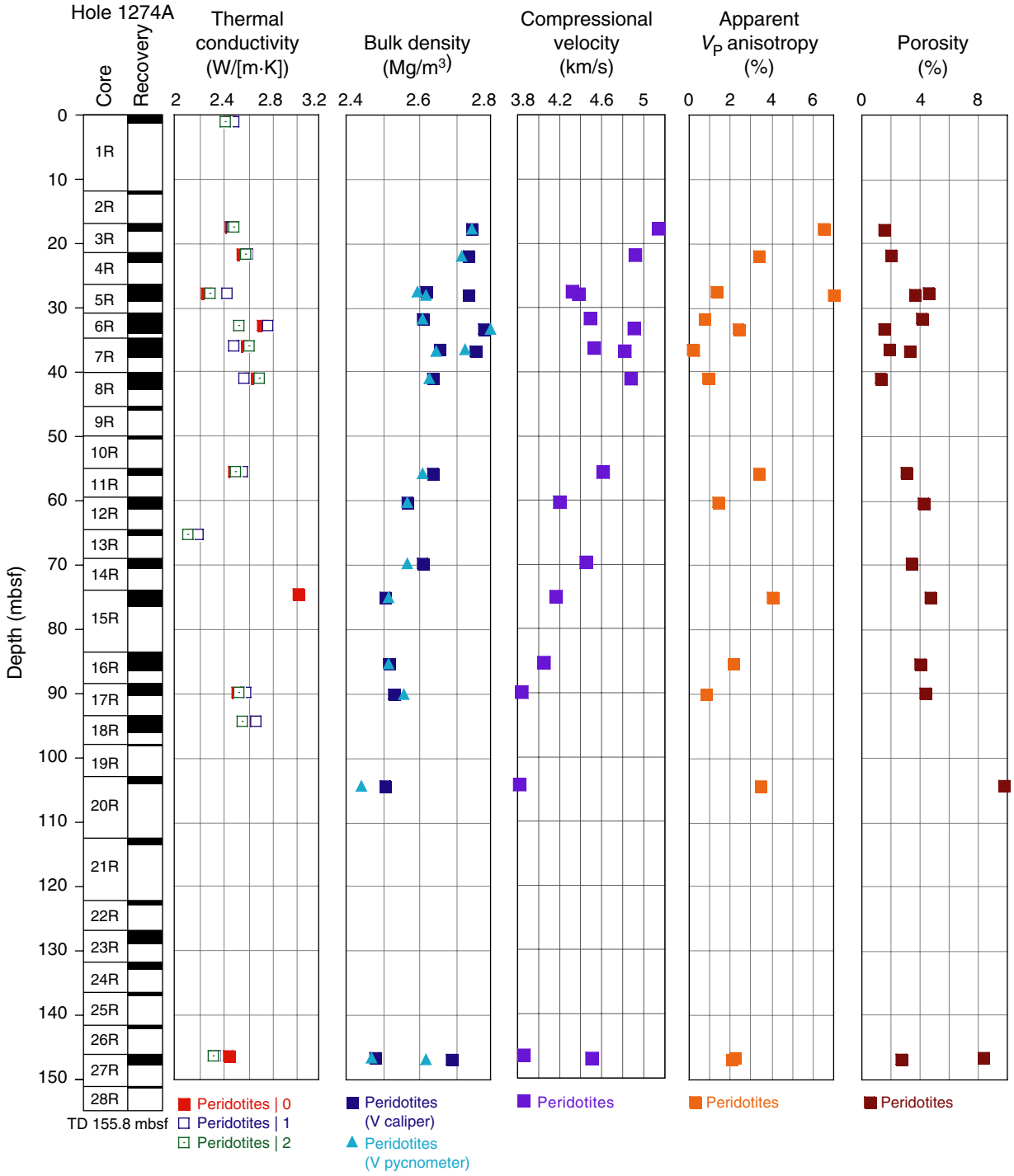

Figure F56. Magnetic susceptibility and natural gamma ray emission (NGR) of cores from Hole 1274A, measured on the MST. TD = total depth.

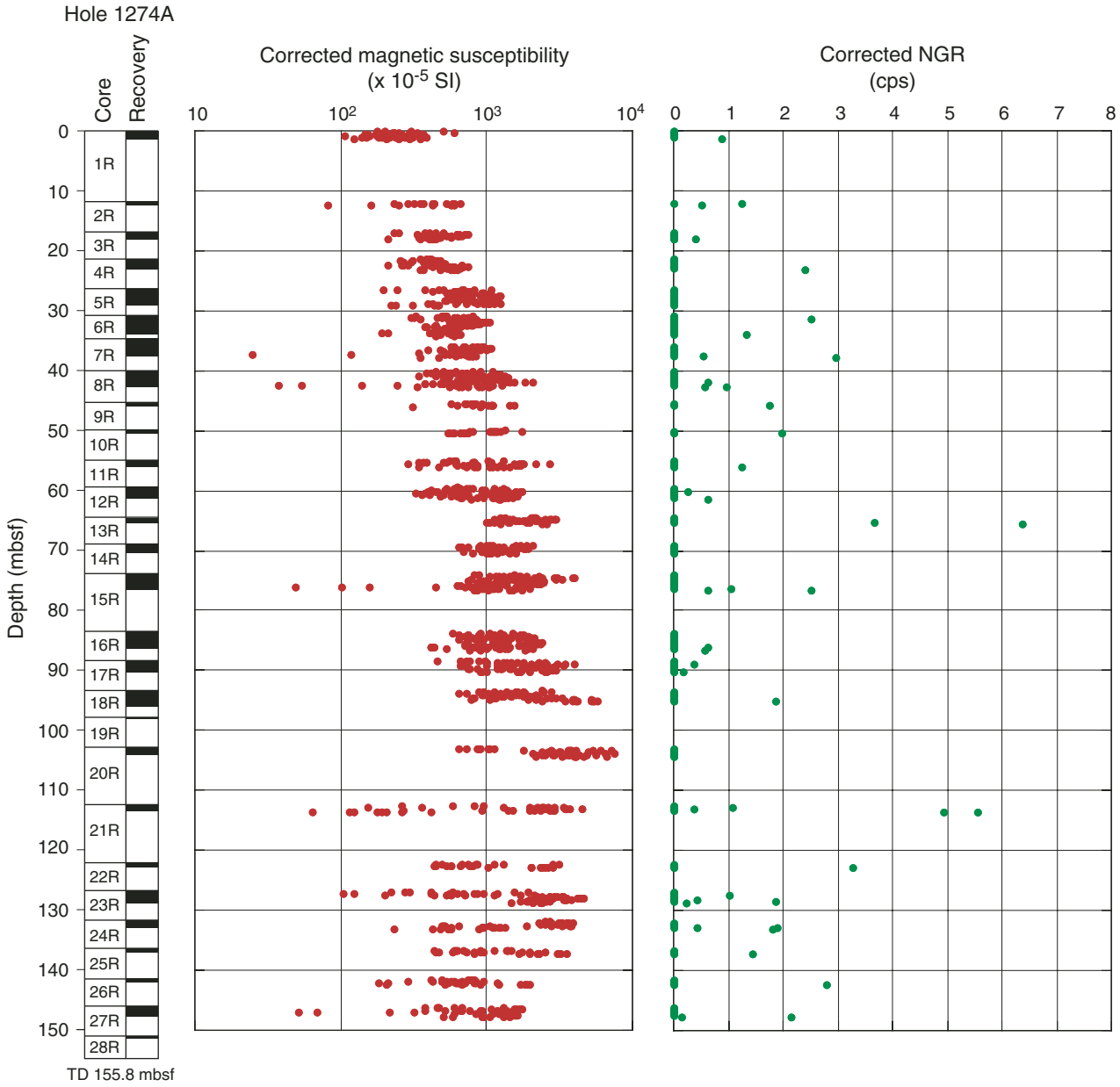

Figure F57. Thermal conductivity of peridotite samples from Site 1274, compared with values from Sites 1268, 1270, 1271, and 1272, and from Legs 147 (Gillis, Mével, Allan et al., 1993) and 153 (Cannat, Karson, Miller et al., 1995).

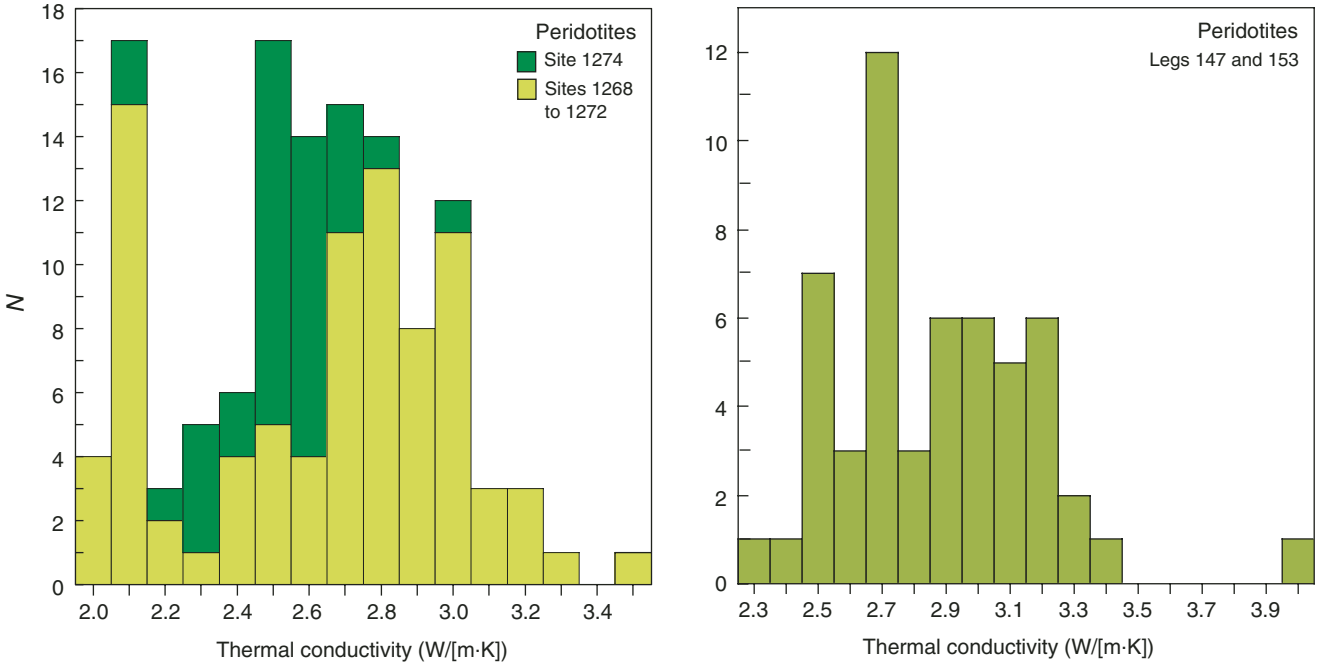

Figure F58. Thermal conductivity anisotropy in peridotite samples from Sites 1268, 1270, 1271, 1272, and 1274.

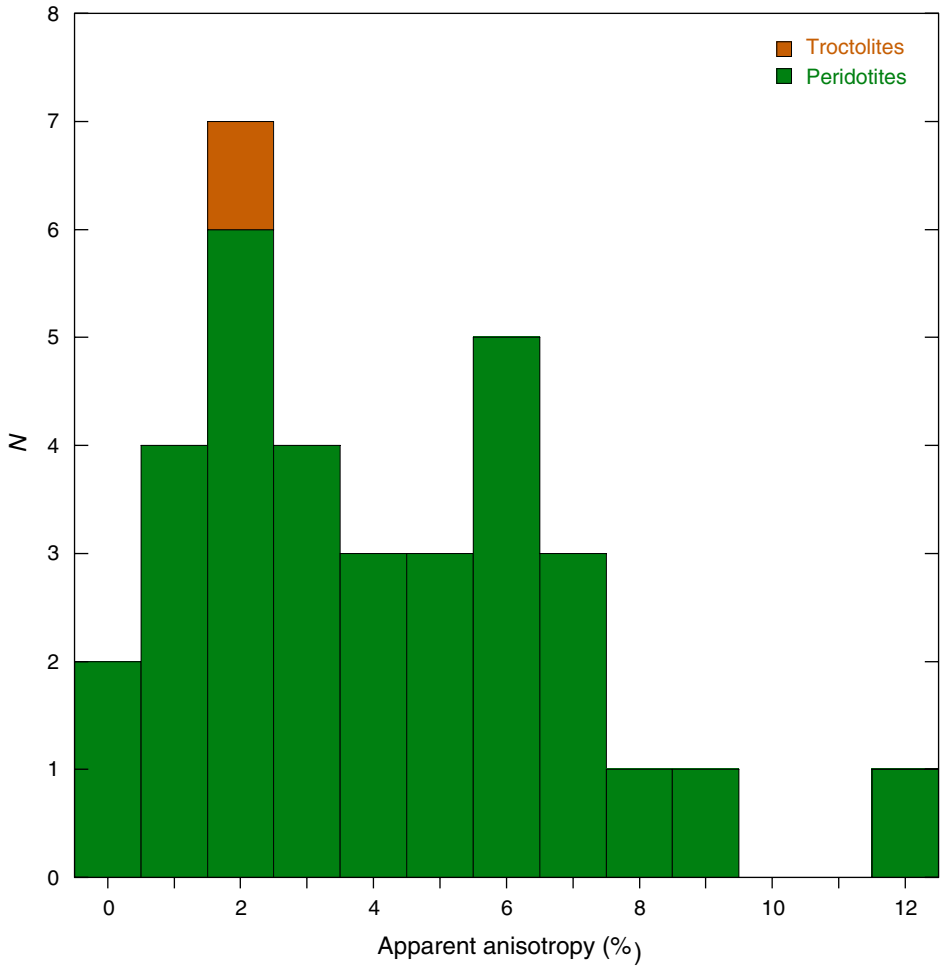

Figure F59. Thermal conductivity (mean of the three measured values for each sample) vs. bulk density in samples from Sites 1268, 1270, 1271,1272, and 1274. The reference data are from Clark (1966) and Clauser and Huenges (1995).

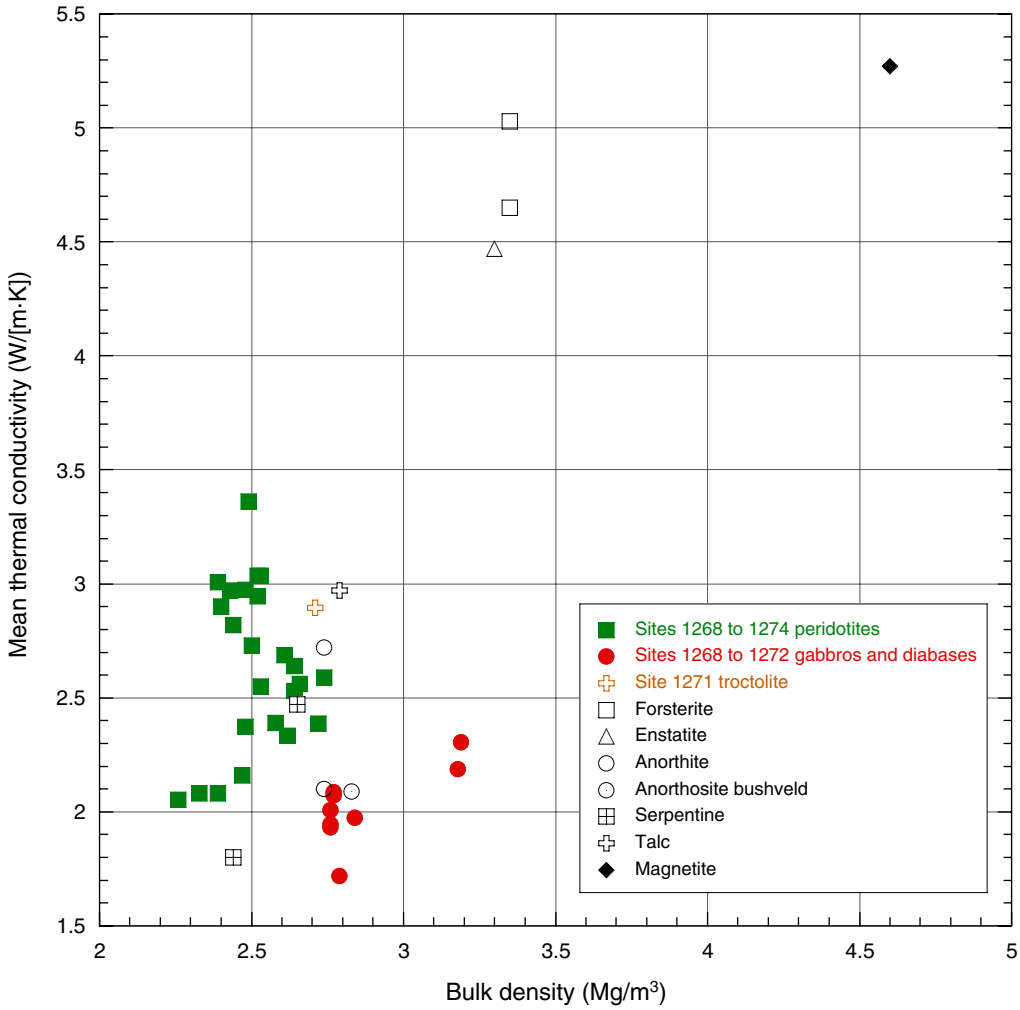

Figure F60. *P*-wave velocity vs. wet bulk density in samples from Site 1274, compared with data from Legs 147 (Gillis, Mével, Allan et al., 1993; Iturrino et al., 1996) and 153 (Cannat, Karson, Miller, et al., 1995; Miller and Christensen, 1997), as well as Sites 1268, 1270, 1271, and 1272.

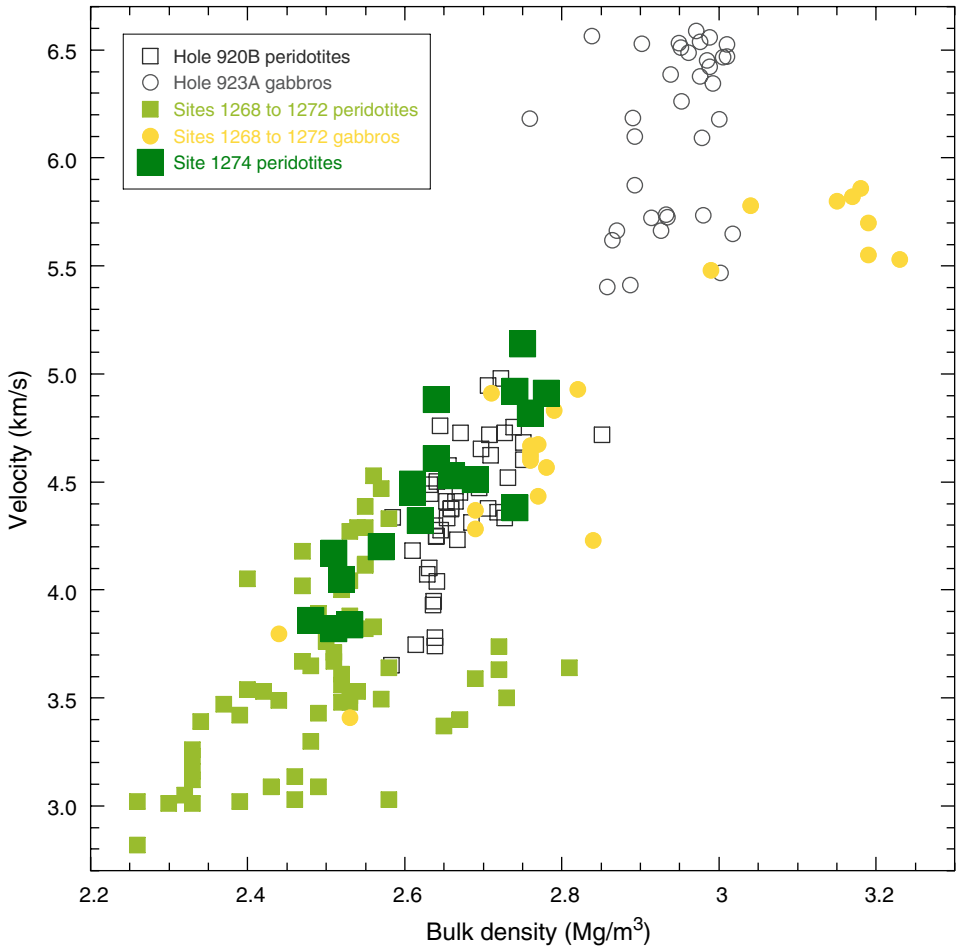

Figure F61. Archive-half magnetic measurements from Hole 1274A. From left: volume magnetic susceptibility; natural remanent magnetization (NRM) intensity (open red circles) and the remanence after 20-mT demagnetization (solid gray circles); NRM inclination and the remanence at 20 mT (same symbols as for intensity); and percentage of the NRM intensity remaining at 20 mT. Remanence and susceptibility data from within 4 cm of a piece end have been excluded. TD = total depth.

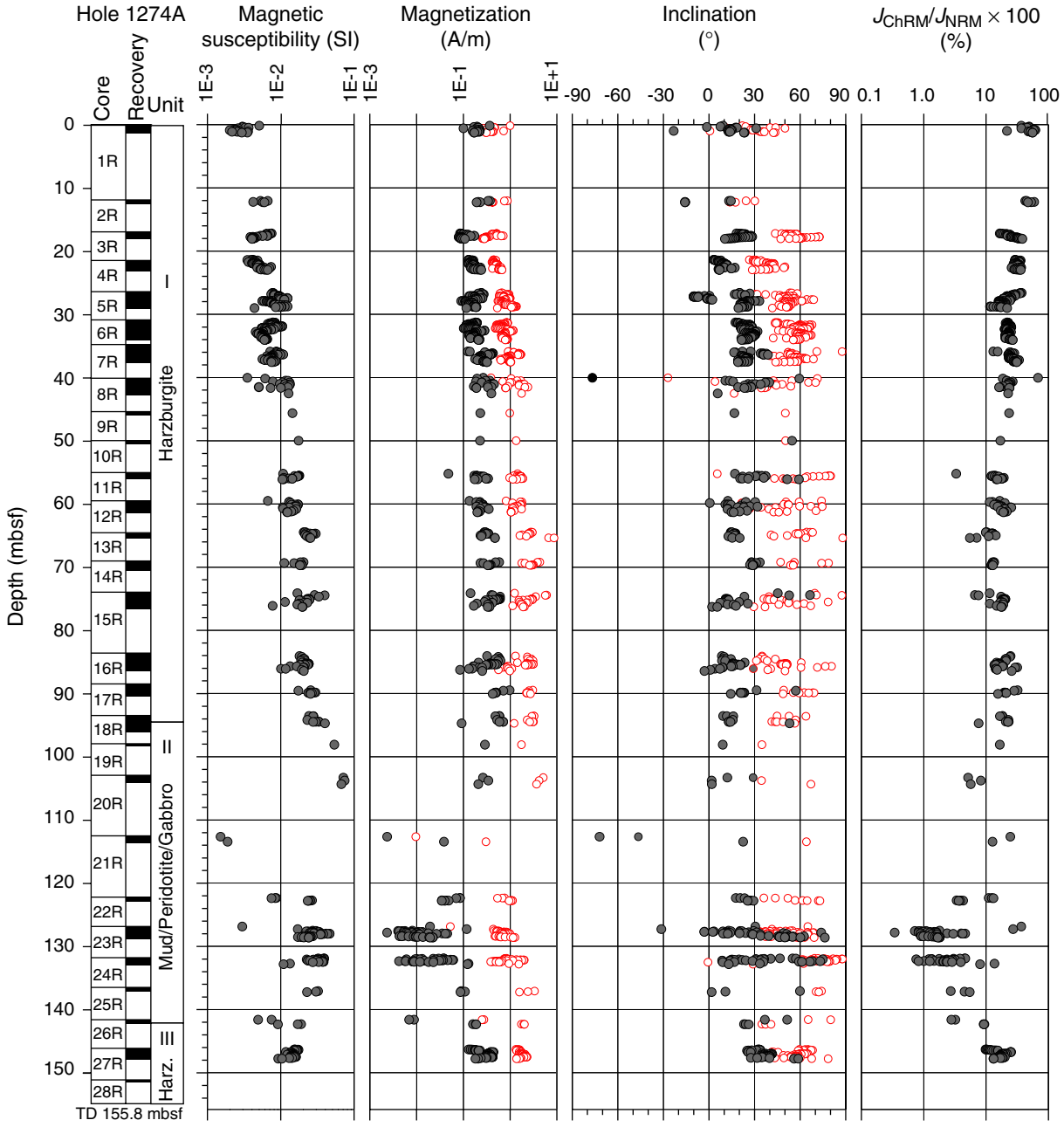

Figure F62. Representative vector endpoint diagrams for archive-half measurements and (D–F) discrete samples from Hole 1274A. **A.** Section 209-1274A-3R-1, 88 cm. **B.** Section 209-1274A-5R-1, 124 cm. **C.** Section 209-1274A-8R-1, 106 cm. **D.** Sample 209-1274A-3R-1, 89–91. **E.** Sample 209-1274A-5R-1, 125–127 cm. **F.** Sample 209-1274A-8R-1, 106–108 cm. NRM = natural remanent magnetization. Open circles = projections of the remanence onto the vertical plane, solid circles = projections of the remanence onto the horizontal plane.

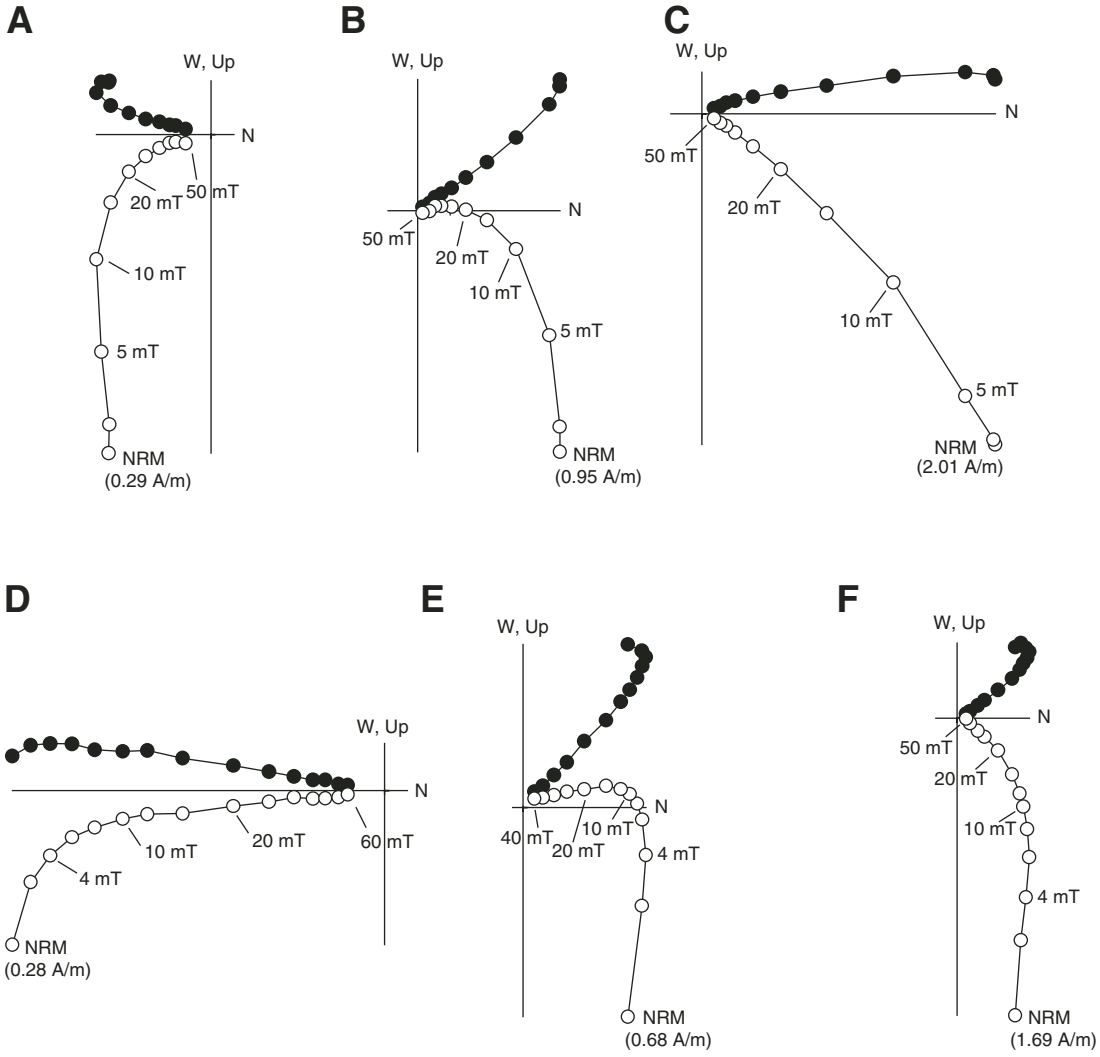

Figure F63. Anisotropy of magnetic susceptibility (AMS; left) and anisotropy of anhysteretic remanence (AARM; right) results for discrete samples from Hole 1274A. The Flinn-type diagrams (top) illustrate the shape and degree of anisotropy. Int./min. = intermediate/minimum eigenvalue ratio. Max./int. = maximum/intermediate eigenvalue ratio. Line separates fields for oblate (below line) and prolate (above line) fabrics. Lower plots show equal-area (lower hemisphere) projections of the AMS (left) and AARM (right) eigenvectors. Circles = eigenvector associated with the minimum eigenvalue. Squares = eigenvector associated with the maximum eigenvalue. For the AARM anisotropy plot, lighter circles = samples where the fabric is statistically prolate and lighter squares indicate samples with statistically oblate fabrics.

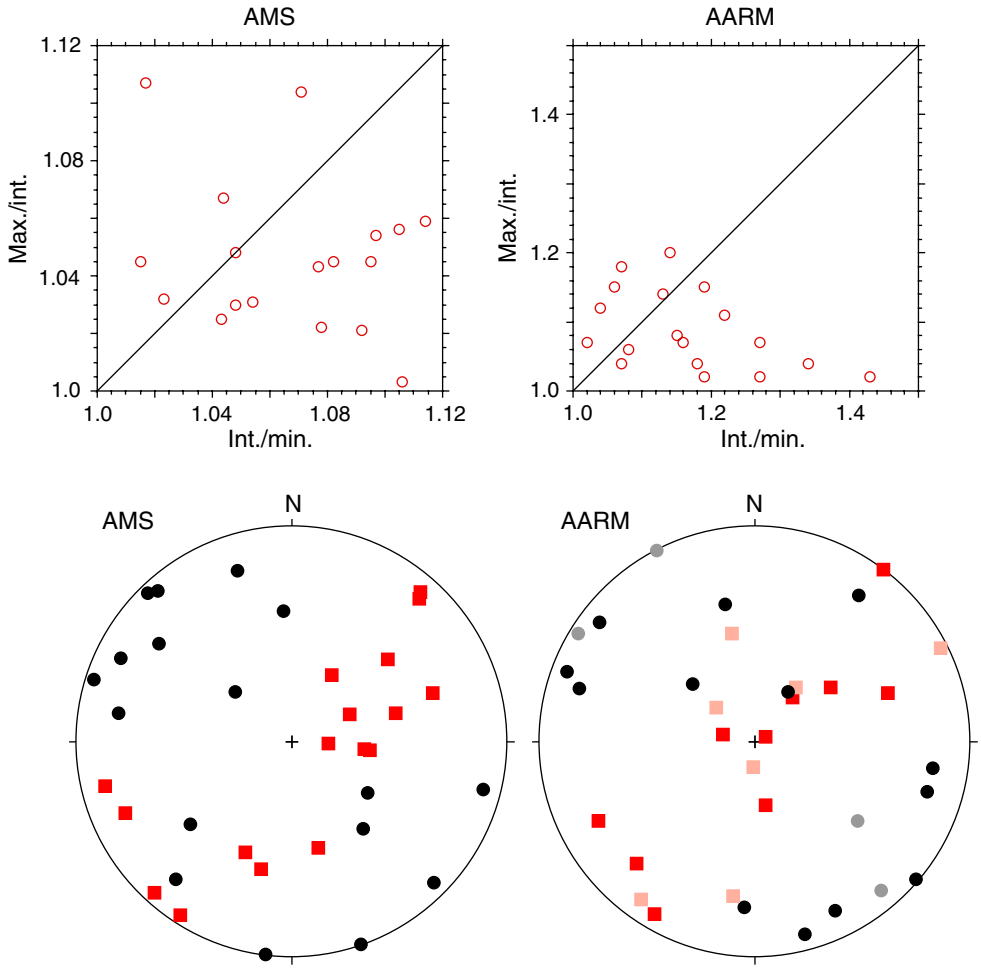

Figure F64. Histograms of (**A**) inclinations and (**B**) declinations for discrete samples (black bars) and archive halves (gray) from Hole 1274A.

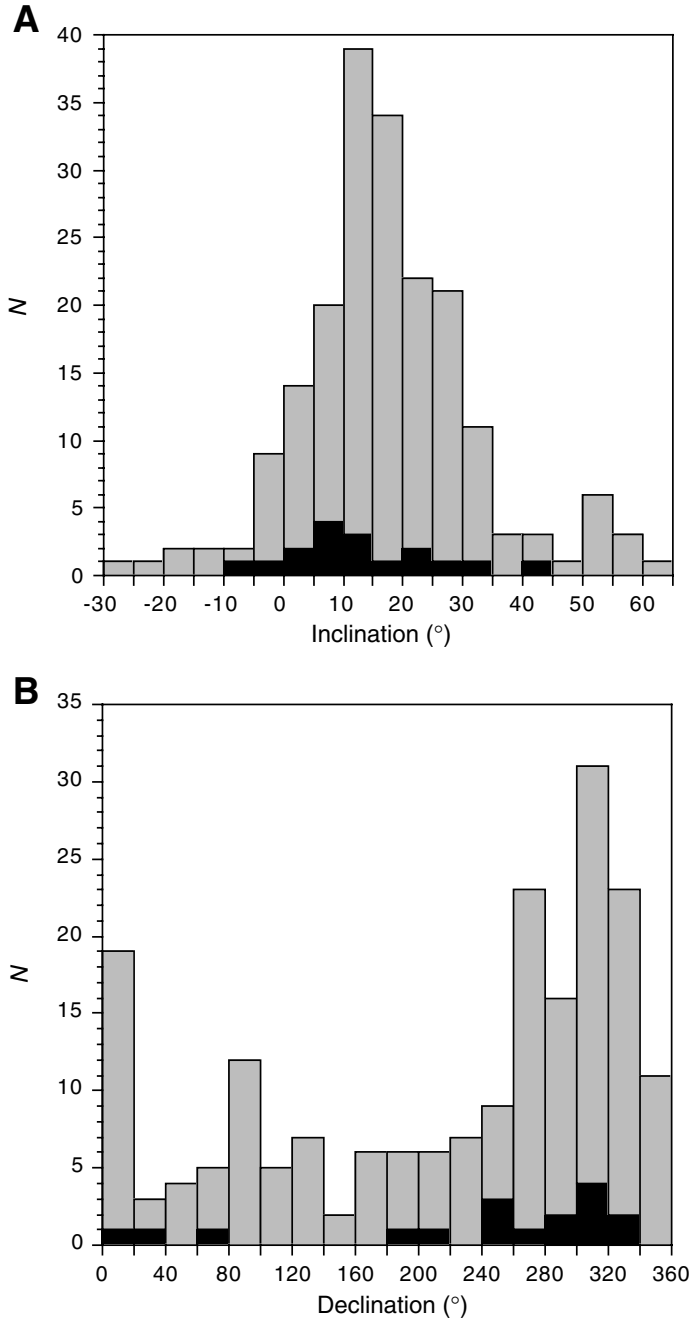

Figure F65. Downhole variation of characteristic remanence directions from archive halves and discrete samples. Note that many of the steepest positive inclinations are associated with core pieces <10 cm in length (small open circles). TD = total depth.

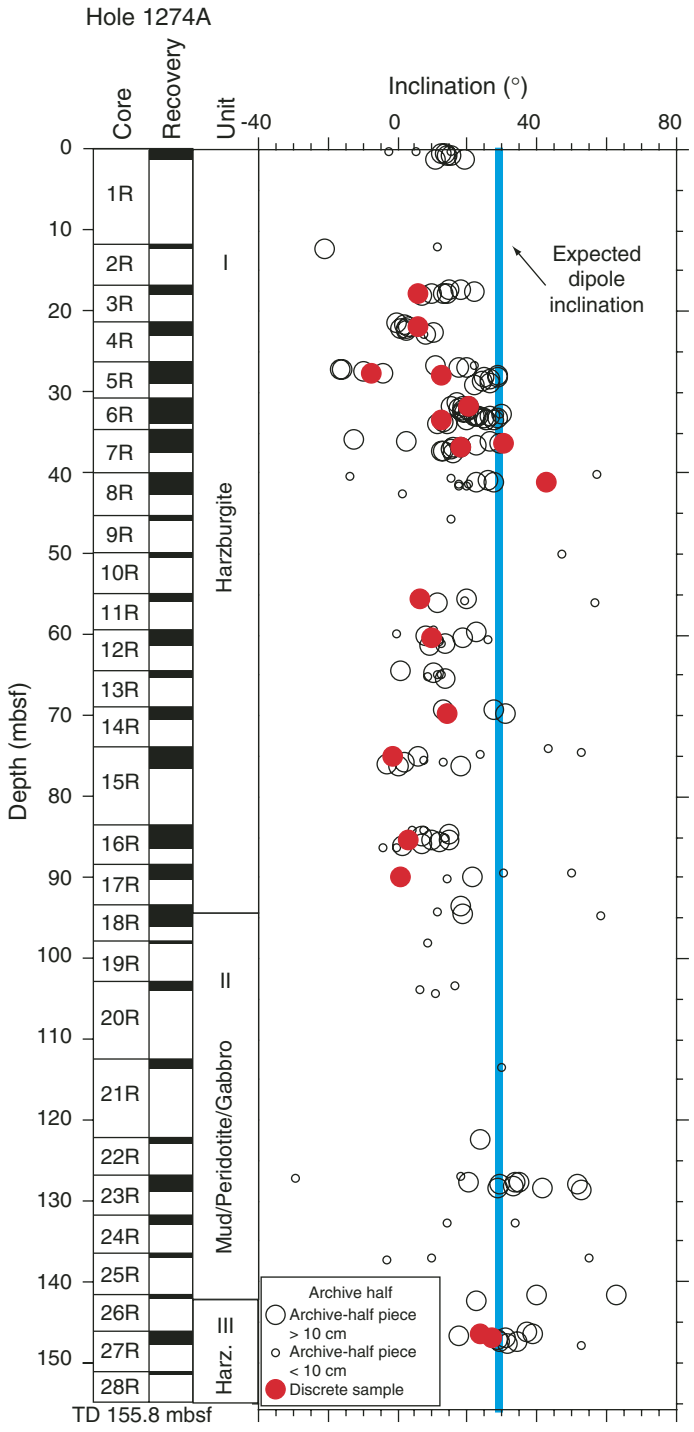

Figure F66. Temperature of ocean bottom water measured during the WSTP deployment prior to the beginning of drilling operations in Hole 1274A. **A.** Entire temperature time series showing the temperature response of the WSTP prior to, during, and after the deployment. **B.** Expanded section of the temperature changes while the WSTP was lowered to a depth of 2 m above seafloor. This profile shows the rising temperatures prior to collection of a water sample, the time when the water-sampling valve opened (VO), the time when the valve closed (VC), and a thermal anomaly after the valve closed. A linear fit to the temperature time-series data before the water-sampling valve opened is also shown.

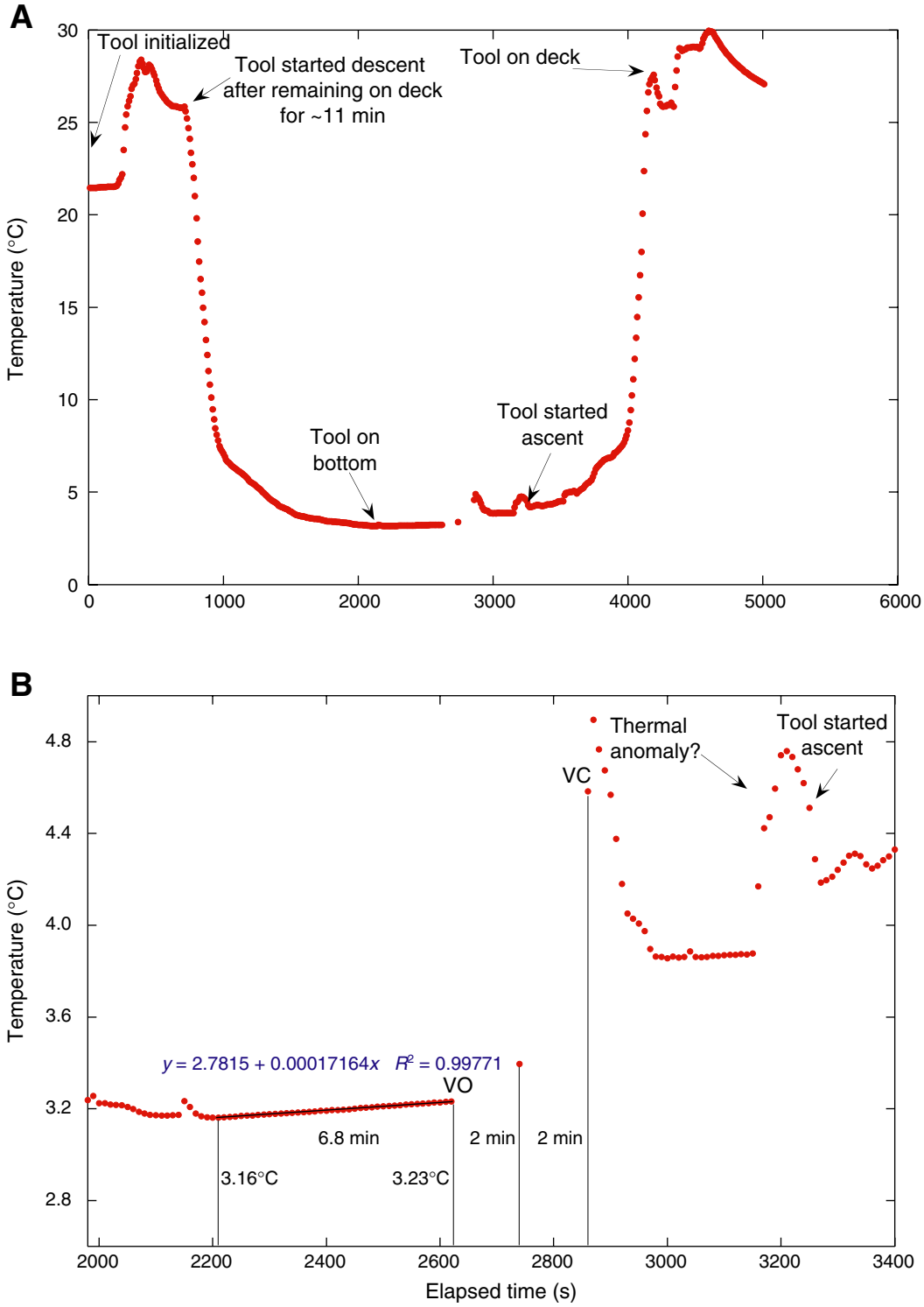

Table T1. Coring summary, Site 1274.

Hole 1274A
Latitude: 15°38.8669′N
Longitude: 46° 40.5824′W
Time on site: 93.25 (0030 hr, 15 Jun–2145 hr, 18 Jun 2003)
Seafloor (drill pipe measurement from rig floor, mbrf): 3951.0
Distance between rig floor and sea level (m): 11.2
Water depth (drill pipe measurement from sea level, m): 3939.8
Total depth (drill pipe measurement from rig floor, mbrf): 4106.8
Total penetration (meters below seafloor, mbsf): 155.8
Total length of drilled intervals (m): 0.0
Total core recovered (m): 34.65
Core recovery (%): 22.2
Total number of cores: 28

Core	Date (Jun 2003)	Local time (hr)	Depth (mbsf) Top	Depth (mbsf) Bottom	Length (m) Cored	Length (m) Recovered	Recovery (%)	Remarks
209-1274A-								
								WSTP before spudding
1R	15	1450	0.0	11.9	11.9	1.10	9.2	AHC
2R	15	1635	11.9	16.9	5.0	0.41	8.2	AHC
3R	15	1930	16.9	21.3	4.4	1.15	26.1	
4R	15	2300	21.3	26.3	5.0	1.70	34.0	AHC
5R	16	0205	26.3	30.8	4.5	2.52	56.0	
6R	16	0555	30.8	35.8	5.0	3.00	60.0	
7R	16	0845	35.8	40.0	4.2	1.75	41.7	
8R	16	1105	40.0	45.3	5.3	2.05	38.7	Whirl-Pak
9R	16	1305	45.3	49.9	4.6	0.55	12.0	Whirl-Pak
10R	16	1450	49.9	54.9	5.0	0.48	9.6	
11R	16	1635	54.9	59.4	4.5	0.98	21.8	Dropped deplugger
12R	16	2225	59.4	64.4	5.0	1.42	28.4	
13R	17	0030	64.4	69.0	4.6	0.90	19.6	
14R	17	0305	69.0	74.0	5.0	1.36	27.2	
15R	17	0615	74.0	83.7	9.7	1.94	20.0	Whirl-Pak
16R	17	0835	83.7	88.3	4.6	2.19	47.6	Whirl-Pak
17R	17	1030	88.3	93.3	5.0	1.35	27.0	
18R	17	1240	93.3	97.9	4.6	1.38	30.0	
19R	17	1415	97.9	102.9	5.0	0.20	4.0	
20R	17	1700	102.9	112.5	9.6	1.09	11.4	
21R	17	1945	112.5	122.1	9.6	0.67	7.0	
22R	17	2240	122.1	126.8	4.7	0.65	13.8	
23R	18	0040	126.8	131.8	5.0	1.68	33.6	
24R	18	0220	131.8	136.5	4.7	1.10	23.4	AHC
25R	18	0405	136.5	141.5	5.0	0.52	10.4	AHC
26R	18	0600	141.5	146.1	4.6	0.70	15.2	
27R	18	0820	146.1	151.1	5.0	1.50	30.0	AHC; Whirl-Pak
28R	18	1130	151.1	155.8	4.7	0.31	6.6	AHC; Whirl-Pak
				Cored totals:	155.8	34.65	22.2	

Notes: WSTP = Water Sampling Temperature Probe. AHC = active heave compensation.

Table T2. XRD results, Hole 1274A.

Core, section, interval (cm)	Depth (mbsf)	Piece	Rock type	Mineralogy			ICP-AES analyses	Thin section
				Major	Minor	Trace		
209-1274A-								
3R-1, 87–89	17.8	9B	Harzburgite	Lizardite	Olivine	Opx, brucite, magnetite	Yes	Yes
5R-1, 121–125	27.5	10B	Harzburgite	Lizardite		Brucite, opx	Yes	Yes
7R-1, 48–54	36.3	5	Harzburgite	Lizardite	Olivine, opx	Brucite	Yes	Yes
8R-1, 108–111	41.1	15C	Dunite	Lizardite	Olivine, brucite	Magnetite	Yes	Yes
11R-1, 75–79	55.7	12B	Harzburgite	Lizardite	Brucite, opx	Olivine	Yes	Yes
15R-1, 101–104	75.0	15	Dunite	Lizardite	Brucite	Opx	Yes	Yes
17R-2, 16–19	89.9	1B	Harzburgite	Lizardite	Opx		Yes	Yes
18R-2, 6–13	94.9	3	Fault	Lizardite			—	—
20R-1, 141–144	104.3	26	Dunite	Lizardite	Brucite	Magnetite	Yes	Yes
23R-2, 0–3	127.5	1	Gray mud	Lizardite		Magnetite	Yes	—
23R-2, 67–70	128.1	1	Black mud	Lizardite	Nontronite	Magnetite	Yes	—
27R-1, 78–83	146.9	7	Harzburgite	Lizardite	Olivine	Opx, magnetite	Yes	Yes

Notes: Opx = orthopyroxene. Due to peak overlap, samples with identified lizardite may also contain chrysotile. Peaks for magnetite and chromite are indistinguishable. Qualifiers "major, minor, and trace" indicate relative abundances based on peak heights and do not necessarily reflect true relative proportions. ICP-AES = inductively coupled plasma–atomic emission spectrometry. ICP-AES data are available in Table **T5,** p. 106. This table is also available in **ASCII.**

Table T3. Vein mineralogy, Hole 1274A.

Hole	1274A
Penetration depth (mbsf)	155.8
Recovery (%)	22.2
Length recovered (m)	34.7
Volume recovered (cm^3)	86,874
Veins in hole (cm^3/m)	40.6
Veins in hole (%)	1.8
Vein minerals in hole (cm^3/m):	
Picrolite	14.42
Chrysotile	20.98
Magnetite	0.42
Carbonates	4.60
Others	0.16
Vein minerals in hole (%):	
Picrolite	0.58
Chrysotile	0.84
Magnetite	0.02
Carbonates	0.18
Others	0.01
Vein minerals in veins (%):	
Picrolite	35.5
Chrysotile	51.7
Magnetite	1.0
Carbonates	11.3
Others	0.4

Notes: The volume of veins is based on macroscopic observations of vein mineralogy and estimates of vein percentages by pieces. We computed volume percentage of veins by using the volume weighted average of the macroscopic estimates using the relative curated length and assuming a constant core radius throughout the site. This table is also available in **ASCII.**

Table T4. Crystal-plastic deformation intensities, Hole 1274A.

Lithology	Total length of core (cm)	Percent of core	*N*	Average CPf	Total core showing deformation grade (cm)								
					0.0	0.5	1.0	1.5	2.0	2.5	3.0	3.5	4.0
Harzburgite	2792.2	82.6	329.0	0.3	961.7	1714.5	95.0	2.5	8.0	0.0	0.0	0.0	2.5
Dunite	400.5	11.8	88.0	0.0	394.5	6.0	0.0	0.0	0.0	0.0	0.0	0.0	0.0
Orthopyroxene dunite	130.5	3.9	26.0	0.4	22.0	103.5	5.0	0.0	0.0	0.0	0.0	0.0	0.0
Gabbro	58.5	1.7	15.0	0.5	33.5	14.0	3.0	0.0	8.0	0.0	0.0	0.0	0.0
Total	3381.7		458.0	0.3	1411.7	1838.0	103.0	2.5	16.0	0.0	0.0	0.0	2.5
Percent of total	99.8				41.7	54.4	3.0	0.1	0.5	0.0	0.0	0.0	0.1

Notes: CPf = crystal-plastic deformation intensity index (0 = no deformation through 5 = extreme deformation). *N* = number of measurements. This table is also available in **ASCII.**

Table T5. Major and trace element compositions of rocks, Hole 1274A.

Core, section, interval (cm)	Depth (mbsf)	Piece	Unit	Lithology	Major element oxides (wt%)										LOI	Volatiles (wt%)	
					SiO_2	TiO_2	Al_2O_3	Fe_2O_3	MgO	MnO	CaO	Na_2O	K_2O	Total		CO_2	H_2O
209-1274A-																	
3R-1, 87–89	17.77	9B	I	Harzburgite	43.92	0.01	0.70	8.57	44.31	0.13	0.65	<0.03	<0.01	98.31	10.44	0.34	10.99
5R-1, 121–125	27.51	10B	I	Harzburgite	43.18	0.01	0.80	8.53	45.74	0.12	0.49	0.04	<0.01	98.90	12.14	0.35	14.52
7R-1, 48–54	36.28	5	I	Harzburgite	43.75	0.01	0.66	8.51	44.42	0.12	0.72	<0.03	<0.01	98.22	10.19	0.37	11.95
8R-1, 108–111	41.08	15C	I	Dunite	40.85	0.01	0.16	8.94	48.11	0.12	0.45	<0.03	0.01	98.66	13.72	0.36	15.49
11R-1, 75–79	55.65	12B	I	Harzburgite	44.44	0.01	0.75	8.30	44.99	0.12	0.73	<0.03	<0.01	99.37	12.69	0.40	14.18
15R-1, 101–104	75.01	15	I	Dunite	41.78	0.01	0.31	8.93	46.78	0.12	0.21	0.03	<0.01	98.17	15.47	0.38	16.47
17R-2, 16–19	89.91	1B	I	Harzburgite	44.91	0.01	0.91	8.43	45.39	0.12	0.37	0.03	<0.01	100.16	13.37	0.36	14.85
20R-1, 141–144	104.31	26	II	Dunite	40.86	0.01	0.16	10.36	47.85	0.12	<0.06	0.04	<0.01	99.41	14.74	0.32	16.24
23R-2, 0–3	127.45	1	II	Mud	45.16	0.02	0.94	8.42	44.43	0.10	<0.06	0.14	0.02	99.27	14.56	0.31	15.28
23R-2, 67–70	128.12	1	II	Mud	44.02	0.15	1.54	9.20	43.78	0.15	0.78	0.23	0.02	99.87	14.16	0.66	15.30
27R-1, 78–83	146.88	7	III	Harzburgite	44.41	0.01	0.77	8.36	45.01	0.11	0.46	<0.03	<0.01	99.14	12.41	0.29	13.68

Note: This table is also available in **ASCII.**

Table T5 (continued).

Core, section, interval (cm)	Depth (mbsf)	Piece	Unit	Lithology	Trace elements (ppm)									
					S	Cr	Ni	Ba	Sr	V	Y	Zr	Sc	Co
209-1274A-														
3R-1, 87–89	17.77	9B	I	Harzburgite	<350	2072	2417	<39	<5	33	<2	3	8.5	114
5R-1, 121–125	27.51	10B	I	Harzburgite	<350	2302	2388	<39	<5	33	<2	<2	8.3	114
7R-1, 48–54	36.28	5	I	Harzburgite	<350	2038	2390	<39	<5	32	<2	4	8.4	114
8R-1, 108–111	41.08	15C	I	Dunite	<350	1230	2697	<39	<5	14	4	2	5.1	127
11R-1, 75–79	55.65	12B	I	Harzburgite	<350	2801	2346	<39	<5	35	<2	<2	8.7	107
15R-1, 101–104	75.01	15	I	Dunite	<350	2234	2548	<39	<5	19	<2	2	6.1	123
17R-2, 16–19	89.91	1B	I	Harzburgite	<350	2665	2456	<39	<5	31	<2	<2	7.6	112
20R-1, 141–144	104.31	26	II	Dunite	638	1908	2688	<39	<5	15	<2	<2	3.8	126
23R-2, 0–3	127.45	1	II	Mud	672	2644	2413	<39	<5	36	3	10	8.7	106
23R-2, 67–70	128.12	1	II	Mud	3268	2683	2258	<39	<5	51	5	10	9.1	112
27R-1, 78–83	146.88	7	III	Harzburgite	<350	2493	2519	157	<5	29	<2	<2	7.4	116

Table T6. Thermal conductivity measurements, Hole 1274A.

Core, section, interval (cm)	Depth (mbsf)	Piece	Thermal conductivity* (W/[m·K])	Standard deviation	Standard error	Needle orientation	Apparent anisotropy (%)	Primary lithology
209-1274A-								
1R-1, 102–116	1.02	12	2.46	0.028	0.014	0	3.0	Harzburgite
1R-1, 102–116	1.02	12	2.50	0.012	0.006	1		Harzburgite
1R-1, 102–116	1.02	12	2.43	0.018	0.009	2		Harzburgite
3R-1, 43–53	17.33	6B	2.47	0.009	0.005	0	0.8	Harzburgite
3R-1, 43–53	17.33	6B	2.48	0.019	0.009	1		Harzburgite
3R-1, 43–53	17.33	6B	2.49	0.019	0.010	2		Harzburgite
4R-1, 37–48	21.67	2B	2.56	0.016	0.008	0	1.7	Harzburgite
4R-1, 37–48	21.67	2B	2.61	0.021	0.010	1		Harzburgite
4R-1, 37–48	21.67	2B	2.60	0.017	0.009	2		Harzburgite
5R-1, 130–143	27.60	11	2.27	0.013	0.006	0	7.4	Harzburgite
5R-1, 130–143	27.60	11	2.44	0.007	0.003	1		Harzburgite
5R-1, 130–143	27.60	11	2.29	0.009	0.005	2		Harzburgite
6R-2, 118–127	32.63	3	2.74	0.022	0.011	0	8.6	Harzburgite
6R-2, 118–127	32.63	3	2.78	0.013	0.007	1		Harzburgite
6R-2, 118–127	32.63	3	2.54	0.025	0.012	2		Harzburgite
7R-1, 14–26	35.94	3	2.57	0.016	0.008	0	4.8	Harzburgite
7R-1, 14–26	35.94	3	2.50	0.036	0.018	1		Harzburgite
7R-1, 14–26	35.94	3	2.62	0.019	0.009	2		Harzburgite
8R-1, 101–112	41.01	15C	2.63	0.023	0.012	0	4.9	Dunite
8R-1, 101–112	41.01	15C	2.58	0.024	0.012	1		Dunite
8R-1, 101–112	41.01	15C	2.71	0.027	0.014	2		Dunite
11R-1, 56–65	55.46	12A	2.50	0.021	0.010	0	2.7	Harzburgite
11R-1, 56–65	55.46	12A	2.57	0.026	0.013	1		Harzburgite
11R-1, 56–65	55.46	12A	2.51	0.023	0.011	2		Harzburgite
13R-1, 92–102	65.32	11	2.14	0.016	0.008	0	3.9	Harzburgite
13R-1, 92–102	65.32	11	2.20	0.005	0.003	1		Harzburgite
13R-1, 92–102	65.32	11	2.12	0.008	0.004	2		Harzburgite
15R-1, 38–46	74.38	7	3.03	0.014	0.007	0		Dunite
17R-2, 13–23	89.88	1B	2.52	0.006	0.003	0	3.3	Harzburgite
17R-2, 13–23	89.88	1B	2.60	0.025	0.012	1		Harzburgite
17R-2, 13–23	89.88	1B	2.53	0.049	0.024	2		Harzburgite
18R-1, 110–122	94.40	19	2.68	0.024	0.012	0	4.0	Harzburgite
18R-1, 110–122	94.40	19	2.68	0.015	0.008	1		Harzburgite
18R-1, 110–122	94.40	19	2.57	0.045	0.022	2		Harzburgite
27R-1, 33–44	146.40	4B	2.45	0.032	0.016	0	5.6	Harzburgite
27R-1, 33–44	146.40	4B	2.34	0.022	0.011	1		Harzburgite
27R-1, 33–44	146.40	4B	2.32	0.009	0.005	2		Harzburgite

Notes: * = average of four measurements. 0 = parallel to core axis, 1 = oblique to core axis (~35°), 2 = oblique to core axis (~35°) in opposite direction. This table is also available in **ASCII.**

Table T7. Porosity, density, and velocity on discrete samples, Hole 1274A.

Core, section, interval (cm)	Depth (mbsf)	Volume measured in pycnometer			Volume measured with caliper			V_P (km/s)				V_P apparent anisotropy (%)	Primary lithology
		Density (Mg/m³)		Porosity (%)	Density (Mg/m³)		Porosity (%)	x	y	z	Mean		
		Bulk	Grain		Bulk	Grain							
209-1274A-													
3R-1, 89–91	17.79	2.75	2.78	1.5	2.75	—	—	5.33	5.10	5.00	5.14	6.5	Harzburgite
4R-1, 55–57	21.85	2.72	2.75	2.0	2.74	—	—	5.02	4.85	4.88	4.92	3.4	Harzburgite
5R-1, 125–127	27.55	2.60	2.68	4.6	2.62	—	—	4.29	4.35	4.32	4.32	1.3	Harzburgite
5R-2, 22–24	27.96	2.62	2.68	3.6	2.74	—	—	4.55	4.25	4.36	4.38	7.0	Harzburgite
6R-2, 29–31	31.74	2.61	2.67	4.1	2.61	—	—	4.49	4.47	4.50	4.49	0.8	Harzburgite
6R-3, 52–54	33.34	2.80	2.82	1.5	2.78	—	—	4.89	4.87	4.98	4.91	2.4	Harzburgite
7R-1, 52–54	36.32	2.73	2.76	1.9	2.66	—	—	4.53	4.53	4.52	4.53	0.2	Harzburgite
7R-1, 98–100	36.78	2.65	2.71	3.3	2.76	—	—	4.81	4.82	—	4.82	—	Harzburgite
8R-1, 106–108	41.06	2.63	2.65	1.3	2.64	—	—	4.91	4.87	4.87	4.88	0.9	Dunite
11R-1, 74–76	55.64	2.61	2.66	3.1	2.64	—	—	4.70	4.60	4.55	4.61	3.4	Harzburgite
12R-1, 94–96	60.34	2.57	2.63	4.2	2.57	—	—	4.18	4.24	4.20	4.20	1.4	Harzburgite
14R-1, 68–70	69.68	2.57	2.62	3.5	2.61	—	—	4.52	4.39	—	4.45	—	Harzburgite
15R-1, 101–103	75.01	2.52	2.59	4.7	2.51	—	—	4.24	4.18	4.07	4.17	4.1	Harzburgite
16R-2, 17–19	85.31	2.52	2.59	4.0	2.52	—	—	4.02	4.11	4.03	4.05	2.2	Dunite
17R-2, 19–21	89.94	2.56	2.63	4.4	2.53	—	—	3.91	3.82	3.86	3.84	0.8	Harzburgite
20R-1, 145–147	104.35	2.44	2.59	9.7	2.51	—	—	3.75	3.81	3.89	3.82	3.5	Dunite
27R-1, 35–37	146.45	2.47	2.61	8.4	2.48	—	—	3.86	3.91	3.82	3.86	2.2	Harzburgite
27R-1, 83–85	146.93	2.62	2.66	2.8	2.69	—	—	4.47	4.50	4.56	4.51	2.1	Harzburgite

Note: This table is also available in **ASCII.**

Table T8. Summary of discrete sample data, Hole 1274A.

Core, section, interval (cm)	Depth (mbsf)	Piece	Lithology	NRM (A/m)	MDF (mT)	*N*	Decay type	MAD (°)	Remanence direction (°)		Demagnetization (mT)		*J* (A/m)	PCA (%)
									Declination	Inclination	Low	High		
209-1274A-														
3R-1, 89	17.79	9B	2	0.28	13.5	9	F	1.3	189.6	5.6	12	60	0.1420	50.53
4R-1, 55	21.85	3	2	0.45	13.7	8	F	2	329.4	5.8	15	60	0.1867	41.58
5R-1, 125	27.55	10B	2	0.68	6.8	6	F	1.9	314.3	–7.4	15	40	0.2415	35.72
5R-2, 22	27.96	1B	2	0.52	8.1	7	F	1.8	319	12.4	12	40	0.1714	33.28
6R-2, 29	31.74	1A	2	1.09	9.4	8	F	1.6	74.6	20.1	15	60	0.4057	37.22
6R-3, 52	33.34	1B	2	0.59	10.2	8	F	2	6.2	12.5	12	50	0.2613	44.59
7R-1, 52	36.32	5	2	1.11	10.8	10	F	2.3	29.7	30.4	12	70	0.4851	43.70
7R-1, 98	36.78	7A	2	0.69	11.0	9	F	1.6	301.2	17.9	12	60	0.3128	45.47
8R-1, 106	41.06	15C	1	1.69	6.8	7	F	3.4	323	42.9	15	60	0.4570	27.04
11R-1, 74	55.64	12B	2	1.85	6.8	5	F	3.3	212	6.4	20	50	0.2075	11.22
12R-1, 94	60.34	13	2	2.23	3.2	6	F	2.6	256.7	9.6	20	60	0.2434	10.91
14R-1, 68	69.68	8C	2	2.34	6.7	6	F	1.7	295.2	14.4	15	50	0.5733	24.50
15R-1, 101	75.01	15A	2	2.55	10.0	6	F	1.6	312.9	–1.3	20	60	0.5876	23.04
16R-2, 17	85.31	1B	1.5	2.03	10.9	6	F	1.2	292.2	3.3	15	40	0.7454	36.72
17R-2, 19	89.94	1B	2	2.54	8.9	6	F	2.9	266.1	0.6	15	40	0.8692	34.22
20R-1, 145	104.35	26	1	2.47	2.7	6	F	1.2	343.2	–52	20	50	0.6081	24.62
27R-1, 35	146.45	4B	2	1.79	5.8	7	F	2.7	255.7	23.7	15	50	0.3845	21.48
27R-1, 83	146.93	7	2	1.25	8.7	8	F	1.8	248.7	27.1	12	50	0.4999	39.99

Notes: Lithology: 1 = dunite, 1.5 = dunite/harzburgite, 2 = harzburgite. NRM = natural remanent magnetization, MDF = median destructive field for vector difference sum. *N* = number of points. Decay type: F = free of origin. MAD = maximum angular deviation. Principal component analysis (PCA) (%) = percentage of NRM intensity. This table is also available in **ASCII.**

Table T9. Anisotropy of magnetic susceptibility, Hole 1274A.

Core, section, interval (cm)	Depth (mbsf)	Piece	Susceptibility (SI)	1 σ	Maximum*			Intermediate*			Minimum*		
					Value	Dec (°)	Inc (°)	Value	Dec (°)	Inc (°)	Value	Dec (°)	Inc (°)
209-1274A-													
3R-1, 89	17.79	9B	3.860E–03	0.00027	0.3452	51.7	5.5	0.3351	145.5	34.4	0.3198	313.7	55.0
4R-1, 55	21.85	3	4.429E–03	0.00024	0.3429	10.2	9.3	0.3324	271.7	42.2	0.3247	110.1	46.3
5R-1, 125	27.55	10B	8.797E–03	0.00012	0.3565	50.8	60.0	0.3378	272.1	23.5	0.3057	174.2	17.6
5R-2, 22	27.96	1B	6.880E–03	0.00014	0.3534	205.8	17.0	0.3380	74.9	64.9	0.3086	301.4	17.8
6R-2, 29	31.74	1A	1.278E–02	0.00053	0.3509	145.7	31.5	0.3365	326.1	58.5	0.3125	235.8	0.2
6R-3, 52	33.34	1B	5.478E–03	0.00028	0.3555	99.6	75.9	0.3372	210.9	5.2	0.3073	302.1	13.1
7R-1, 52	36.32	5	8.541E–03	0.0002	0.3583	104.4	48.4	0.3236	0.2	12.2	0.3181	260.2	39.0
7R-1, 98	36.78	7A	6.366E–03	0.00015	0.3527	153.9	4.6	0.3306	61.5	27.7	0.3167	252.6	61.8
8R-1, 106	41.06	15C	1.316E–02	0.00013	0.3436	59.6	62.3	0.3352	240.0	27.7	0.3213	149.9	0.2
11R-1, 74	55.64	12B	1.469E–02	0.00016	0.3490	54.6	43.4	0.3331	217.0	45.2	0.3179	316.1	8.9
12R-1, 94	60.34	13	1.617E–02	0.00016	0.3477	62.5	47.5	0.3404	281.1	35.6	0.3118	176.0	20.1
14R-1, 68	69.68	8C	2.301E–02	0.00015	0.3520	337.1	12.0	0.3368	91.0	62.4	0.3113	241.5	24.5
15R-1, 101	75.01	15A	2.562E–02	0.00006	0.3448	2.6	41.2	0.3300	173.8	48.5	0.3252	268.8	4.4
16R-2, 17	85.31	1B	2.415E–02	0.00032	0.3635	125.7	38.7	0.3292	315.2	50.9	0.3073	219.5	4.7
17R-2, 19	89.94	1B	3.034E–02	0.00035	0.3582	162.4	12.1	0.3382	58.6	48.0	0.3036	262.5	39.5
20R-1, 145	104.35	26	1.099E–01	0.00018	0.3465	257.8	45.3	0.3390	110.9	39.7	0.3145	6.0	17.2
27R-1, 35	146.45	4B	2.112E–02	0.00022	0.3450	287.2	60.4	0.3440	124.5	28.5	0.3110	30.4	7.4
27R-1, 83	146.93	7	1.220E–02	0.00015	0.3461	314.0	65.5	0.3355	113.9	23.2	0.3184	207.1	7.6

Notes: σ = 1 standard deviation for normalized eigenvalues. Total anisotropy critical value = 3.4817. * = unrotated core coordinates (double line on working half = 360°, inclination positive down). Dec = declination, inc = inclination. F12 = max, min eigenvalues, F23 = int, min eigenvalues (critical value = 4.2565 for F12 and F23). *P* (degree of anisotropy) = max/min eigenvalues, *F* (magnetic foliation) = int/min eigenvalues, *L* (magnetic lineation) = max/int eigenvalues. AMS = anisotropy of magnetic susceptibility. † = anisotropy of magnetic susceptibility core coordinates rotated to 360°. This table is available in **ASCII.**

Table T9 (continued).

Core, section, interval (cm)	Depth (mbsf)	Piece	Total anisotropy	F12	F23	*P*	*F*	*L*	Minimum†		Maximum†	
									Dec (°)	Inc (°)	Dec (°)	Inc (°)
209-1274A-												
3R-1, 89	17.79	9B	1771.6	688.0	1588.5	1.079	1.048	1.030	124.1	55.0	222.1	5.5
4R-1, 55	21.85	3	1132.9	945.1	495.1	1.056	1.023	1.032	140.7	46.3	40.8	9.3
5R-1, 125	27.55	10B	9999.9	9999.9	9999.9	1.166	1.105	1.056	219.9	17.6	96.5	60.0
5R-2, 22	27.96	1B	9999.9	5791.2	9999.9	1.145	1.095	1.045	342.4	17.8	246.8	17.0
6R-2, 29	31.74	1A	1085.5	373.4	1039.0	1.123	1.077	1.043	161.2	0.2	71.1	31.5
6R-3, 52	33.34	1B	6129.8	2185.0	5760.6	1.157	1.097	1.054	295.9	13.1	93.4	75.9
7R-1, 52	36.32	5	9062.9	9999.9	365.8	1.127	1.017	1.107	230.5	39.0	74.7	48.4
7R-1, 98	36.78	7A	9999.9	9999.9	4337.4	1.114	1.044	1.067	311.4	61.8	212.7	4.6
8R-1, 106	41.06	15C	5597.2	1952.9	5318.9	1.069	1.043	1.025	186.9	0.2	96.6	62.3
11R-1, 74	55.64	12B	7462.3	4831.8	4498.1	1.098	1.048	1.048	104.1	8.9	202.6	43.4
12R-1, 94	60.34	13	9999.9	1037.7	9999.9	1.115	1.092	1.021	279.3	20.1	165.8	47.5
14R-1, 68	69.68	8C	9999.9	4828.3	9999.9	1.131	1.082	1.045	306.3	24.5	41.9	12.0
15R-1, 101	75.01	15A	9999.9	9999.9	3260.8	1.060	1.015	1.045	315.9	4.4	49.7	41.2
16R-2, 17	85.31	1B	6155.5	5648.3	2293.8	1.183	1.071	1.104	287.3	4.7	193.5	38.7
17R-2, 19	89.94	1B	5030.7	1639.7	4945.3	1.180	1.114	1.059	356.4	39.5	256.3	12.1
20R-1, 145	104.35	26	6983.4	868.8	9371.6	1.102	1.078	1.022	22.8	17.2	274.6	45.3
27R-1, 35	146.45	4B	6372.0	11.7	9999.9	1.110	1.106	1.003	134.7	7.4	31.5	60.4
27R-1, 83	146.93	7	6618.0	2370.5	6203.5	1.087	1.054	1.031	318.4	7.6	65.3	65.5

Table T10. Anisotropy of anhysteretic remanent magnetization, Hole 1274A.

Core, section, interval (cm)	Depth (mbsf)	Piece	ARM (A/m)	1 σ	Maximum*			Intermediate*			Minimum*		
					Value	Dec (°)	Inc (°)	Value	Dec (°)	Inc (°)	Value	Dec (°)	Inc (°)
209-1274A-													
3R-1, 89	17.79	9B	1.14E+00	0.00278	0.3546	53.3	22.2	0.3358	322.0	3.2	0.3096	224.2	67.5
4R-1, 55	21.85	3	1.71E+00	0.00479	0.3503	6.4	0.6	0.3288	275.7	50.6	0.3210	96.9	39.4
5R-1, 125	27.55	10B	3.22E+00	0.00521	0.3785	123.9	65.3	0.3419	254.2	16.6	0.2796	349.7	17.8
5R-2, 22	27.96	1B	2.06E+00	0.00326	0.3774	28.9	34.5	0.3309	226.0	54.3	0.2917	124.5	8.1
6R-2, 29	31.74	1A	3.98E+00	0.00545	0.3628	138.2	3.6	0.3559	34.1	75.7	0.2813	229.1	13.8
6R-3, 52	33.34	1B	2.41E+00	0.00438	0.3895	47.4	68.0	0.3257	203.5	20.3	0.2848	296.5	8.2
7R-1, 52	36.32	5	4.19E+00	0.00455	0.3798	84.9	54.3	0.3207	314.9	24.8	0.2995	213.0	23.9
7R-1, 98	36.78	7A	2.64E+00	0.00458	0.3717	151.1	8.0	0.3234	56.3	30.9	0.3049	254.0	57.9
8R-1, 106	41.06	15C	4.77E+00	0.00560	0.3646	32.1	85.7	0.3242	206.0	4.3	0.3113	296.0	0.5
11R-1, 74	55.64	12B	5.73E+00	0.00546	0.3569	163.0	70.9	0.3490	50.7	7.5	0.2941	318.3	17.5
12R-1, 94	60.34	13	5.69E+00	0.00852	0.3734	245.2	47.5	0.3582	99.3	37.2	0.2683	355.4	17.5
14R-1, 68	69.68	8C	9.65E+00	0.01150	0.3654	150.9	10.7	0.3399	15.0	75.2	0.2947	242.8	10.1
15R-1, 101	75.01	15A	1.11E+01	0.00984	0.3501	135.9	80.1	0.3363	345.0	8.7	0.3136	254.3	4.7
16R-2, 17	85.31	1B	1.00E+01	0.00979	0.3747	120.2	28.0	0.3683	335.6	56.9	0.2570	219.1	16.2
17R-2, 19	89.94	1B	1.58E+01	0.00886	0.3756	148.9	20.0	0.3499	35.2	47.8	0.2745	253.9	35.3
20R-1, 145	104.35	26	2.06E+01	0.00409	0.3601	290.1	36.0	0.3461	65.5	44.4	0.2938	181.3	24.0
27R-1, 35	146.45	4B	6.40E+00	0.01907	0.3842	293.0	64.1	0.3349	116.8	25.8	0.2809	26.1	1.5
27R-1, 83	146.93	7	4.81E+00	0.01820	0.3656	171.7	77.9	0.3413	297.2	7.1	0.2931	28.4	9.8

Notes: ARM = anhysteretic remanent magnetization. σ = 1 standard deviation for normalized eigenvalues. Total anisotropy critical value = 3.4817. * = unrotated core coordinates (double line on working half = 360°, inclination positive down). Dec = declination, inc = inclination. F12 = max, min eigenvalues, F23 = int, min eigenvalues (critical value = 4.2565 for F12 and F23). *P* (degree of anisotropy) = max/min eigenvalues, *F* (magnetic foliation) = int/min eigenvalues, *L* (magnetic lineation) = max/int eigenvalues. † = anisotropy of anhysteretic remanent magnetization core coordinates rotated to 360°. This table is also available in **ASCII.**

Table T10 (continued).

Core, section, interval (cm)	Depth (mbsf)	Piece	Total anisotropy	F12	F23	*P*	*F*	*L*	Minimum†		Maximum†	
									Dec (°)	Inc (°)	Dec (°)	Inc (°)
209-1274A-												
3R-1, 89	17.79	9B	52.89	23.03	44.23	1.145	1.084	1.056	34.6	67.5	223.7	22.2
4R-1, 55	21.85	3	8.01	10.06	1.32	1.091	1.024	1.065	127.5	39.4	37.0	0.6
5R-1, 125	27.55	10B	73.62	24.70	71.35	1.354	1.223	1.107	35.4	17.8	169.6	65.3
5R-2, 22	27.96	1B	138.53	101.61	72.39	1.294	1.134	1.140	165.5	8.1	69.9	34.5
6R-2, 29	31.74	1A	55.08	0.80	93.83	1.290	1.265	1.019	154.5	13.8	63.6	3.6
6R-3, 52	33.34	1B	115.77	105.73	43.51	1.367	1.144	1.196	290.3	8.2	41.2	68.0
7R-1, 52	36.32	5	66.86	84.42	10.78	1.268	1.071	1.184	183.3	23.9	55.2	54.3
7R-1, 98	36.78	7A	45.53	55.79	8.20	1.219	1.061	1.150	312.8	57.9	209.9	8.0
8R-1, 106	41.06	15C	19.71	26.00	2.65	1.171	1.041	1.125	333.0	0.5	69.1	85.7
11R-1, 74	55.64	12B	31.34	1.03	50.53	1.213	1.187	1.022	106.3	17.5	311.0	70.9
12R-1, 94	60.34	13	35.57	1.59	55.69	1.392	1.335	1.042	98.7	17.5	348.5	47.5
14R-1, 68	69.68	8C	7.75	2.47	7.71	1.240	1.153	1.075	307.6	10.1	215.7	10.7
15R-1, 101	75.01	15A	2.81	0.97	2.68	1.116	1.073	1.041	301.4	4.7	183.0	80.1
16R-2, 17	85.31	1B	36.54	0.21	64.62	1.458	1.433	1.017	286.9	16.2	188.0	28.0
17R-2, 19	89.94	1B	28.15	4.19	36.27	1.368	1.275	1.073	347.8	35.3	242.8	20.0
20R-1, 145	104.35	26	58.39	5.84	81.79	1.226	1.178	1.040	198.1	24.0	306.9	36.0
27R-1, 35	146.45	4B	5.87	3.35	4.00	1.368	1.192	1.147	130.4	1.5	37.3	64.1
27R-1, 83	146.93	7	3.30	0.89	3.52	1.248	1.165	1.071	139.7	9.8	283.0	77.9

Table T11. Piece orientations from archive-half data, Hole 1274A. (**See table notes.** Continued on next two pages.)

Core, section, interval (cm)	Length (cm)	Piece	Lithology	PCA interval (cm)	Depth (mbsf)	*N*	Decay type	MAD (°)	Remanence direction (°)		Demagnetization (mT)		*J* (A/m)	PCA (%)
									Declination	Inclination	Low	High		
209-1274A-														
1R-1, 8–17	10	2	2	14	0.14	5	F	5.1	295.2	15.5	20	40	0.1972	19.9
1R-1, 24–30	6	4	2	28	0.28	4	A	0.9	75.5	5.2	25	40	0.1580	39.9
1R-1, 31–38	7	5	2	36	0.36	4	A	0.9	111.4	–2.7	25	40	0.1360	38.9
1R-1, 39–51	12	6	2	44	0.44	4	A	2.1	266.7	12.6	25	40	0.1579	33.8
1R-1, 39–51	12	6	2	46	0.46	4	A	1.8	264.1	13.4	25	40	0.1699	37.0
1R-1, 73–92	19	10	2	78	0.78	5	F	2.1	274.5	14.5	20	40	0.0911	24.9
1R-1, 73–92	19	10	2	82	0.82	4	F	1	271.3	15.1	25	40	0.0651	18.4
1R-1, 103–117	14	12	2	110	1.10	4	A	1	230.0	11.0	25	40	0.1840	44.5
1R-1, 118–129	11	13	2	126	1.26	4	A	1.6	251.9	19.4	25	40	0.1439	46.7
2R-1, 11–18	7	3	2	14	12.04	4	F	4.1	85.7	11.5	25	50	0.2236	25.8
2R-1, 28–38	10	6	2	32	12.22	4	F	3	267.4	–21	25	50	0.1212	34.7
3R-1, 25–53	28	6	2	30	17.20	6	F	5.2	288.3	17.9	20	50	0.0760	14.9
3R-1, 25–53	28	6	2	40	17.30	4	F	5.7	291.0	14.9	30	50	0.0268	6.6
3R-1, 61–74	14	8	2	68	17.58	6	A	5.7	225.5	22.0	20	50	0.1707	23.9
3R-1, 75–122	47	9	2	82	17.72	4	A	1.9	201.6	14.4	30	50	0.0514	14.4
3R-1, 75–122	47	9	2	90	17.80	4	A	2.2	191.9	12.9	30	50	0.0493	17.1
3R-1, 75–122	47	9	2	100	17.90	4	A	2	191.1	9.8	30	50	0.0581	19.5
3R-1, 75–122	47	9	2	110	18.00	4	A	2.3	189.9	7.0	30	50	0.0574	22.2
4R-1, 0–23	23	1	2	14	21.44	4	A	1.6	313.8	–0.1	30	50	0.0870	17.7
4R-1, 24–47	23	2	2	36	21.66	4	A	0.9	316.5	1.8	30	50	0.0972	21.8
4R-1, 48–101	53	3	2	60	21.90	4	A	1.4	335.2	3.0	30	50	0.0862	18.9
4R-1, 48–101	53	3	2	70	22.00	4	A	1.6	333.5	0.7	30	50	0.0821	16.8
4R-1, 48–101	53	3	2	80	22.10	4	A	2.7	329.0	2.7	30	50	0.0957	19.4
4R-1, 105–122	18	5	2	118	22.48	2	A	1.8	121.0	2.6	30	35	0.0825	14.5
4R-1, 123–134	11	6	2	128	22.58	5	F	6.4	263.8	10.1	25	50	0.1232	19.5
4R-1, 123–134	11	6	2	130	22.60	5	F	4.5	264.9	10.2	25	50	0.1070	16.8
4R-1, 139–146	7	8	2	144	22.74	4	F	10.1	311.3	7.4	30	50	0.0578	13.9
4R-2, 0–32	32	1	2	10	22.86	5	F	6.7	9.1	8.3	25	50	0.0753	13.3
5R-1, 25–35	10	5	2	30	26.60	5	F	8.4	168.4	11.1	25	50	0.1436	22.2
5R-1, 36–44	8	6	2	40	26.70	5	F	6.2	267.0	22.3	25	50	0.1198	20.0
5R-1, 46–57	11	7	2	52	26.82	7	+	5.4	347.4	17.8	20	50	0.2709	28.7
5R-1, 58–70	12	8	2	66	26.96	6	+	3.1	321.8	19.6	25	50	0.1599	18.8
5R-1, 71–104	33	9	2	80	27.10	4	A	12.3	298.5	–16	30	50	0.0696	11.5
5R-1, 71–104	33	9	2	90	27.20	4	A	6.5	315.9	–16.4	30	50	0.1049	13.7
5R-1, 105–129	24	10	2	120	27.50	4	A	6.2	316.9	–9.7	30	50	0.0907	9.8
5R-1, 129–143	14	11	2	136	27.66	4	A	9.2	253.3	–4	30	50	0.1129	14.0
5R-2, 1–53	52	1	2	20	27.94	6	F	4.3	341.0	28.6	20	50	0.0823	12.3
5R-2, 1–53	52	1	2	30	28.04	6	F	4.7	333.4	28.5	20	50	0.0947	13.7
5R-2, 1–53	52	1	2	40	28.14	6	F	4.3	334.0	24.9	20	50	0.1142	14.5
5R-2, 55–89	34	2	2	70	28.44	6	F	5	356.4	26.4	20	50	0.1019	13.2
5R-2, 55–89	34	2	2	80	28.54	6	F	4.9	353.9	24.2	20	50	0.1366	12.7
5R-2, 94–120	26	4	2	106	28.80	6	F	5.1	1.9	26.5	20	50	0.1407	11.6
5R-2, 121–131	10	5	2	126	29.00	5	F	4.1	344.7	21.9	20	40	0.0785	14.8
6R-1, 41–63	22	7	2	54	31.34	6	A	3.3	334.7	17.2	20	50	0.1928	22.0
6R-2, 0–102	102	1	2	20	31.65	4	A	1.9	91.4	20.2	25	40	0.0904	13.2
6R-2, 0–102	102	1	2	30	31.75	4	A	2	85.9	18.6	25	40	0.0963	17.1
6R-2, 0–102	102	1	2	40	31.85	4	A	1.6	86.5	15.6	25	40	0.1320	18.1
6R-2, 0–102	102	1	2	60	32.05	4	A	1.4	85.8	17.8	25	40	0.1170	18.8
6R-2, 0–102	102	1	2	70	32.15	4	A	1.7	88.0	18.8	25	40	0.0861	16.2
6R-2, 0–102	102	1	2	80	32.25	4	A	2	87.0	20.3	25	40	0.0867	15.4
6R-2, 0–102	102	1	2	90	32.35	4	A	2.5	88.2	18.5	25	40	0.1169	14.1
6R-2, 105–117	12	2	2	110	32.55	5	A	4.7	326.2	19.1	25	50	0.1737	14.9
6R-2, 118–128	10	3	2	122	32.67	5	F	4.9	327.2	29.9	25	50	0.1132	10.7
6R-2, 129–136	7	4	2	132	32.77	5	F	5.4	321.3	29.2	25	50	0.0890	11.4
6R-3, 1–86	85	1	2	8	32.90	5	F	5.9	9.3	22.0	25	50	0.0852	11.2
6R-3, 1–86	85	1	2	10	32.92	5	F	7	9.8	22.7	25	50	0.0815	10.9
6R-3, 1–86	85	1	2	12	32.94	5	F	7.8	10.7	22.9	25	50	0.0812	10.8
6R-3, 1–86	85	1	2	20	33.02	5	F	8.1	10.5	26.6	25	50	0.0796	10.3
6R-3, 1–86	85	1	2	30	33.12	5	F	9.1	7.4	24.7	25	50	0.0757	9.8
6R-3, 1–86	85	1	2	40	33.22	5	F	9.4	4.1	28.5	25	50	0.0669	9.3
6R-3, 1–86	85	1	2	50	33.32	5	F	8.9	4.8	27.6	25	50	0.0585	9.0
6R-3, 1–86	85	1	2	60	33.42	5	F	8.3	6.6	25.3	25	50	0.0752	10.2
6R-3, 1–86	85	1	2	70	33.52	5	A	4.2	5.9	19.6	25	50	0.1108	15.1
6R-3, 88–98	10	2	2	94	33.76	3	A	2	289.4	13.3	35	50	0.0584	8.6
6R-3, 99–126	27	3	2	112	33.94	3	A	2.4	300.6	14.0	35	50	0.0845	9.8
6R-3, 99–126	27	3	2	120	34.02	3	A	1.5	301.6	11.2	35	50	0.1020	12.4

Table T11 (continued).

Core, section, interval (cm)	Length (cm)	Piece	Lithology	PCA interval (cm)	Depth (mbsf)	N	Decay type	MAD (°)	Remanence direction (°)		Demagnetization (mT)		J (A/m)	PCA (%)
									Declination	Inclination	Low	High		
7R-1, 3–13	10	2	2	10	35.90	2	A	5.3	190.2	–12.8	30	35	0.0917	10.2
7R-1, 13–27	14	3	2	20	36.00	3	A	6.5	85.1	2.3	35	50	0.1250	10.6
7R-1, 29–45	16	4	2	36	36.16	4	A	2.1	303.6	26.7	30	50	0.2359	15.7
7R-1, 46–65	19	5	2	58	36.38	4	A	3.5	47.8	29.3	30	50	0.1809	11.4
7R-1, 67–84	17	6	2	78	36.58	5	F	3.3	329.9	22.6	25	50	0.1048	10.5
7R-1, 86–134	48	7	2	98	36.78	5	A	3.4	304.6	15.9	25	50	0.1548	18.0
7R-1, 86–134	48	7	2	110	36.90	5	A	3.4	304.7	18.1	25	50	0.1548	16.4
7R-1, 86–134	48	7	2	120	37.00	4	A	2.9	302.4	15.2	30	50	0.1099	13.6
7R-2, 1–11	10	1	2	6	37.22	4	A	2.5	240.6	12.9	30	50	0.1280	19.8
7R-2, 12–46	34	2	2	20	37.36	4	A	3.3	332.4	12.7	30	50	0.1488	15.1
7R-2, 12–46	34	2	2	30	37.46	4	A	3.2	331.9	16.1	30	50	0.1288	13.5
8R-1, 14–22	8	3	2	16	40.16	2	A	1.1	285.8	57.3	30	35	0.1030	9.8
8R-1, 44–52	8	8	2	50	40.50	3	A	7.1	328.6	–13.8	35	50	0.1211	8.7
8R-1, 59–67	8	10	2	62	40.62	4	A	4.8	312.8	15.2	30	50	0.0989	14.2
8R-1, 71–82	11	12	1	76	40.76	4	A	6.1	130.8	26.0	30	50	0.1117	10.4
8R-1, 95–112	17	15	1	100	41.00	4	F	4.5	327.8	22.6	30	50	0.1155	7.4
8R-1, 95–112	17	15	1	104	41.04	4	F	3.3	333.8	27.9	30	50	0.1222	6.4
8R-1, 119–128	9	17	1	124	41.24	4	F	3.3	314.7	20.6	30	50	0.0882	5.7
8R-1, 134–141	7	19	1	138	41.38	3	A	1.6	116.8	17.7	35	50	0.0643	7.3
8R-2, 1–10	9	1	1	6	41.53	3	A	2.3	5.6	17.5	35	50	0.0958	4.6
8R-2, 11–20	9	2	1	18	41.65	3	A	2.1	264.9	19.6	25	35	0.1359	17.0
8R-2, 99–107	8	17	2	104	42.51	3	A	4.4	127.4	1.3	30	40	0.1349	7.7
9R-1, 28–37	9	7	1	32	45.62	5	A	4.6	254.2	15.5	20	40	0.2290	23.4
10R-1, 3–11	8	2	1	8	49.98	4	A	5.6	138.0	46.9	30	50	0.1447	10.8
11R-1, 56–84	28	12	2	72	55.62	5	A	7.5	221.7	19.7	25	50	0.1379	8.1
11R-1, 93–100	7	15	2	96	55.86	4	F	9.7	310.8	19.2	30	50	0.0614	6.3
11R-1, 102–114	12	16	1	108	55.98	4	F	6.6	286.6	11.2	30	50	0.0882	4.8
11R-1, 116–122	6	17	2	120	56.10	5	F	4.2	5.1	56.8	25	50	0.0777	6.8
12R-1, 7–15	8	2	2	10	59.50	5	F	10.5	223.2	10.5	25	50	0.0704	8.7
12R-1, 22–32	10	4	2	28	59.68	5	A	5	43.4	22.5	25	50	0.1137	6.9
12R-1, 40–47	7	6	2	44	59.84	4	A	5	335.3	–0.4	25	40	0.1169	10.4
12R-1, 60–77	17	10	2	70	60.10	5	A	2.2	275.6	7.9	25	50	0.1500	8.5
12R-1, 88–106	18	13	2	96	60.36	5	F	6.1	265.6	18.6	25	50	0.1354	9.2
12R-1, 109–118	9	14	1	114	60.54	6	F	3.1	317.5	25.7	20	50	0.2488	22.6
12R-1, 127–134	7	17	1	130	60.70	5	F	4.4	341.1	11.9	25	50	0.1089	9.5
12R-1, 135–144	9	18	2	140	60.80	5	F	2.5	303.0	11.9	25	50	0.1805	10.3
12R-2, 11–22	11	3	2	16	61.06	5	A	4.7	274.0	13.9	25	50	0.1328	11.0
12R-2, 23–32	9	4	2	28	61.18	5	A	5.2	290.7	12.8	25	50	0.1368	13.2
12R-2, 33–44	11	5	2	40	61.30	5	A	3.4	262.6	9.3	25	50	0.1219	11.7
13R-1, 0–16	16	1	2	8	64.48	4	F	6.1	110.2	0.8	30	50	0.1151	3.9
13R-1, 17–40	23	2	2	30	64.70	5	A	3.6	270.9	10.3	25	50	0.1960	7.3
13R-1, 45–53	8	4	2	48	64.88	3	A	2.2	351.1	11.3	25	35	0.1250	7.0
13R-1, 54–61	7	5	2	58	64.98	5	A	4.5	303.1	12.4	25	50	0.1239	7.7
13R-1, 67–73	6	7	2	70	65.10	5	A	4.7	306.6	8.4	25	50	0.1259	5.7
13R-1, 92–103	11	11	2	96	65.36	4	A	7.4	266.7	13.5	20	35	0.4682	7.1
14R-1, 14–25	11	3	2	22	69.22	4	A	1.8	33.6	27.5	25	40	0.2999	7.8
14R-1, 30–40	10	5	2	34	69.34	3	A	5.2	213.3	13.2	30	40	0.1156	6.5
14R-1, 55–75	20	8	2	66	69.66	6	F	5.3	312.9	31.1	20	50	0.3364	11.6
15R-1, 8–16	8	2	1	12	74.12	5	A	7.9	223.6	43.0	20	40	0.1409	11.4
15R-1, 38–47	9	7	1	44	74.44	5	F	5	114.5	52.8	20	40	0.3465	6.2
15R-1, 62–70	8	10	1	66	74.66	5	A	5.7	341.3	23.8	25	50	0.3528	10.1
15R-1, 95–129	34	15	2	110	75.10	4	A	5.1	316.5	5.7	25	40	0.3395	11.7
15R-2, 0–8	8	1	2	4	75.51	4	A	5	208.3	7.6	30	50	0.1429	9.1
15R-2, 9–21	12	2	2	16	75.63	5	A	4.3	260.5	2.0	25	50	0.2829	12.8
15R-2, 23–31	8	3	2	28	75.75	5	A	5.7	131.9	13.1	25	50	0.1396	8.3
15R-2, 38–48	10	5	2	42	75.89	4	F	3.9	54.5	–3	30	50	0.1347	7.2
15R-2, 54–68	14	7	2	64	76.11	5	F	12.2	207.4	18.1	25	50	0.0879	7.8
15R-2, 75–86	11	9	2	80	76.27	4	A	2.9	315.8	0.2	20	35	0.3607	17.9
16R-1, 31–40	9	5	1	36	84.06	4	A	2.9	7.1	7.3	20	35	0.3188	24.6
16R-1, 45–53	8	7	2	50	84.20	5	A	3	304.3	4.3	25	50	0.3766	16.2
16R-1, 74–88	14	11	1	82	84.52	6	F	3.2	317.8	14.7	20	50	0.3784	13.7
16R-1, 104–118	14	14	1	110	84.80	5	F	1.9	315.9	6.8	25	50	0.2192	7.1
16R-1, 135–143	8	18	1	140	85.10	4	A	6.7	93.0	13.8	25	40	0.1339	9.4
16R-2, 0–38	38	1	1	20	85.34	4	A	4.8	298.9	10.0	25	40	0.3057	9.7
16R-2, 0–38	38	1	1	30	85.44	4	A	5.7	301.2	15.0	25	40	0.1799	7.8
16R-2, 48–58	10	3	1	54	85.68	6	A	6.5	201.2	12.0	20	50	0.1688	18.2
16R-2, 67–79	12	6	1	74	85.88	6	A	5.4	162.0	6.8	20	50	0.2498	29.1
16R-2, 85–96	11	8	2	92	86.06	3	A	2.8	22.0	1.3	25	35	0.0884	8.2

Table T11 (continued).

Core, section, interval (cm)	Length (cm)	Piece	Lithology	PCA interval (cm)	Depth (mbsf)	*N*	Decay type	MAD (°)	Remanence direction (°)		Demagnetization (mT)		*J* (A/m)	PCA (%)
									Declination	Inclination	Low	High		
16R-2, 106–112	6	11	2	110	86.24	5	A	2.4	66.7	–0.1	20	40	0.0842	15.0
16R-2, 123–131	8	14	2	128	86.42	5	A	4	245.3	–4.2	20	40	0.2509	25.7
17R-1, 113–121	8	20	2	118	89.48	5	A	3.2	5.2	30.6	20	40	0.9689	31.9
17R-1, 122–129	7	21	2	126	89.56	3	A	4.4	75.5	50.2	30	40	0.2568	10.2
17R-2, 0–23	23	1	2	14	89.89	6	A	9.1	274.2	21.5	20	50	0.4667	20.7
17R-2, 25–34	9	2	2	30	90.05	5	A	1.6	276.8	14.0	20	40	0.4210	15.5
18R-1, 21–34	13	5	2	26	93.56	6	F	2.6	293.3	18.4	15	40	0.8921	27.9
18R-1, 83–92	9	15	2	88	94.18	4	A	2.9	231.7	11.2	25	40	0.2959	12.9
18R-1, 109–124	15	19	2	116	94.46	5	F	2.6	273.3	18.5	20	40	0.5580	17.7
18R-1, 136–144	8	23	2	142	94.72	5	F	1.9	283.3	58.2	20	40	0.0715	5.9
19R-1, 16–23	7	4	2	20	98.10	5	F	11.3	88.9	8.8	20	40	0.2826	16.3
20R-1, 35–43	8	8	1	40	103.30	5	F	5.5	11.5	16.7	20	40	0.2361	4.6
20R-1, 83–92	9	17	1	88	103.78	5	F	3.6	281.2	6.4	20	40	0.2822	6.8
20R-1, 141–148	7	26	1	144	104.34	6	F	12.1	332.1	11.1	20	50	0.1882	5.1
21R-1, 91–98	7	23	1	94	113.44	6	F	6.3	0.6	30.0	20	50	0.0331	11.0
22R-1, 20–33	13	4	2	26	122.36	6	F	9.3	40.0	23.6	20	50	0.0781	11.5
23R-1, 1–10	9	1	10	6	126.86	3	A	5.8	285.3	18.2	35	50	0.0083	15.8
23R-1, 44–50	6	10	2	48	127.28	6	F	6.1	71.8	–29.1	20	50	0.1432	33.0
23R-2, 1–70	69	1	18	12	127.57	3	F	0.5	176.6	34.0	5	15	0.2250	40.5
23R-2, 1–70	69	1	18	20	127.65	3	F	1.9	156.0	20.2	5	15	0.2333	46.3
23R-2, 1–70	69	1	18	30	127.75	3	F	1	171.5	34.8	5	15	0.3426	40.3
23R-2, 1–70	69	1	18	40	127.85	3	F	3.5	194.6	51.9	5	15	0.2345	35.9
23R-2, 1–70	69	1	18	50	127.95	3	F	2.1	149.4	29.1	5	15	0.3939	45.0
23R-2, 1–70	69	1	18	60	128.05	3	F	0.4	160.4	33.2	5	15	0.2770	38.3
23R-2, 83–120	37	1B	18	88	128.33	3	F	1.6	164.4	41.7	5	15	0.1952	38.5
23R-2, 83–120	37	1B	18	100	128.45	3	F	0.3	122.4	28.9	5	15	0.2614	41.5
23R-2, 83–120	37	1B	18	110	128.55	3	F	1.8	84.6	52.7	5	15	0.4487	44.0
24R-1, 89–97	8	5	2	94	132.74	5	F	4.1	123.4	33.6	20	40	0.1214	13.0
24R-1, 97–106	9	6	2	102	132.82	5	F	4.6	343.9	14.0	20	40	0.1087	7.1
25R-1, 54–62	8	9	1	58	137.08	4	F	1.9	239.4	54.7	25	40	0.0327	1.0
25R-1, 63–70	7	10	1	66	137.16	5	F	3.8	271.2	9.5	20	40	0.0925	3.9
25R-1, 71–77	6	11	2	74	137.24	5	F	6.4	103.6	–2.8	20	40	0.0826	5.2
26R-1, 5–16	11	2	18	10	141.60	4	F	7.6	355.7	39.8	15	30	0.0138	5.1
26R-1, 5–16	11	2	18	12	141.62	5	F	8.4	310.1	62.6	15	35	0.0117	4.7
26R-1, 75–89	14	13	2	80	142.30	4	F	3.6	357.5	22.8	20	35	0.1313	7.5
27R-1, 15–44	29	4	2	20	146.30	4	F	1.6	281.5	37.3	20	35	0.1180	9.0
27R-1, 15–44	29	4	2	30	146.40	5	F	1.8	268.1	39.0	20	40	0.1742	11.3
27R-1, 56–67	11	6	2	60	146.70	3	A	4.1	304.5	17.7	30	40	0.1538	9.9
27R-1, 79–109	30	7	2	92	147.02	4	A	7.7	260.6	31.2	25	40	0.1964	10.6
27R-1, 79–109	30	7	2	100	147.10	4	A	7.4	257.2	28.9	25	40	0.2164	10.4
27R-1, 111–149	38	8	2	130	147.40	5	A	4.7	325.3	34.2	25	50	0.1708	8.7
27R-1, 111–149	38	8	2	140	147.50	5	A	3.6	321.0	29.5	25	50	0.2358	10.3
27R-2, 0–12	12	1	2	6	147.66	5	F	4.3	327.5	31.6	25	50	0.1368	8.3
27R-2, 13–22	9	2	2	16	147.76	5	F	8.3	0.7	53.0	25	50	0.0974	6.2

Notes: Lithology: 1 = dunite, 2 = harzburgite, 10 = gabbro, 18 = breccia. Principal component analysis (PCA) interval = level at which PCA analysis was performed. *N* = number of samples. Decay type: A = anchored to origin, F = free of origin, + = includes origin as point. MAD = maximum angular deviation. PCA (%) = percentage of natural remanent magnetization intensity. This table is also available in **ASCII.**

Table T12. Surface water and atmospheric microbiology results, 14–19 June 2003.

Sample	Date (Jun 2003)	Surface water (counts/mL)		Air growth* (CFU)		Atmospheric condition
		Bacteria	Virus	Bacteria	Fungi	
a	14	5.85×10^5	6.07×10^6	0/0	0/0	7.4: light cloud
b	15	4.34×10^5	6.00×10^6	0/0	0/0	No data
c	16	4.72×10^5	5.15×10^6	0/2	0/11	12.2: light/heavy dust
d	17	5.28×10^5	5.55×10^6	0/0	0/11	No data
e	18	5.09×10^5	4.87×10^6	0/6	0/9	8.4: light dust
f	19	4.72×10^5	6.02×10^6	0/–	0/–	9.9: light dust

Notes: * = colony-forming units (CFU) growth is measured at 48/96 hr. † = SeaWiFS image values.

Figure AF1. Comparison of whole-core and archive-half measurements of the natural remanent magnetization (NRM) for Sections 209-1274A-6R-3 and 6R-4. **A.** Whole-core measurements were made at two different orientations: +x-core axis parallel to +x-SQUID (blue crosses) and +x-core axis parallel to +y-SQUID axis (red circles). For the sake of comparison, declinations of the second run are plotted corrected by 90°. **B.** NRM data from whole-core and archive-half measurements of Sections 209-1274A-6R-2 and 6R-3.